THE UNIVERSITY *of* EDINBURGH

High-Pressure High-Temperature Behaviour of the Lanthanide Metals

K. A. Munro

Doctor of Philosophy
The University of Edinburgh
December 2016

Abstract

The high-pressure behaviour of the lanthanide series of metals has been the subject of study since the work of Percy Bridgman in the 1940s. Differences in said behaviour between the different lanthanide metals are attributed to the increasing occupation of the $4f$ electron shell as Z increases. Upon compression, or as Z decreases, the trivalent lanthanides (La to Lu, excluding Eu and Yb) undergo a common phase transformation sequence through various close packed structures: hcp $\rightarrow$ Sm-type (the structure adopted by samarium at ambient conditions) $\rightarrow$ dhcp $\rightarrow$ fcc $\rightarrow$ distorted fcc (d-fcc). Upon further compression, the lanthanide metals experience a first order transition to a "volume collapsed" phase. Many studies have focused on the low-Z members of the series, since the various phase transitions occur at much lower pressure where it is comparatively easy to collect high quality data. By contrast, the other members of the series have received comparability little attention, and there are even fewer reports of the structural behaviour of the lanthanide metals at high pressure and high temperature.

This thesis contains the results of angle-dispersive x-ray powder diffraction experiments at high pressure and high temperature of the various members of the lanthanide metals. Ce has been the subject of many previous studies, but a systematic x-ray diffraction study of the fcc/d-fcc phase boundary has never been attempted. Furthermore, the location in P-T space of the high temperature fcc/bct/d-fcc triple point has only been inferred, due to the lack of data on the fcc/bct phase boundary at high temperature. The high-pressure high-temperature phase diagram of Ce is presented and discussed.

La is unique amongst the lanthanide metals due to its empty $4f$ shell at ambient conditions. Despite this, La undergoes the common lanthanide transformation sequence up to the d-fcc phase, after which it undergoes a re-entrant transition back to the fcc phase at 60 GPa. The diffraction peaks of d-fcc La are shown in this thesis to undergo changes in intensity upon compression, indicating a

transformation to the $oI16$ structure found in Pr. La is one of the few elements whose behaviour has been unknown above 100 GPa, and results of La's structural behaviour upon compression to 280 GPa are presented and discussed. At 76 GPa, La begins a transition from the fcc phase to a new phase with the bct structure. Finally, the d-fcc $\rightarrow$ fcc re-entrant phase transition has been determined at various temperatures, and the d-fcc stability region has been mapped out.

Finally, x-ray diffraction experiments were performed on Gd up to 100 GPa and $\sim$700 K, to determine the structure of the d-fcc phase and the "volume collapsed" phase. While d-fcc Gd does not undergo pressure-induced changes similar to its low Z brethren, the d-fcc Gd remains stable up to 41 GPa at 700 K, putting a constraint on the d-fcc stability region. The data collected on Gd's "volume collapsed" phase cannot be fitted to the currently accepted $mC4$ structure. This has implications for our understanding of the lanthanide series as a whole, since most of of the heavier members, and some of the lighter lanthanides, are reported to adopt the $mC4$ structure.

Lay Summary

The majority of the elements adopt very simple crystal structures at atmospheric pressure and room temperature, with the atoms arranged as densely as possible. When compressed, the atoms within the structure can re-order to form very complicated arrangements. In the case of the lanthanide metals, they adopt a series of very similar, complex structures which have proved difficult to determine.

Pressure is applied by using a diamond anvil cell, consisting of two diamonds glued to two backing plates which are pulled together with screws. By placing a very small sample between the two diamond tips and turning the screws, a sample can experience pressures a million times higher than the air pressure found at sea level. Simultaneously, by using a heater attached to the diamond anvil cell, or by using a laser beam, the sample can be heated up to thousands of degrees while being compressed. Once compressed and hot, x-rays can be scattered off the re-arranged atoms to determine their new location, and the compressed sample's structure can thus be determined.

X-ray diffraction was performed on multiple lanthanide metals at various pressures and temperatures to determine their crystal structures. The high-pressure high-temperature behaviour of cerium and lanthanum have been determined, and the stability regions of the various structures have been mapped out. A previously unknown structure of lanthanum has been discovered, and evidence of a different structure for a high-pressure phase of gadolinium is reported.

Declaration

I declare that this thesis was composed by myself, that the work contained herein is my own except where explicitly stated otherwise in the text, and that this work has not been submitted for any other degree or professional qualification except as specified.

(*K. A. Munro, December 2016*)

Acknowledgements

Firstly, I would like to thank my supervisor Prof. Malcolm McMahon for his help and guidance during my PhD, without which, this project would not have been possible. I would also like to thank my industrial supervisor Dr Simon MacLeod for his advice and assistance, in particular, with the high-temperature components of this work, and for allowing me to use AWE's cells, diamonds and heating vessel. I would to thank the members of the McMahon group for help when preparing for, and during, beam time experiments: Dr Rachel Husband, Dr Graham Stinton, Dr Martin Gorman and Dr Richard Briggs. Special mention to Rachel Husband and Graham Stinton for answering my endless questions and assisting me when I was struggling. I would also like to thank Dr Heribert Wilhelm, Dr Annette Kleppe, Dr Dominik Daisenberger and Mr Allan Ross from beamline I15, Dr Michael Hanfland from beamline ID09, and Dr Hanns-Peter Liermann and Dr Zuzana Konôpkvá from beamline P02.2. Special mention to Annette Kleppe, Dominik Daisenberger and Allan Ross for going above and beyond with assistance in the early hours of the morning. Finally I would like to thank my office mates Charlotte, Melon, Duncan, Martin, Veronika and Amy for their continuous support.

Contents

List of Figures

List of Tables

List of Symbols and Abbreviations

P: Pressure

T: Temperature

λ: Wavelength

λ_0: Wavelength at ambient conditions

B: Bulk Modulus

B_{T}: Bulk Modulus at elevated temperature

B': Pressure derivative of the bulk modulus

B'': Double pressure derivative of the bulk modulus

V: Volume

V_0: Volume at ambient conditions

ϵ: Strain

σ_{j}: Applied stress field

f_{E}: Finite strain

$\alpha(T)$: Volume expansion coefficient

δ: Anderson-Grüneisen parameter

T_{ref}: Reference temperature

$P_{\mathrm{th}}(T)$: Thermal pressure

$\mathbf{R_n}$: Lattice vector

$\mathbf{a}$, $\mathbf{b}$, $\mathbf{c}$: Unit lattice vectors

a, b, c, α, β, γ: Lattice parameters

d: d-spacing

θ: Bragg angle

$\Delta\theta$: Difference between measured θ and the bragg angle

$\mathbf{k}$: Wave vector

$\mathbf{K}$: Change in wave vector

$\mathbf{R}$: Bravais lattice vector

$\mathbf{G}$: Reciprocal lattice vector

h, k, l: Miller Indices

A_{G}: Net scattering amplitude

F: Structure factor

f_{j}: Atomic form factor

K_{f}: K factor

e: Electron charge

λ_{U}: Magnetic period

B_{M}: Magnetic field

γ_{L}: Lorentz factor

m_e: Mass of an electron

v_{c}: Speed of light

pV: pseudo-Voigt

G: Gaussian

L: Lorentzian

H: Full width at half maximum (FWHM)

P_{k}: Empirical preferred orientation function

R_{p}: Conventional profile R-factor

wR_{p}^2: Weighted profile R-factor

PTM: Pressure transmitting medium

ADXRD: Angle dispersive x-ray diffraction

EDXRD: Energy dispersive x-ray diffraction

EoS: Equation of state

DLS: Diamond Light Source

ESRF: European Synchrotron Radiation Facility

DESY: Deutsches Elektronen-Synchrotron

DAC: Diamond Anvil Cell

LLNL: Lawrence Livermore National Laboratory

d-fcc: Distorted face centred cubic

dhcp: Double hexagonal close packed

Pressure calculator: Function which returns the sample pressure if the sample volume in known for a given temperature

P_{calc}: Calculated pressure from a pressure calculator

P_{marker}: Pressure as determined from the pressure marker

P_{shift}: The pressure shift needed to be applied to make transition pressures from different samples comparable

R_{ws}: Wigner-Seitz radius

R_{I}: Ionic radius

KVC: Kondo volume collapse

Chapter 1

Introduction

The study of elemental and molecular structures in condensed, solid states is an important area of research. If a material's structure is known then it is possible to determine a number of the material's properties. The majority of the metallic elements have very simple, dense structures, such as hexagonal close packed (hcp), or face centred cubic (fcc) at ambient conditions [1]. When pressure and heat are applied, even the elements undergo dramatic structural changes, and can even adopt complex incommensurate host-guest structures [1]. Such dramatic structural rearrangement results in radical changes to the material's properties: metallic sodium becomes a transparent insulator above 200 GPa or 2 Mbars [2], while the insulator sulphur transforms into a superconducting metal [3]. The application of pressure can also be used to study the minerals found in the earth's mantle [4], or employed to determine protein folding processes [5].

Pressure is often applied to a sample through the use of a diamond anvil cell (DAC). A DAC generates pressure by compressing the sample between the culets of the two diamonds anvils. It is possible to obtain pressures of 400 GPa using conventional diamonds with bevelled tips [6], while pressures of 1 TPa can be reached using synthesized nano-diamond spheres placed on conventional culets [7].

X-ray diffraction can be performed on a compressed sample to determine its crystal structure at high pressure. Ideally, the sample should be a single crystal. Data collected from a single crystal is 3-dimensional, and each observable reflection can be measured or indexed independently of the other reflections. Furthermore, single crystal data has a high signal to noise ratio, meaning even

the weakest signal can be detected. Unfortunately, acquiring a single crystal at high pressure is very difficult to achieve in practice, since the first order phase transitions that materials may undergo upon compression can break the single crystal [8]. As a result, almost all high-pressure experiments rely on powder x-ray diffraction, which projects the single crystal data into 1-dimension. This causes reflections with similar d-spacing to overlap, making it difficult to solve complex structures with multiple reflections. Since the sample is very small, the scattered x-ray signal is also very weak. In order to compensate for the weak signal, an incredibly bright x-ray source is required, such as a synchrotron.

The first high-pressure x-ray synchrotron diffraction experiments utilized energy dispersive x-ray diffraction techniques (EDXRD), where the use of the high flux from the full "white" beam compensated for the weak sample scattering [9]. EDXRD techniques were used to study the high-pressure behaviour of many of the elements, including the lanthanide series of metals [10], which were shown to undergo a transformation to new, complex phases at high pressure [11]. However, data collected from EDXRD experiments suffer from unavoidable contamination from sample fluorescence, poor resolution, and unreliable peak intensities [9]. The development of angle dispersive x-ray diffraction (ADXRD) techniques and image plate detectors advanced high-pressure science by reducing non-sample scattering, improved powder averaging resulting in accurate peak intensities and greatly improved resolution [9, 12, 13]. The improvements of ADXRD over EDXRD were exemplified when Hamaya *et al.* presented a new structure for a high-pressure phase of the low Z lanthanide metal, Pr [14].

It was eventually shown that, as pressure increases or as Z decreases, the majority of lanthanide metals (La-Lu except Eu and Yb) undergo a common phase transformation sequence through various close packed structures: hcp $\rightarrow$ Sm-type $\rightarrow$ dhcp $\rightarrow$ fcc $\rightarrow$ distorted-fcc (d-fcc) before transforming into a low-symmetry phase accompanied by a sudden decrease in volume (see [15] and the references within). The post-fcc phases can only be assigned a structure by observing very weak reflections, and subtle peak splitting effects. Due to the electronic similarities between the lanthanide metals, structural determination of the high-pressure phases found in the heavier members relies on "analysis by analogy" with the lighter members. As a result, the post fcc phases in different lanthanide metals are assigned very similar structures, albeit with slightly different lattice parameters. However, "analysis by analogy" is not infallible, and can result in an incorrect crystal structure being assigned to a high-pressure phase, which was

the case in Tb [16]. As such, a more robust analysis of the high-pressure phases found in the heavier lanthanide metals is required.

Most of the high-pressure high-temperature phase transitions were determined by observing changes in resistivity, and there are very few systemic x-ray studies of the lanthanide metals at temperature. Furthermore, these x-ray diffraction studies at high pressure and temperature report a currently unknown phase in both Pr and Gd [17, 18]. This thesis will attempt to confirm the structures of the high-pressure phases in some of the lanthanide metals, both at ambient and high temperature, and shed light on their behaviour at said conditions. Simultaneously, the phase diagrams at temperature of said lanthanide metals will be determined. The rest of this thesis is arranged as follows:

Chapter 2 will introduce the methods and equipment used in this thesis to study materials at high pressure and temperature, followed by a discussion of the theory of x-ray diffraction, and how x-rays are generated. Finally, the structural refinement methods used to analyse the x-ray diffraction data will be presented.

Chapter 3 will be a general review of the behaviour of the lanthanide series at high pressure and temperature as a whole. The d-fcc and "volume collapsed" phases in particular, will be discussed in detail.

Chapter 4 will provide an in-depth literature review of Ce, and present the outstanding issues this thesis aims to resolve. The results of extensive high-pressure high-temperature x-ray diffraction experiments on Ce will be discussed and an updated high-pressure high-temperature phase diagram will be presented.

Chapter 5 will present a literature review of La, similar to the literature review on Ce in Chapter 4. Results on La's d-fcc, and a possible transformation to a second d-fcc phase will be discussed. The first x-ray diffraction data collected on La above 100 GPa will also be presented. Finally, a high-pressure, high-temperature phase diagram of La will also be reported.

Chapter 6 will present a literature review devoted to Gd. The results x-ray diffraction experiments of Gd's d-fcc and "volume collapsed" phases will be presented.

Finally, Chapter 7 will give a brief summary of the results contained within this thesis, will outline some possibilities for future study, and highlight a possible avenue for improving the apparatus described in Chapter 2.

Chapter 2

Experimental Methods

2.1 Diamond Anvil Pressure Cells

The diamond anvil cell (DAC) is an invaluable tool for high-pressure research, capable of emulating conditions found in the center of planets. The first DAC was developed separately and simultaneously by Weir *et al.* [19] and Jamieson *et al.* [20], and was a huge advancement in high-pressure research. Diamond is an ideal anvil material, able to endure much larger stresses and reach higher pressures compared to other materials due to its strength. Diamond is also transparent to many different types of electro-magnetic radiation, allowing a potential sample to be viewed optically to observe any changes. It is also possible to perform Raman, spectroscopic and x-ray studies at high pressure. Other properties of diamond include a high thermal conductivity, which has to be taken into account when heating samples using external and internal resistive heating techniques.

The DAC generates pressure by compressing a sample between the small, flat tips, or culets, of two opposing anvils. The anvils are attached to either beryllium or tungsten carbide backing discs, which are then fixed into the metal body of the DAC itself. The diamond culets must be parallel and spatially overlapped to minimize any pressure gradients being applied to the diamonds, which increases the risk of anvil failure. The two halves of the DAC are then typically pulled together using screws. Care must be taken to turn the screws by an equal amount keep the application of force as uniform as possible. A gearbox can also be used to ensure a uniform application of force. By this method, force is applied to

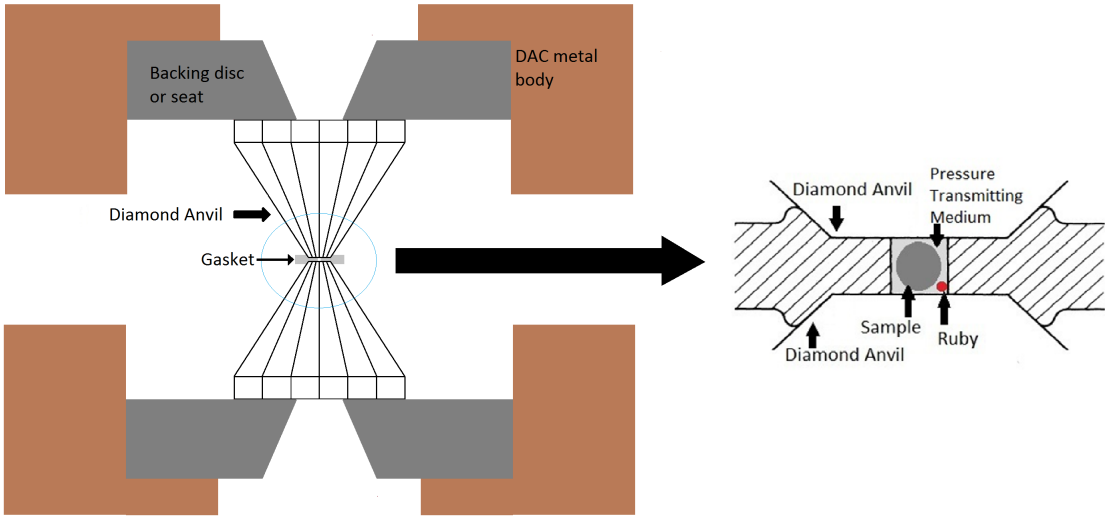

Figure 2.1 *Schematic diagram of a diamond anvil cell (DAC). The sample, pressure calibrant such as ruby, pressure transmitting medium are loaded into the sample chamber, which is compressed by the diamond culets.*

the larger back of the diamond which propagates through the diamond, and is magnified at the culet tip due to the reduction in area. In an x-ray diffraction experiment, the incident x-ray beam is transmitted through one anvil, enters the sample and the diffracted x-rays exit through the other anvil. The opening angle on the backing disk on the exit side of the cell must be as large as possible, to maximise the amount of diffraction data available.

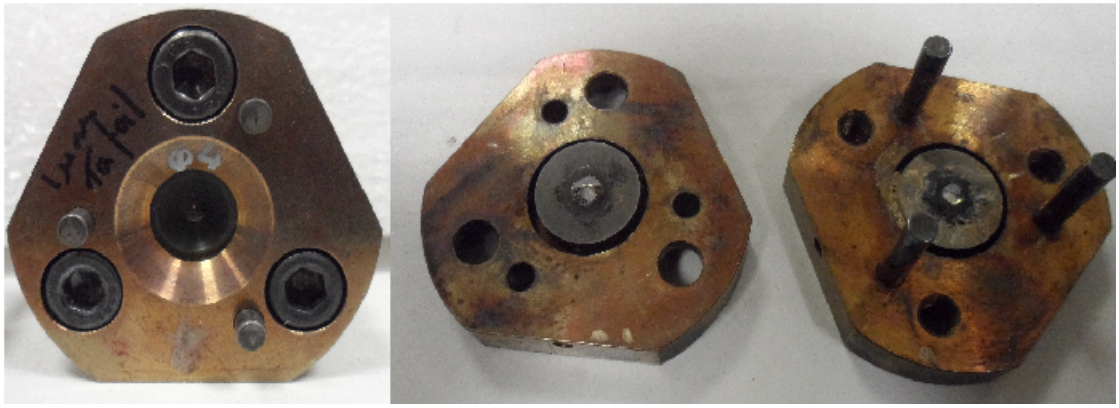

Figure 2.2 *Left: Image of a closed Merrill-Bassett DAC. Right: An open Merrill-Bassett DAC with diamonds attached to tungsten carbide seats.*

There are many designs of DAC, one of the oldest of which is still in use is

the Merrill-Bassett (MB) cell which uses 3 screws to generate the pressure [21]. The MB cell is very light and compact, which allows the cell to be mounted on a goniometer head for *in situ* diffraction experiments. Originally the MB cell utilised beryllium backing discs [21], since beryllium has a high mechanical strength and is x-ray transparent. These properties allowed the diamond anvil to be supported, while maintaining a very large opening angle to maximise the amount of diffraction data available. Unfortunately, beryllium is very toxic if inhaled and loses its mechanical strength if heated. Both the straight through beam and the diffracted x-rays must also pass through the detector side backing disc, each creating its own diffraction pattern superimposed on the pattern from the sample. By reducing the support to the anvils, and thus, increasing the chance of a breakage, other materials opaque to x-rays can be used to make the backing discs, such as tungsten carbide. Tungsten carbide is non-toxic and maintains its mechanical properties at high temperature. A new backing disc was designed by Boehler *et al.* [22] which provides support to the anvil, while keeping the opening angle as large as possible, see Figure 2.3.

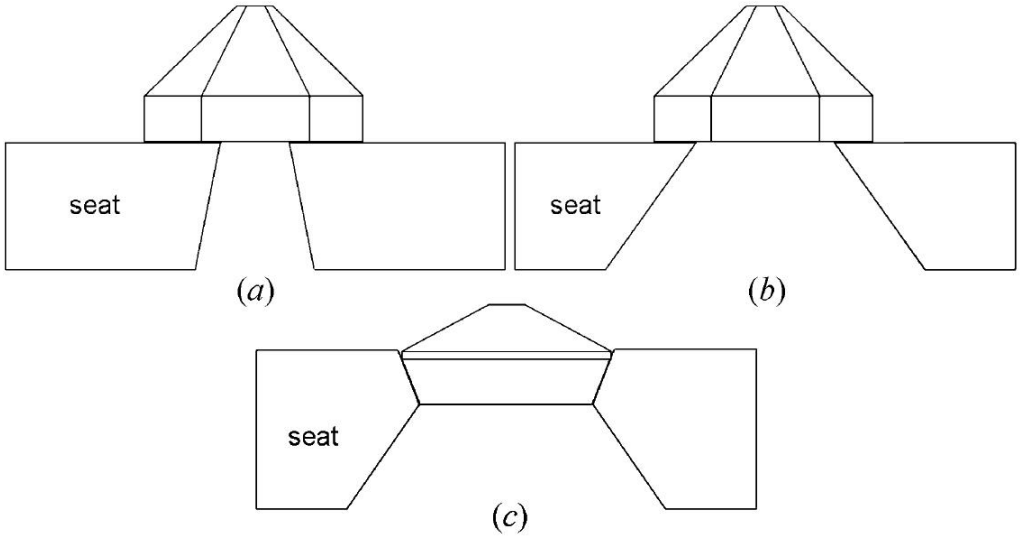

Figure 2.3 *Diagram of the backing seat and anvil design for: (a) a standard brilliant cut diamond on a MB beryllium seat. (b) a standard brilliant cut diamond on a MB tungsten carbide seat, in order to maintain a large opening angle there is very little material supporting the anvil. (c) a conical Boehler-Almax diamond with a Boehler-Almax tungsten carbide seat. The seat has been machined so a diamond can be deeply embedded. Image modified from Moggach et al. [23].*

Instead of using screw driven DACs, it is possible to increase pressure by using a gas-filled membrane. Gas can be added or removed from the membrane to

remotely control the pressure, when access to the DAC's screws is not possible. For example, if the cell is too hot to manipulate or if the cell is inside a vacuum vessel. This type of DAC is called a gas membrane driven piston cylinder diamond anvil cell, or piston cell. The piston cell typically consists of a cylindrical cell body, and a piston, which has been machined to perfectly fit inside the cell body (see Figures 2.4 and 2.5). The diamond anvils are placed in the cell body and on top of the piston, and are aligned using screws, with the perfect fit of the piston ensuring the anvils remain aligned during the loading process. The piston cell used for the research in this thesis was a Lawrence Livermore National Lab (LLNL) cell designed by Jenei *et al.* for use in a vacuum vessel which has been described in Section 2.5 [24].

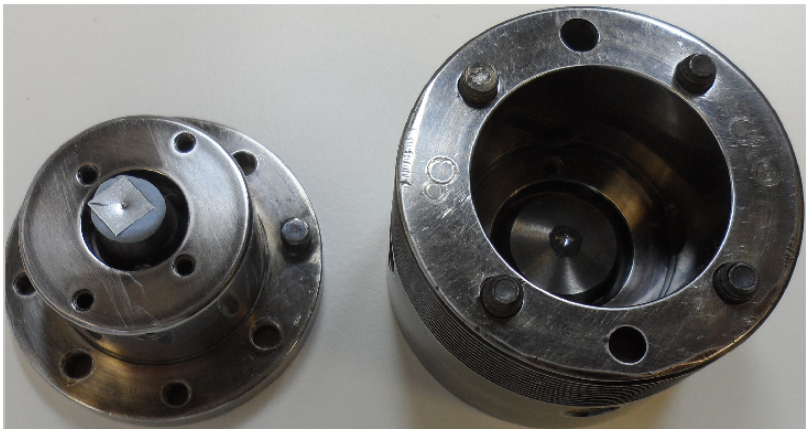

Figure 2.4 *Image of an open piston DAC.*

A gasket is required to contain the sample, pressure calibrant and the pressure transmitting medium (see Figure 2.1). The calibrant and medium are discussed further in Sections 2.2 and 2.4 respectively. The gasket is a 1 cm by 1 cm piece of metal, initially 200 μm thick. Typical gasket materials include rhenium, tungsten or steel. The gasket is first indented using the DAC, creating a support ring of hardened gasket material which decreases the shear stress on the diamond anvil on compression, and increases resistance to breakage [25]. The indent is typically indented to $\sim$20 μm thick for 200 μm culets, and 20-25 μm for 300 μm diamonds. A perfectly cylindrical sample chamber is then drilled in the center of the indent. Ideally the sample chamber's diameter is 1/3 of the indent diameter (see Figure 2.1). When the cell is closed the culets seal the sample chamber. As pressure is applied to the indent, the gasket material flows outward causing friction between the gasket and the anvil [26]. This causes a pressure gradient across the culet which is proportional to the shear strength of the gasket material and inversely

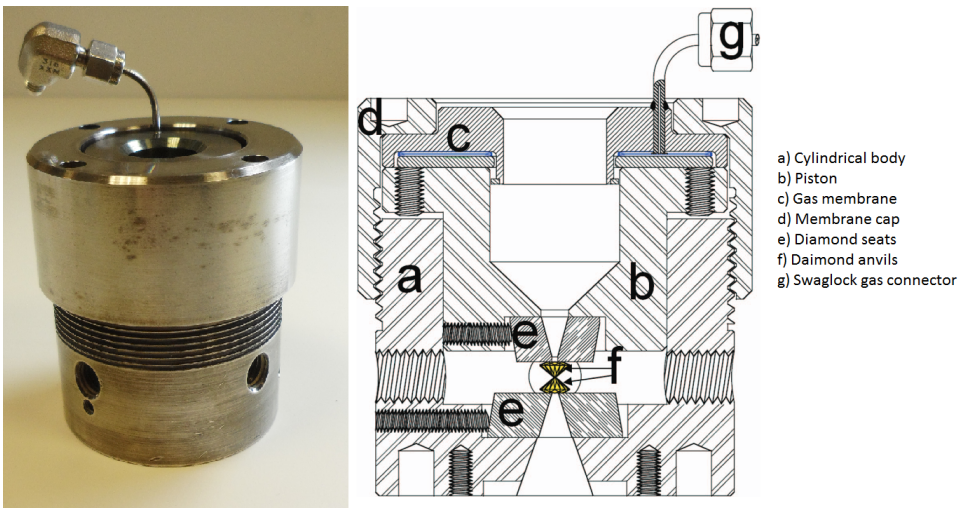

Figure 2.5 *Left: Image of a closed LLNL cell with a gas membrane attached to the piston using a metal cap, with the swaglock gas connector protruding from the top. Right: Schematic drawing of the same LLNL cell with a gas membrane attached to the piston. Image modified from Jenei et al. [24].*

proportional to the indent thickness [27]. If the sample chamber has not been drilled correctly the sample chamber may distort, or become displaced, which can lead to a breakage if pressure continues to be applied.

A problem with the standard cut of diamond is that at very high pressures the normally flat culet becomes concave, with stress being concentrated at the culet edge. This results in the culets cutting through the indented gasket to touch the other anvil. Due to the increase in stress on the culet edges the chance of anvil failure greatly increases. This places an upper limit on the pressures that can be achieved. The diamond anvil can be bevelled (see Figure 2.6), which at extremely high pressures deforms inward to counteract the deformation of the culet, and spreads the stress more homogeneously between the culet and the bevel [28]. This increases the maximum pressure that can be reached before anvil failure.

2.2 The Pressure Calibrant

A pressure calibrant is added to the sample chamber in order to accurately determine pressure being applied to the sample. Pressure can be determined by measuring the volume of an internal diffraction standard and utilizing its known Equation of State (EoS), or by measuring the change in fluorescence emitted from

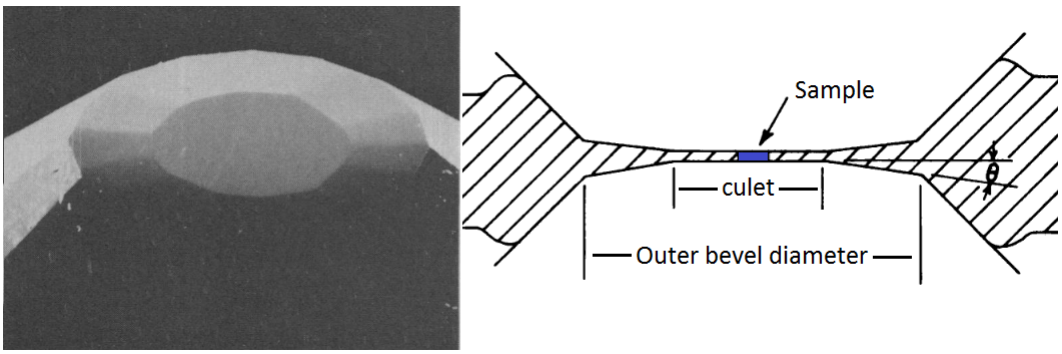

Figure 2.6 *Left: Scanning electron micrographs of a bevelled culet. Right: Schematic diagram of a beveled diamond/gasket/sample assembly. Images modified from Mao et al. [29]*

the calibrant.

2.2.1 Fluorescence

The most common fluorescence calibrant used in high-pressure experiments is corundum doped with chromium, otherwise known as ruby (Al_2O_3:Cr_{3+}). The luminescences of ruby was studied in great detail for use in early lasers [30]. When illuminated with a laser, ruby fluoresces strongly, emitting two R-lines (labelled R_1 and R_2) with wavelengths 694.25 nm and 692.86 nm respectively (see profile a) in Figure 2.7). The ruby fluorescence technique was first pioneered by Forman *et al.*, eliminating the need to estimate the pressure being applied to the sample. The R_1 line was shown to increase linearly with pressure at low pressures [31]. Further work demonstrated that the ruby fluorescence technique is a very rapid and convenient method for measuring pressure, and was calibrated to the Decker EoS of sodium chloride (NaCl) [32, 33]. Mao *et al.* pushed the pressure calibration of ruby up to 100 GPa and set the ruby calibration against the EoS of many other materials. Mao *et al.* also showed that the scale needed a slight non-linear correction at higher pressures and this scale is in use today [29]. Because of its ease of use, ruby fluorescence has been studied extensively up to 150 GPa, and the calibration is shown below in Equation 2.1 [34].

$$P(\text{GPa}) = 1870\left(\frac{\lambda}{\lambda_0} - 1\right)\left[1 + 5.9\left(\frac{\lambda}{\lambda_0 - 1}\right)\right] \tag{2.1}$$

where λ is wavelength of emitted radiation and λ_0 = wavelength of emitted radiation at 0 GPa.

Unfortunately, above 100 GPa the fluorescence signal significantly decreases in intensity. In addition, the R_1 line's wavelength is strongly temperature dependant, and as temperature increases the intensity of the R_1 line also decreases. Above 550 K the R_1/R_2 doublet also broadens rapidly and merge into a single band [32]. The doublet also can merge into a singlet when the ruby piece is "bridged" or touching both diamond anvils, see Figure 2.7. In this thesis ruby fluorescence was only used for low pressure, room temperature experiments, due to the temperature limitations of the ruby fluorescence calibration.

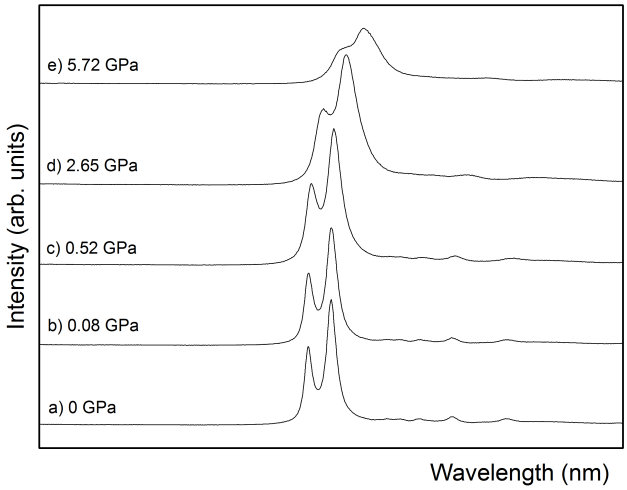

Figure 2.7 *Graph of ruby fluorescence as pressure increases. As the sample is compressed the diamonds touch the ruby sphere, and the R_1/R_2 lines start to broaden and merge. A large ruby was selected on purpose to highlight the bridging effect.*

2.2.2 Internal Diffraction Standard

A second method of determining the sample pressure is to insert small pieces of a diffraction standard into the sample chamber, and determine the pressure of the sample by measuring the lattice parameters of the standard whose EoS must be well known. Ideal internal diffraction standards have the following qualities: Highly symmetric crystal structure, high compressibility, absence of high-pressure, high-temperature phase transitions in the pressure-temperature region of interest, strongly scattering and chemically inert.

Having a highly symmetric crystal structure minimises the number of possible diffraction peaks that could overlap with the sample peaks. A body centered cubic material is ideal, since any overlap between the standard signal and the sample

signal is minimised, aiding both determination of the sample's structure and the pressure measurement. A high compressibility means a small pressure increase translates to a large change in volume, allowing the pressure to be precisely determined. A strongly-scattering material means that only a very small amount of calibrant relative to the sample is necessary. The calibrant must not react with another material in the sample chamber, diamond, or the gasket. Historically, NaCl at ambient conditions was the first material that had an equation of state determined, up to 15 GPa [35]. NaCl was chosen due to the large quantity of experimental data available to fit the EoS parameters to, and the simplicity of the original model used [35]. Other internal pressure standards include Au, Pt, Ta and Cu. The main benefit of using a diffraction standard is that pressure can be determined with very high precision from the diffraction measurement itself, and a separate optical measurement is unnecessary. However, this also means that the pressure cannot be determined until after the diffraction measurement is taken, rather than being able to adjust the pressure to the necessary value before collecting the data. Another downside is that the diffraction peaks from the standard could potentially overlap with the diffraction peaks from the sample, complicating both pressure and structure determination.

In almost all of the experiments described in this thesis, Ta was used as the pressure calibrant. Either a small grain of Ta 1-2 μm in diameter or a 1 μm thick Ta foil was placed into the sample chamber. The pressures were determined by using the equation of state as determined by Hanfland *et al.* [36]. To account for the thermal expansion of the Ta pressure calibrant above room temperature, a thermal correction was applied based on the results of Dorogokupets *et al.* [37]. Ta is vulnerable to hydrogen embrittlement [38], which is exploited to make the creation of Ta powders easier via ball milling [39]. Once the Ta has been powderised, most of the hydrogen is removed. However, the lattice parameter of Ta at ambient conditions is linearly dependant on the amount of hydrogen absorbed [40], making contaminated Ta appear less compressed compared to pure Ta. The largest value for Ta measured at ambient conditions was 3.30619(8) Å, which corresponds to a hydrogen content of ∼300 ppm, and causes a ∼1.66 GPa shift at 62.3 GPa compared to pure Ta. The ambient volume of Ta was always determined at the start of each experiment to establish V_0 for use in the equation of state.

Some experiments were performed in which an alternative diffraction standard was used. 1 μm thick Au foil was used for high-temperature experiments using the

equation of state by Dorogokupets *et al.* [37] or Yokoo *et al.* [41]. Finally, 3 μm thick Cu foil and NaCl powder were used in one high-temperature experiment, and pressures were calculated from the equation of states by Cynn *et al.* [42] and Dorogokupets *et al.* [43], respectively.

2.3 Equation of State

A solid's isothermal equation of state, or simply equation of state, describes a volume change under hydrostatic pressure at a fixed temperature. The equation of state is characterised by the solid's bulk modulus $B = -V(\partial P/\partial V)_{\mathrm{T}}$. For small changes in pressure and volume, B can be defined in terms of the elastic tensor by applying linear elasticity theory or Hooke's Law. When applying Hooke's law, it is assumed that the strains of the solid, ϵ_{i}, are linearly related to the magnitude of the applied stress field σ_{j} by the equation $\epsilon_{\mathrm{i}} = s_{\mathrm{ij}}\sigma_{\mathrm{j}}$ [44]. The suffixes range from 1 - 6, with i, j = 1, 2, 3 referring to normal stresses and strains along orthogonal axes, while i, j = 4, 5, 6 refers to shear stresses or strains. The material's elastic properties are represented by s_{ij}, which are elements of the symmetric compliance matrix [45].

Hydrostatic pressure is a stress state where all normal stresses are equal $\sigma_1 = \sigma_2 = \sigma_3$, and all shear stresses are zero, $\sigma_4 = \sigma_5 = \sigma_6 = 0$. Under these conditions it is possible to calculate all changes in pressure from Hookes law by setting $-\partial P = \sigma_1 = \sigma_2 = \sigma_3$. The individual strain elements can then be written as ϵ_{i} = $s_{\mathrm{i1}}\sigma_1 + s_{\mathrm{i2}}\sigma_2 + s_{\mathrm{i3}}\sigma_3$ = -$(s_{\mathrm{i1}} + s_{\mathrm{i2}} + s_{\mathrm{i3}})\partial P$. Since the sum of the 3 normal strains is equal to the fractional change in volume in the infinitesimal limit, the fractional change in volume can be written in terms of s_{ij} and ∂P [44]:

$$\frac{\partial V}{V} = \epsilon_1 + \epsilon_2 + \epsilon_3 = [s_{11} + s_{22} + s_{33} + 2(s_{12} + s_{13} + s_{23})]\partial P. \tag{2.2}$$

Rearranging this equation shows the bulk modulus under hydrostatic compression can be written as:

$$B = -V\frac{\partial P}{\partial V} = [s_{11} + s_{22} + s_{33} + 2(s_{12} + s_{13} + s_{23})]^{-1} \tag{2.3}$$

The bulk modulus can thus be defined under hydrostatic compression at any pressure using Hooke's law. But this is impossible to achieve in practice since

all pressure and volume changes are finite. Therefore, it is nessesary to define an equation of state in terms of how the bulk modulus varies with pressure, $B' = \partial B/\partial P$ and $B'' = \partial^2 B/\partial P^2$ [44]. There is no thermodynamic basis for describing how the bulk modulus varies with pressure, and further assumptions have to be made [46]. The validity of such assumptions is determined by how well the equation of state reproduces the experimental data.

One assumption is to assume that the strain energy of a solid undergoing compression can be expressed as a taylor series in finite strain f_{E} [47], which is defined in Equation 2.4.

$$f_{\mathrm{E}} = \left[\left(\frac{V_0}{V}\right)^{\frac{2}{3}} - 1\right]/2 \tag{2.4}$$

where V is the volume and V_0 is the volume at ambient conditions. Expanding to the 4^{th} order in the strain yields the Birch-Murnaghan EoS.

$$P = 3Bf_{\mathrm{E}}(1+2f_{\mathrm{E}})^{5/2}\left[1 + \frac{3}{2}(B'-4)f_{\mathrm{E}} + \frac{3}{2}[BB'' + (B'-4)(B'-3) + \frac{35}{9}]f_{\mathrm{E}}^2\right] \tag{2.5}$$

If the Birch-Murnaghan EoS is truncated to 2^{nd} order in the energy, the coefficient of f_{E} must equal zero, which requires B' to be equal to 4. In the 3^{rd} order truncation, the coefficient of f_{E}^2 is set to zero, which implies that $B'' = \dfrac{-1}{B}\left[(3-B')(4-B') + \dfrac{35}{9}\right]$ [46, 48].

The simplest method of evaluating P-V data at elevated temperature is to consider how the EoS parameters vary at an elevated temperature [48]. The bulk modulus at elevated temperatures, B_{T}, can be written as [44]:

$$B_{\mathrm{T}} = B\exp -\delta\int_{T_{\mathrm{ref}}}^{T}\alpha(T)dT \tag{2.6}$$

where $\alpha(T) = V^{-1}\partial V/\partial T$ and is the volume thermal expansion coefficient, δ is the Anderson-Grüneisen parameter defined as $(1/\alpha(T)B)(\partial B/\partial T)_{\mathrm{P}}$ [49], T_{ref} is a reference temperature, T is the elevated temperature and B is the bulk modulus at the reference temperature. The volume thermal expansion coefficient can be approximated to quadratic function of temperature: $\alpha(T) = \mathrm{a}_1 + \mathrm{a}_2 T + \mathrm{a}_3 T^2$ where a_1, a_2 and a_3 are constants [50].

The total pressure $P(V,\ T)$ at an elevated temperature can be expressed as the

sum of the pressure at T_{ref}, $P(V, T_{\mathrm{ref}})$, and the thermal pressure function $P_{\mathrm{th}}(T)$. The thermal pressure function is the pressure increase that would be observed by increasing the temperature from T_{ref} to T at constant volume and ambient pressure, and depends on B_{T} [44].

Once a sample's EoS is known, it is then possible to estimate the pressure of the sample simply by determining the sample's volume and temperature, eliminating the need for a marker. While not suitable for determining phase boundaries or melt curves, it completely removes the possibility of the marker signal contaminating the sample signal. It is also possible to fit isothermal P-V data to a much more simple equation such as quadratic. Such a fit allows the calculation of the sample's pressure simply by knowing the sample's volume, and are referred to as "pressure calculators" throughout this thesis.

2.4 Pressure Transmitting Medium

As discussed in Section 2.1, the pressure in the diamond anvil cell is generated by the diamonds applying a force along one axis. The pressure applied in this way across the sample volume is inhomogeneous, or non-hydrostatic. Inhomogeneous pressure causes the diffraction peaks to broaden, while uni-axial stress causes a systematic shift in peak positions. Under uni-axial stress the sample is deformed in such a way that the crystal lattice planes perpendicular to the pressure direction are more compressed, compared to lattice planes parallel to the pressure direction. X-ray diffraction is impossible from the perpendicular planes (assuming an axially-oriented beam), hence the average pressure determined from a diffraction standard, and thus the pressure the sample is experiencing, will be underestimated [51]. Non-hydrostaticity can be quantified by measuring both the full width at half maximum (FWHM) and the splitting, of the R_1 and R_2 ruby fluorescence peaks [33, 52].

In order to reduce the effects of non-hydrostatic pressure, a pressure transmitting medium (PTM) is included in the sample chamber. The PTM must be inert, compressible, optically and x-ray transparent, have low strength and weakly scattering. A PTM transforms the stress generated by the anvils into a stress whose non-hydrostaticity is contained by its own yield stresses [53]. This means that the force applied from the culet is applied uniformly across the sample. Various materials can be used as a PTM and in this work some of the samples

were loaded in a helium PTM. Despite solidifying at 11.5 GPa [54], helium remains soft and retains its hydrostaticity up to 40 GPa [55]. However, since the samples studied in this thesis are very reactive, in most cases no PTM was used to avoid forming compounds with the sample within the sample chamber during sample preparation.

2.5 High-Temperature Methods

Temperature is another thermodynamic variable which influences the properties of matter, and extra considerations must be taken into account when modifying high-pressure apparatus for high-temperature work. There are broadly two methods of applying heat to a pressurised sample within a DAC: resistive heating and laser heating.

Resistive heating can be further categorised between external and internal resistive heating. External resistive heaters are attached to the outside of the DAC itself, and heat is transferred through the cell body, diamonds and gasket to the sample via conduction. The temperature is uniformly distributed across the sample, ensuring the repeatability of individual measurements and leading to accurate measurements of P-V-T equations of state [56]. A uniform temperature also "relaxes" the sample, reducing stress. Due to the thermal expansion of the DAC, the sample may experience pressure changes, but these changes can be regulated utilizing a membrane, as discussed in Section 2.1. While temperature is easy to maintain using an external heater, the expansion of a piston cell can cause the piston become stuck. This leads to a "build up" of force if more gas is added to the membrane, and if the DAC becomes unstuck a large force is very rapidly applied to the sample, resulting in a large pressure increase and possibly diamond failure [57].

Placing a miniaturised internal heater inside the DAC largely removes the problems encountered by external heaters. These internal heaters are attached to the gasket, or are placed within sample chamber itself, taking care to electrically insulate the metal components of the DAC from the internal heater [58]. Using an internal heater removes the need to heat the whole cell body, and thus requires much less power and enables higher maximum temperatures [58]. However, temperature gradients across the sample from an internal heater are much more pronounced compared to external heaters [59, 60]. Furthermore, care must be

taken to prevent the heater wires from being destroyed upon closing the DAC [58].

Laser heating can heat samples to over 5000 K [61], much higher than the temperatures reached with resistive heating techniques. Lasers have the high power output and low beam divergence necessary to focus on, and heat, a small spot on the sample which can vary between 10 μm and 50 μm in diameter [62]. Vitally, the x-ray beam has to be focused to a point smaller than the laser spot. The laser also requires a high power stability and a high pointing stability to ensure uniform heating [63]. By heating the sample on both sides, slightly defocusing the spot and using beam focusing optics to change the spot size, temperature gradients across the spot and within the sample are reduced. However, laser heating suffers similar drawbacks to internal heaters. The sample can experience large temperature gradients, up to hundreds of kelvin per micron, which applies large thermal stresses to the sample [61]. The temperature can also fluctuate rapidly, meaning a stable temperature can only be maintained on a time scale of minutes, up to an hour [64]. Diamond has a very high thermal conductivity, and is able to dissipate heat very rapidly. As a result, care has to be taken to thermally insulate the sample from the diamonds [65]. This can be achieved by surrounding the sample with an insulator like alumina, MgO or NaCl [65–67], or by elevating the sample above the culet using ruby spheres [65].

High-pressure, high-temperature experiments in this thesis were performed using external resistive heaters to apply heat. Heat is transferred to the sample via conduction through the cell body from the heater. The LLNL cells were heated *in situ* using a custom built copper block equipped with 4 cartridge heaters purchased from Watlow Ltd. The copper block was able to heat the sample up to 200 degC without oxidising the diamond anvils or melting the white plastic thermal insulation, see Figure 2.8. A gas membrane was used to change pressure, as described in Section 2.1.

To reach temperatures above 200 degC, a coil heater was wrapped around the cell body which was then placed into a custom-made vacuum vessel. A vacuum of less than 10^{-4} mbar was obtained to minimise heat loss from conduction and convection, reducing the power required to reach higher temperatures. The vacuum also prevents the diamonds from oxidation at higher temperatures. The vacuum vessel was water cooled by pumping water from a reservoir being cooled by a chilling unit, or by using water from the mains. The sample temperature was measured using a K-type thermocouple glued using thermal cement [68] to

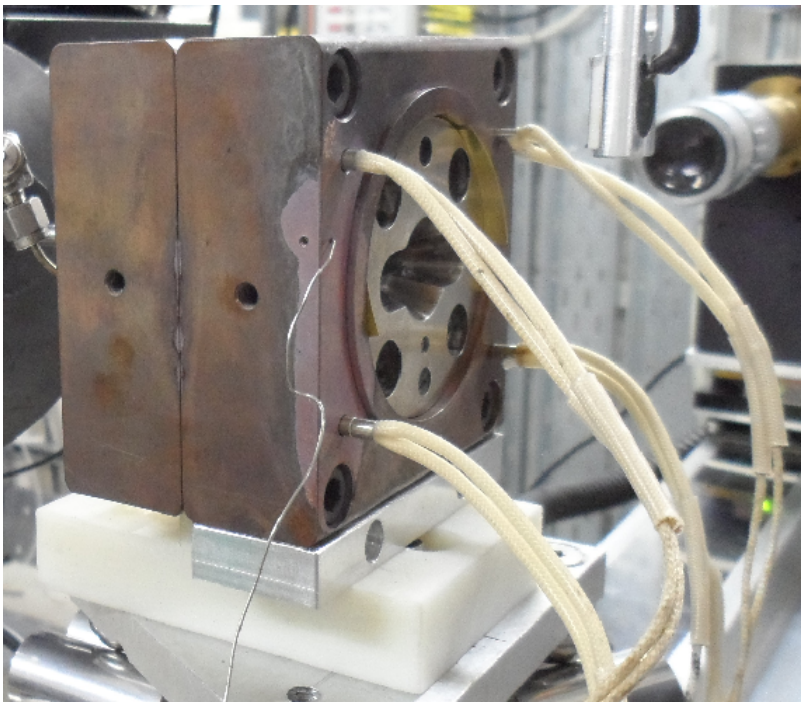

Figure 2.8 *Image of the copper block applying heat to a LLNL cell attached to the plastic support, set up on beamline I15 at the Diamond Light Source.*

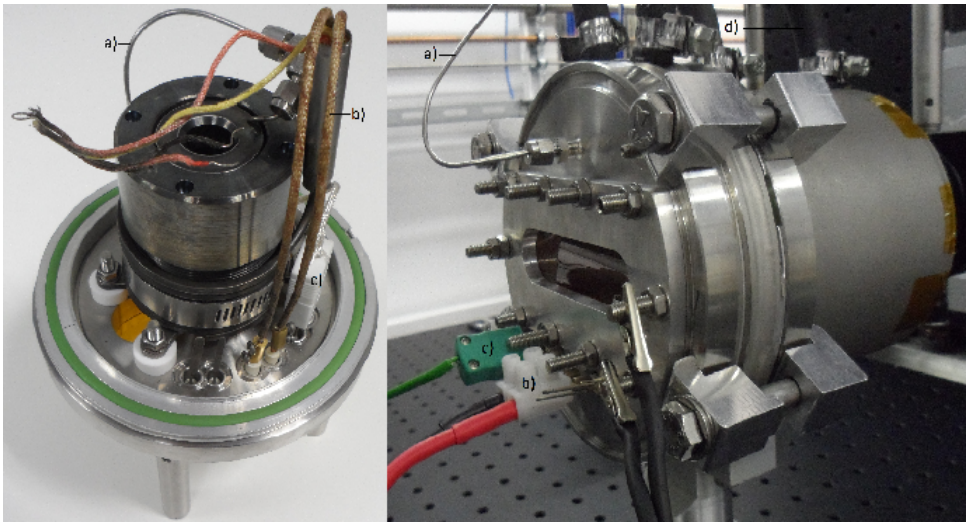

Figure 2.9 *Left: Image of the LLNL cell attached to the front flange, before being loaded into the vacuum vessel. Right: Image of the heating vessel set up on beamline BL04 at ALBA. a) The gas membrane capillary tube which pumps in gas to compress the cell. b) The power cables for the coil heater. c) The thermocouple wires to measure the temperature. d) the tubes for the water cooling system to prevent the vacuum vessel from overheating.*

the backing discs. Both the thermocouple wires and the heater power leads are fed through the front flange of the vacuum vessel as shown in Figure 2.9. In later experiments two thermocouples were used, one on each diamond and an average reading was used as the sample temperature. The maximum difference between the two thermal couples was 9 K in the high-temperature experiments, although in general the temperature difference was less than 0.5 K.

2.6 Crystalline Structures

2.6.1 The Unit Cell

A perfect crystalline solid can be described as an infinitely large number of identical arrangements of elements or molecules repeating in all directions. Due to this repetition, crystalline solids have long range order, or translational symmetry. It is possible to mark identical points (i.e. points that have the same surroundings, in the same orientation) in 3 dimensions within a crystalline solid. These points are called lattice points and together make up the Bravais lattice of the structure, and are related by translational symmetry using the following lattice vector equation:

$$\mathbf{R_n} = n_1\mathbf{a_1} + n_2\mathbf{a_2} + n_3\mathbf{a_3} \tag{2.7}$$

where n_1, n_2, n_3 are integers, and $\mathbf{a_1}$, $\mathbf{a_2}$, $\mathbf{a_3}$ are primitive lattice vectors which make up the primitive unit cell, which by definition contains only 1 lattice point. There are an infinite number of non-equivalent choices for the primitive unit cell, but many of the choices do not utilise the full symmetry of the Bravais lattice, meaning the primitive unit cell is over-parameterised. A solution is to use non-primitive cells, called the conventional unit cell or simply the unit cell, which is described by unit lattice vectors $\mathbf{a}$, $\mathbf{b}$ and $\mathbf{c}$ with lengths $a = |\mathbf{a}|$, $b = |\mathbf{b}|$ and $c = |\mathbf{c}|$ respectively. The unit cell fills space without any overlap when translated through a subset of the Bravais lattice vectors. The unit lattice vectors do not have to be orthogonal, and it is necessary to define the angles between the unit lattice vectors: α for the angle between $\mathbf{b}$ and $\mathbf{c}$, β for the angle between $\mathbf{a}$ and $\mathbf{c}$ and γ for the angle between $\mathbf{a}$ and $\mathbf{b}$. Collectively, the 3 lengths (a, b and c) and the 3 angles (α, β and γ) are called lattice parameters, which enclose a parallelepiped volume [69, 70].

The unit cell can be thought of as the basic building block, which can be translated

to all points on the lattice to build the crystal lattice. In order to complete the description of the crystal structure, a basis of atoms or molecules must be present at each lattice point. Coordinates of the atoms or molecules for each lattice point inside the unit cell are expressed as fractions of the unit cell parameters.

$$\mathbf{r} = x_1\mathbf{a} + x_2\mathbf{b} + x_3\mathbf{c} \tag{2.8}$$

where x_1, x_2, x_3 vary between 0 and 1.

It is sometimes convenient, particularly when analysing periodic structures, to define the reciprocal lattice, which is the Fourier transform of the lattice in real space. The lattice vectors of the reciprocal lattice in reciprocal space, $\mathbf{a_1^*}$, $\mathbf{a_2^*}$ and $\mathbf{a_3^*}$, can be generated from the lattice in real space using equations 2.9.

$$\mathbf{a_1^*} = 2\pi\frac{\mathbf{a_2} \times \mathbf{a_3}}{\mathbf{a_1} \cdot (\mathbf{a_2} \times \mathbf{a_3})} \tag{2.9a}$$

$$\mathbf{a_2^*} = 2\pi\frac{\mathbf{a_3} \times \mathbf{a_1}}{\mathbf{a_1} \cdot (\mathbf{a_2} \times \mathbf{a_3})} \tag{2.9b}$$

$$\mathbf{a_3^*} = 2\pi\frac{\mathbf{a_1} \times \mathbf{a_2}}{\mathbf{a_1} \cdot (\mathbf{a_2} \times \mathbf{a_3})} \tag{2.9c}$$

and all lattice points in reciprocal space can be defined by equation 2.10

$$\mathbf{G} = h\mathbf{a_1^*} + k\mathbf{a_2^*} + l\mathbf{a_3^*} \tag{2.10}$$

where h, k and l are integer numbers, collectively called Miller indices.

2.6.2 Crystallographic Planes

A set of crystallographic planes is defined as a set of planes that intercept all lattice points, all parallel to each other and equally spaced apart by distance, d. The distance d is calculated for each lattice, for each set of planes. Each set of planes is described using the Miller indices: h, k, and l.

In this thesis, a set of planes is written as (hkl), for example (111). However the Miller indices can reach double digits, making it difficult to determine which set of planes is being discussed. For example (0111) can refer to either: $h = 0$, $k = 1$, and $l = 11$, or $h = 0$, $k = 11$, and $l = 1$. In such cases, commas are added for

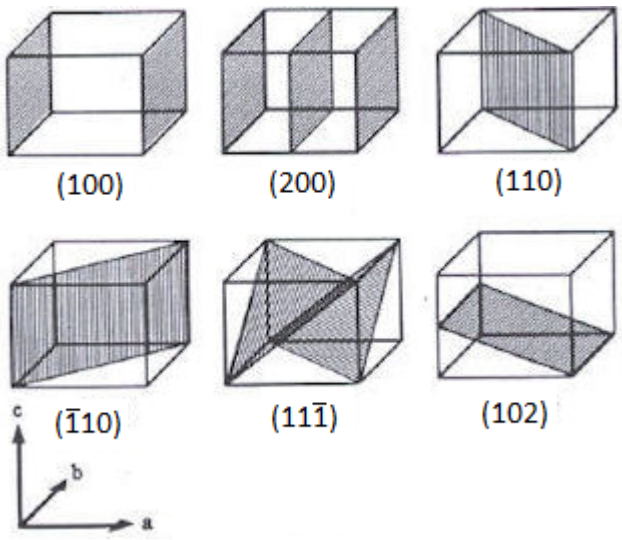

Figure 2.10 *Image of Miller Planes. Image modified from [71].*

clarification. For example (0111) becomes (01,11) indicating that $h = 0$, $k = 1$, and $l = 11$.

2.6.3 Crystallographic Symmetry

A symmetry element is a physically identifiable point, line or plane in an object (such as a molecule) about which symmetry operations are applied. A symmetry operation applies an operation which leaves the object with an identical appearance (such as an inversion about a point, a rotation about a line, or a reflection about a plane). Symmetry elements can be combined only in certain ways that are consistent with each other. In the case of a molecule the symmetry elements must pass through the center of said molecule which is also the inversion center if there is one. Because of the dependence on the molecule's center the collection of symmetry operations for a molecule is called its point group. By contrast, symmetry elements in a solid do not all pass through one point, and the symmetry elements present in one unit cell are translated into other units [69].

In theory, it is possible for there to be any order of rotation within a molecule. In a crystalline solid, some symmetry operations are restricted due to the necessary combination of certain symmetry operations with translational symmetry operations. Only 1^{st}, 2^{nd}, 3^{rd}, 4^{th} and 6^{th} orders of rotations are allowed. Due to this restriction there are only 32 point groups that can be applied to a solid. If there is rotational symmetry or reflection symmetry in a

solid, restrictions are imposed on the unit cell parameters. For example a 4-fold rotation means that the unit cell must have 2 square faces exactly opposite each other with an axis parallel to the rotation axis. This means that 2 of the cell lengths must be equal and the 3 angles are 90^o. On the basis of these restrictions there are 7 different crystal systems. Combining these 7 systems with the various different unit cell centering leads to 14 distinct combinations, called the 14 Bravais lattices. Combining the 14 Bravais lattices with all possible symmetry operation combinations produces the 230 different space groups [69].

The symmetry elements within a crystal structure define a set of symmetry equivalent positions, which generates new atoms within the unit cell. These positions are called Wyckoff positions, and can be split into either special positions or general positions. General positions do not lie on any symmetry element, and will be related by symmetry to the maximum number of other positions within the unit cell. The maximum number of symmetry equivalent positions is determined by the spacegroup. A special position lies on a symmetry element without a transitional component (such as on a mirror plane or on a rotation axis). The corresponding symmetry operation leaves the point unchanged and no new atom is placed. The number of atoms generated by an atom at a particular position is called the site multiplicity. Each spacegroup has an associated set of Wyckoff positions, and each Wyckoff position is identified by the site multiplicity and a letter [69].

2.6.4 Pearson Notation

In this thesis, crystal structures will be described using Pearson notation, which describes the crystal structure using 2 letters and 1 number. The first letter in lower case italics indicates the crystal lattice: a = triclinic, m = monoclinic, o = orthorhombic, t = tetragonal, h = hexagonal/rhombohedral, c = cubic. The second letter in upper case italics indicates the unit cell centering or lattice centering of the crystal: S, A, B, C = Centering on a particular face, P = Primitive, I = Body centred, F = Face centred, R = Rhombohedral. Finally, the number refers to the number of atoms in the conventional unit cell. However, Pearson notation does not give any indication of the unit cell's space group. Some examples include, $cF4$, $hP2$ and $cI2$ which describe the fcc, hcp and bcc structures respectively.

2.7 X-ray Diffraction

2.7.1 X-ray Diffraction Physics

X-ray diffraction is one of the most used techniques to determine structural information about crystalline solids. The intense peaks of scattered x-rays from matter were first explained and demonstrated by father and son, William Henry Bragg and William Lawrence Bragg [72].

William Lawrence Bragg considered the crystalline solid as planes of atoms spaced distance d apart, and assumed the angle of reflection equalled the angle of incidence. Under these conditions the scattered radiation from one plane would interact both constructively and destructively with the other planes. The conditions for constructive interference, or observable reflections, is if the path difference between scattered radiation from 2 different planes is equal to an integer number of wavelengths. This condition is called Bragg's Law:

$$n\lambda = 2dsin\theta \tag{2.11}$$

where n in the order of reflection, λ is the wavelength and θ is the angle of reflection and incidence. A point to note is that there are multiple ways of defining planes from the lattice and each way will produce further reflections.

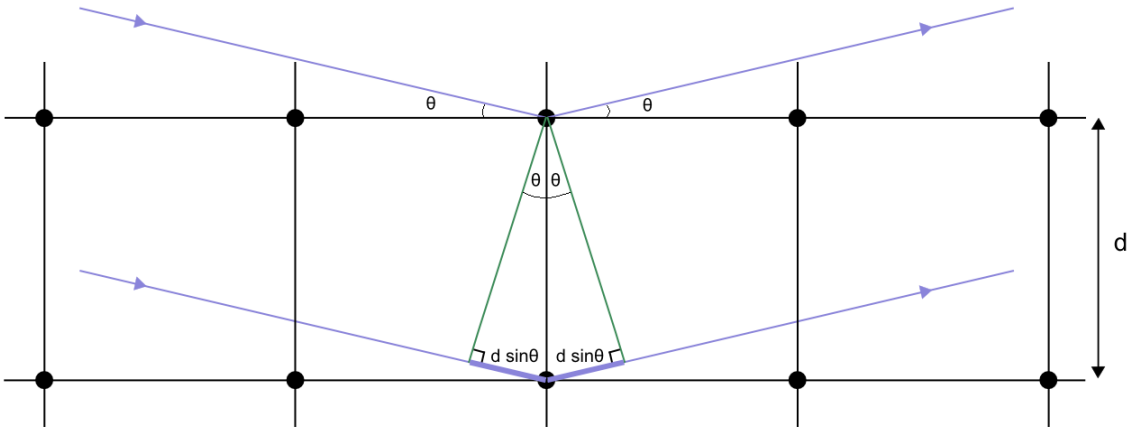

Figure 2.11 *A Bragg reflection from a set of atomic planes, separated by distance d.*

The von Laue formalism is another approach to describe x-rays scattering from a periodic structure. In this formulation there is no assumption of how the lattice

planes are defined, nor is the incident angle assumed to be equal to the reflection angle. Consider an incident x-ray travelling in direction $\hat{\mathbf{n}}$ with wave vector $\mathbf{k} = 2\pi\hat{\mathbf{n}}/\lambda$, which is scattered by 2 points spaced distance $\mathbf{d}$ apart, with the scattered wave travelling in the $\hat{\mathbf{n}}'$ direction with wave vector $\mathbf{k}' = 2\pi\hat{\mathbf{n}}'/\lambda$. Provided that the path difference between the scattered radiation from both points is equal to an integer number of wavelengths, constructive interference will occur.

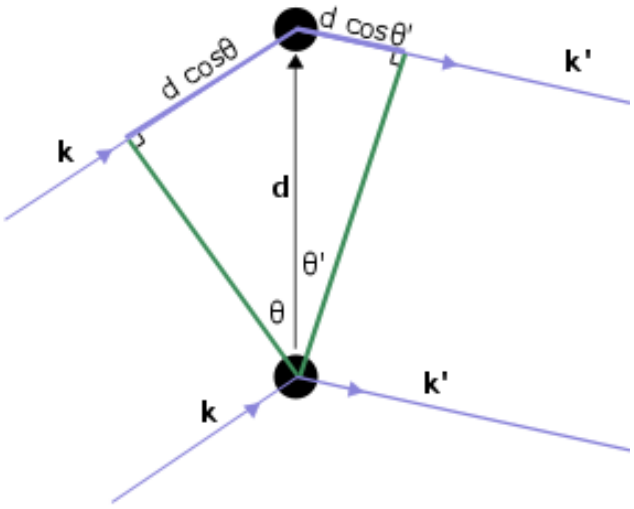

Figure 2.12 *Two incident waves with wave vectors $\boldsymbol{k} = 2\pi\hat{\mathbf{n}}/\lambda$ being scattered by two points, separated by **d**.*

From Figure 2.12, the path difference is equal to d cosθ + d cosθ' or $\mathbf{d}\cdot(\hat{\mathbf{n}}$ - $\hat{\mathbf{n}}')$. The condition for constructive interference is therefore: $\mathbf{d}\cdot(\hat{\mathbf{n}}$ - $\hat{\mathbf{n}}') = \mathrm{m}\lambda$. Multiplying both sides by $2\pi/\lambda$ and using $\mathbf{k} = 2\pi\hat{\mathbf{n}}/\lambda$ returns the constructive interference condition in terms of the incident and scattered wave vectors.

$$\mathbf{d} \cdot (\mathbf{k} - \mathbf{k}') = 2\pi m \tag{2.12}$$

where m is an integer number.

When applied to a Bravais lattice, Equation 2.12 is valid for all $\mathbf{d}$ that are a lattice vector. Extending this analysis to a crystalline solid which is considered to be made up of identical microscopic objects placed at position $\mathbf{R}$, the condition for constructive interference is:

$$\mathbf{R} \cdot (\mathbf{k} - \mathbf{k}') = 2\pi m \tag{2.13}$$

or equivalently

$$e^{(\mathrm{i}\mathbf{R}\cdot\mathbf{K})} = 1 \tag{2.14}$$

where $\mathbf{K}$ is the change in wave vector $\mathbf{k} - \mathbf{k}'$, and $\mathbf{R}$ is a Bravais lattice vector.

The conditions for constructive interference can be broken down further:

$$\begin{aligned} \mathbf{a}\cdot\mathbf{K} &= 2\pi h \\ \mathbf{b}\cdot\mathbf{K} &= 2\pi k \\ \mathbf{c}\cdot\mathbf{K} &= 2\pi l \end{aligned} \tag{2.15}$$

All of Equations 2.15 must be statisfied for constructive interference to occur, and are collectively called the Laue conditions for diffraction [73].

The Laue conditions are satisfied if the change in the wave vector $\mathbf{k}-\mathbf{k}'$ is itself a vector of the reciprocal lattice, $\mathbf{G}$. Assuming elastic scattering conditions $\mathbf{k}$ and $\mathbf{k}'$ must have the same wavelength and magnitude. Therefore, the component of $\mathbf{k}$ along $\mathbf{K}$ must exactly equal K/2. Therefore an incident wave vector will satisfy the Laue condition if the tip of $\mathbf{k}$ lies in a plane that is perpendicular to $\mathbf{K}$ and the plain intercepts $\mathbf{K}$ halfway along $\mathbf{K}$ [74].

The net scattering amplitude, A_G, for a given $\mathbf{K} = \mathbf{G}$ can be written as the sum of all the scattering from all atoms [73]. The position of the n^{th} atom can be written as $\mathbf{R_n} = (x_i + x_j)\mathbf{a} + (y_i + y_j)\mathbf{b} + (z_i + \mathrm{z_j})\mathbf{c}$ where (x_i, y_i, z_i) is the position of the i^{th} lattice point and (x_j, y_j, z_j) is the position of the j^{th} atom relative to the unit cell vectors $\mathbf{a}$, $\mathbf{b}$, and $\mathbf{c}$. This allows the sum over n atoms to be factorised into two separate sums: one over all lattice vectors i, and the other over all atoms j within the unit cell [73].

$$A_\mathrm{G} = \sum_{n=1} f_n e^{\mathrm{i}\mathbf{G}\cdot\mathbf{R}_n} \tag{2.16}$$

$$= \sum_{i=1} e^{2\pi\mathrm{i}(hx_\mathrm{i}+ky_\mathrm{i}+lz_\mathrm{i})} \sum_{j=1} f_\mathrm{j} e^{2\pi\mathrm{i}(hx_\mathrm{j}+ky_\mathrm{j}+lz_\mathrm{j})} \tag{2.17}$$

$$= \sum_{i=1} e^{2\pi\mathrm{i}(hx_\mathrm{i}+ky_\mathrm{i}+lz_\mathrm{i})} F \tag{2.18}$$

where $F = \sum_{j=1} f_\mathrm{j} e^{2\pi\mathrm{i}(hx_\mathrm{j}+ky_\mathrm{j}+lz_\mathrm{j})}$ and is called the structure factor.

The intensity of a reflection is proportional to the net scattering amplitude squared $|A_{\mathrm{G}}|^2$. Systematic absences are reflections that have zero intensity, and can be determined from the exponent of Equation 2.16. The last term f_{j}, is the atomic form factor and is the x-ray scattering contribution for an element of the electron cloud integrated over the whole cloud, and is inversely proportional to θ. The atomic form factor is at a maximum at $\theta = 0$, and is equal to the Z of the atom. The scattering from the atom is proportional to the Fourier transform of the electron density distribution around the atom [75].

$$f_{\mathrm{j}}(\mathbf{K}) = -\frac{1}{e}\int_V e^{2\pi \mathrm{i}\mathbf{K}\cdot\mathbf{r}}\rho_{\mathrm{j}}(\mathbf{r})d\mathbf{r} \tag{2.19}$$

A more intuitive graphical representation of the von Laue scattering condition was developed by Ewald, called the Ewald Sphere or the Ewald circle in 2-D. For a given lattice point and incident wave vector $\mathbf{k}$, the Ewald Sphere maps out a sphere containing every possible $\mathbf{k}'$, and hence $\mathbf{K}$. A diffraction peak will be observed if the origin of the incident wave and any other lattice point are on the surface of the sphere, $\mathbf{K}$ is then equal to a lattice vector since $\mathbf{K}$ connects two lattice points.

Using trigonometry and Figure 2.13 returns the following: $\sin\theta = K/2k$, since k is equal to $2\pi/\lambda$, and remembering that the magnitude of $\mathbf{K}$ is equal to $2\pi/d$ gives $\sin\theta = \lambda/2d$, which can be rearranged to return Bragg's law. The equivalence of the Bragg and von Laue scattering conditions demonstrates the comparison between a reflection for a family of atomic planes in real space and lattice points in reciprocal space.

Generally the von Laue scattering condition will only be satisfied by one or two lattice points at any one time, if any at all. There are a few ways of exploring reciprocal space to observe more reflections. If an incident beam is polychromatic, called a white beam, the Ewald sphere becomes a shell. Any lattice point contained within the shell satisfies the von Laue condition and will produce a Bragg peak. The 2$^{\mathrm{nd}}$ method is to fix the direction and wavelength of the incident x-rays and rotate the crystal around an axis. This fixes the size of the Ewald sphere, and causes the reciprocal lattice to rotate. During the rotation each reciprocal lattice point draws a circle in k-space and satisfies the von Laue condition when a lattice point intercepts the Ewald sphere.

The last method, called the Debye-Scherrer Method, rotates the sample around

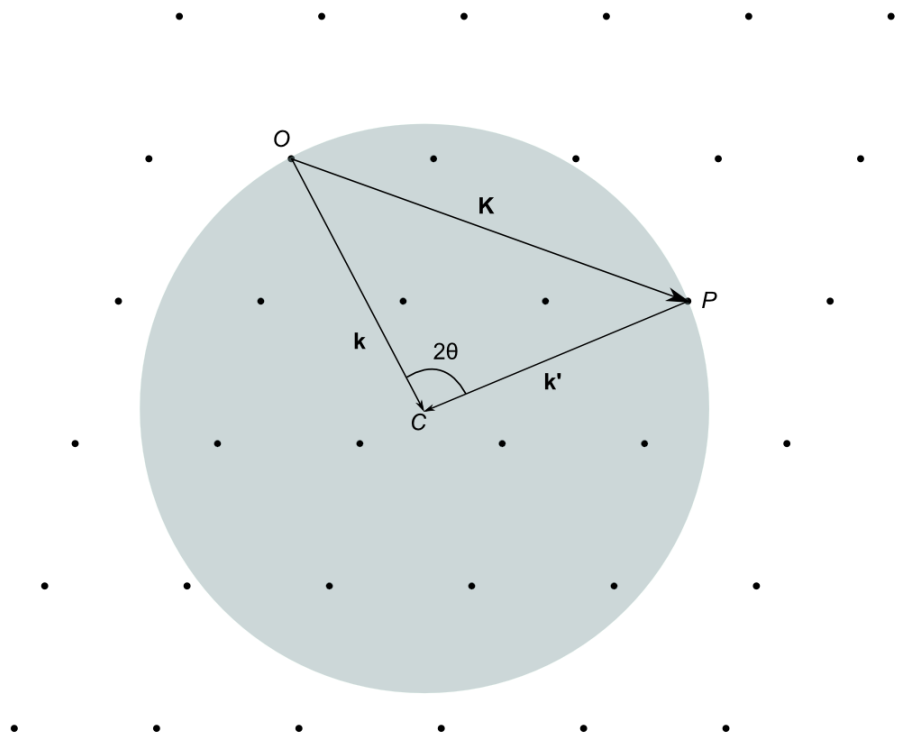

Figure 2.13 *The Ewald construction in 2-D which has all possible values for* ***K*** *for a monochromatic x-ray beam.*

a rotation axis which is able to orientate in any direction, which in practice, is achieved by placing a powdered sample within a fixed x-ray beam. The grains of a powdered sample are randomly orientated, which is equivalent to changing the direction of the rotation axis, and produces a pattern containing the sum of all possible orientations of a crystal. Each lattice point maps out a sphere of radius R around the origin, and will always intercept the Ewald Sphere, slicing out a circle provided that the R is less then $2k$ (the sphere mapped out by the lattice point is larger than the Ewald Sphere). Bragg reflections will occur for $\mathbf{K}$ that connects the circle to the origin. Thus $\mathbf{K}$ maps out a cone of scattered radiation.

The cone of intensity is captured by a 2-D detector as a circle if the detector is perpendicular to the beam, called a Debye-Scherrer ring. A powder diffraction pattern consists of multiple Debye-Scherrer rings. The major problem with powder diffraction is the 3-D information of the crystal structure is reduced to 1-D as the data is projected onto the detector. The only information that can obtained from a powder pattern is the d-spacing of the rings and their intensities. For simple patterns, this restriction is not a huge problem. However, when analysing complex patterns, reflections can overlap resulting in only 1 ring being

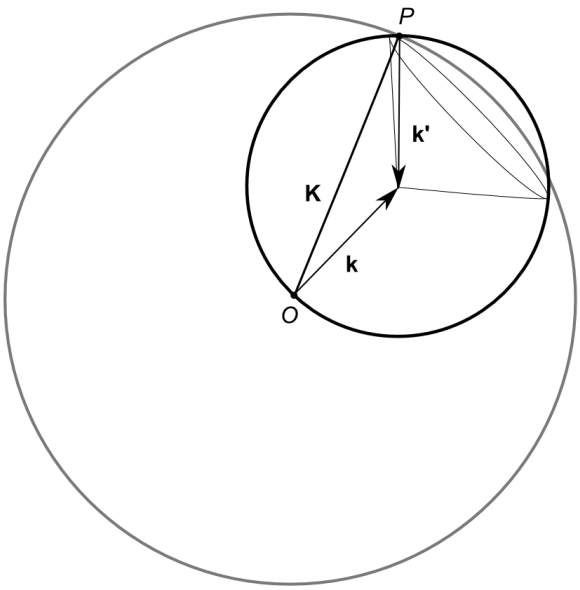

Figure 2.14 *The Ewald construction in 3-D. The grey sphere is generated by the lattice point O, and the black sphere is the Ewald sphere. The two spheres intercept in a circle (compressed to an ellipse). The Laue condition is satisfied for all points that K goes through the circle that intercepts both spheres.*

observed compared to multiple spots in the diffraction pattern. Single crystal diffraction does not have this restriction, and since it is possible to determine the orientation, each reflection can be uniquely identified. There are other difficulties with obtaining diffraction data at high pressure from single crystals. If the crystal undergoes a first order phase transition it is very unlikely that the sample will remain a single crystal after the transition. It is possible to grow a single crystal of a high-pressure phase directly in the DAC. One method is to melt a powdered sample, then attempt to solidify the sample back into a single crystal [76]. It is also possible for a sample to undergo a phase transition into a single crystal under hydrostatic conditions by slowly compressing the sample through the phase boundary [77]. However, this is sample dependant, and it is not always possible to acquire a single crystal of a high-pressure phase.

2.7.2 X-ray Generation

It is possible to generate x-rays in a university laboratory using an x-ray tube. Electrons are generated from a heated filament, and accelerated towards a metal anode. When the electrons hit the anode, bremsstrahlung radiation is emitted as

the electron slows down and is eventually stopped. Additionally, when an emitted electron collides with an anode atom, an atomic electron can be promoted from an inner electron shell creating a vacancy. This vacancy is then filled by an outer shell electron, emitting fluorescence radiation with discrete wavelengths in the process. The fluorescence radiation generated from an electron falling from the L shell (principle quantum number 2) to the K shell (principle quantum number 1) is called the K_α line, and is much more intense than the bremsstrahlung radiation. While it is convenient to perform experiments in-house, there are various downsides. It is not possible to continuously change the wavelength of the radiation emitted, and only the small fraction of x-rays that are emitted within a small angular range can be utilised to form an incident beam [78]. For high-pressure experiments it is much more useful to take samples to a synchrotron facility. All of the data collected for this thesis were taken at such facilities: the Diamond Light Source (DLS) in the United Kingdom, the European Synchrotron Radiation Facility (ESRF) in France, the Deutsches Elektronen-Synchrotron (DESY) in Germany and the ALBA synchrotron in Spain.

A synchrotron facility produces electromagnetic radiation in intensities 11 orders of magnitude higher than an x-ray tube. This allows data from very small samples to be collected very rapidly. Choosing a shorter wavelength permits larger areas of reciprocal space to be accessed, while selecting a longer wavelength separates out the diffraction peaks, allowing easier observation of reflections with similar d-spacings. Another advantage over lab sources is the lower beam divergence, which greatly improves the data quality by reducing the peak width and improving the signal to noise ratio. This particular advantage is vital for distinguishing doublet and triplet peaks, and identifying weak reflections from background noise. Various aspects of the resulting x-ray radiation beam can be combined into a single quantity called brilliance, which is defined as the number of photons emitted per second, of a particular wavelength and direction in a particular area. Brilliance considers the collimation of the beam, or how the beam diverges as it propagates through space. The collimation is measured in mrad in both the horizontal and vertical direction. Ideally, the beam has as small a cross section as possible, inversely proportional to brilliance and is typically measured in mm^2. Finally, some sources produce very smooth spectra, while other sources have peaks at particular wavelengths. By convention, the range of wavelengths that contribute to the measured brilliance must be within 0.1% of the chosen wavelength.

A synchrotron generates electrons by heating a metal (usually tungsten) causing electrons to be ejected from the surface. The electrons are then caught using a positive electric field applied close to the surface of the metal, and are accelerated toward a linear accelerator (linac). The linac is a series of units containing electric fields with changeable charges. When the electrons reach the linac the charge of the electric field is flipped to negative which pushes the electrons towards the next positively charged unit. By this method the linac accelerates the electrons to 99.99% the speed of light, with an energy on the order of a 100 MeV. In this state the electrons are fed into a booster ring which increases the electron energy to 3-6 GeV [69, 79–82].

The electrons are ejected into the storage ring, which are then kept at constant energy and are manipulated by bending magnets to focus and direct the beam in an arc. When the direction of the beam changes, a continuous spectrum of radiation is emitted. In order to maximise the quantity of radiation produced, insertion devices are placed in the straights between the bending magnets. An insertion device is an array of magnet pairs with alternating polarity, which cause the electrons to oscillate. Insertion devices are classified as either a wiggler or an undulator. A wiggler causes the electrons to move through a series of small arcs, and at each arc more radiation is emitted in a cone shape. The spectrum of the radiation emitted due to the wiggler's magnetic field is comparable to a bending magnet of similar field strength. Since there is very little overlap between the cones, the radiation is superimposed on each other and the intensity of the beam is hugely increased. An undulator operates in a similar fashion to a wiggler, but has much smaller oscillation amplitudes. Radiation from each pair of magnets interferes with each other, which results in the amplitudes of the emitted radiation being combined. This produces a collimated, quasi-monochromatic stream of radiation at a particular wavelength. In summary, a wiggler produces much more radiation than an undulator over a wide spectrum, resulting in a continuous, uniform brilliance, but for a specific wavelength the undulator has a higher brilliance than the wiggler.

The maximum angular deviation from the axis parallel to the beam direction, called the K-factor, is used to characterise the insertion device as either a wiggler or an undulator [69, 78]:

$$K_{\mathrm{f}} = \frac{eB_{\mathrm{M}}\lambda_{\mathrm{U}}}{2\pi\gamma_{\mathrm{L}}m_{\mathrm{e}}v_{\mathrm{c}}} \tag{2.20}$$

where K_f is the K-factor, where e is the electron charge, λ_U is the magnetic period, γ_L is the Lorentz factor, m_e is the electron's mass and v_c is the speed of light. If $K_\mathrm{f} > 1$ then the insertion device is classified as a wiggler, if $K_\mathrm{f} < 1$ then it is an undulator. The x-ray radiation enters the optics hutch where the beam is manipulated to suit the experiment. The radiation diffracts through a double crystal monochromator, which is rotated to select a single wavelength. The beam is manipulated and focused by various optics, before entering into the experimental hutch where it is further refined. The beam then reaches the sample and is diffracted by the sample towards a detector.

2.7.3 Structural Refinements

Le Bail [83] and Rietveld [84] refinements are methods commonly used to fit an integrated diffraction pattern, or diffraction profile, to a profile generated from a theoretical model. The entire diffraction profile is used to constrain and refine the model's structural parameters by minimising a least-squares residual S, until the model's profile matches the diffraction profile.

$$S = \sum w_i |I_\mathrm{io} - I_\mathrm{ic}|^2 \tag{2.21}$$

where I_io is the observed intensity at point i, I_ic is the intensity calculated by the model at point i and w_i is the weight.

In a Le Bail refinement the lattice parameters (a, b, c, α, β, γ), peak shape and background are varied to match the generated profile to the observed profile. The atomic positions are not considered in this refinement, so only the lattice parameters and spacegroup can be determined from a Le Bail refinement. In a Rietveld refinement, the atomic positions are also varied to change the calculated peak intensities, meaning a crystal structure can be fully determined.

The first step is to index the diffraction profile and assign each peak (hkl) values. This involves deciding which of the 7 crystal systems to use, determining values for the lattice parameters (a, b, c, α, β and γ), and determining the background. Systematic absences can then be utilised to determine which space group best suits the profile.

The second step is to extract the structure factors from the peak intensities. The whole profile is utilised to refine the peak heights and positions for each

of the reflections. Peaks which are composed of multiple overlapping reflections can be broken down, and the contribution from each reflection can be calculated separately. There are many choices of peak shape which can be used to model the reflection peaks. In this thesis a pseudo-Voigt (pV) peak shape was used to fit data [85], which can be described a combination of a Gaussian (G) (see Equation 2.23) and a Lorentzian (L) (see Equation 2.24).

$$pV = (\eta)G + (\eta - 1)L \tag{2.22}$$

where η is a number between 0 and 1.

$$G = \frac{(4\ln(2))^2}{\sqrt{\pi}H} \exp\left[-4\ln(2)\frac{2\Delta\theta^2}{H}\right] \tag{2.23}$$

$$L = \frac{2}{\pi H}\left[1 + 4(\frac{2\Delta\theta}{H})^2\right]^{-1} \tag{2.24}$$

where H is the full width at half maximum and $\Delta\theta$ is the difference between measured θ and the Bragg angle.

While it is possible to refine Equation 2.22 by slowly varying η and H, it is much more common to directly modify H in Equation 2.23 and Equation 2.24 separately. H_{G} and H_{L} are described in Equations 2.25 [86] and 2.26 [87].

$$H_{\mathrm{G}} = (U\tan^2\theta + V\tan\theta + W)^{1/2} \tag{2.25}$$

$$H_{\mathrm{L}} = X\tan\theta + Y/\cos\theta \tag{2.26}$$

where U, V, W, X and Y are the variable parameters in the refinements.

While an ideal powdered sample will have a perfectly random distribution of crystallite orientations, such a sample is very difficult to achieve in practice. This is especially true in high-pressure experiments, since upon compression the grains become much more tightly packed, forcing the grains to orientate in a particular direction. Preferred orientation can change a bragg reflection's intensity, and is accounted for by multiplying the calculated intensity with an empirical function P_{k}, which is dependent on the acute angle between the preferred orientation plane

and the diffracting plane, ϕ. P_{k} can be a Gaussian [88] or trigonometric [89]:

$$P_{\mathrm{k}} = \exp(-p\phi^2) \tag{2.27}$$

$$P_{\mathrm{k}} = (p^2 \cos^2 \phi + \sin^2 \phi/p)^{-3/2} \tag{2.28}$$

where p is a refinable parameter.

Finally, the structural model $|F_{\mathrm{calc}}|$ is refined by optimising the model parameters to match the profile $|F_{\mathrm{obs}}|$ as accurately as possible. It should be noted that a Rietveld refinement will never produce a better fit compared to a Le Bail refinement. There are various measures of the goodness of fit [85]:

$$R_{\mathrm{p}}^2 = \frac{\sum ||F_{\mathrm{obs}}| - |F_{\mathrm{calc}}||}{\sum |F_{\mathrm{obs}}|} \tag{2.29}$$

where R_{p} is the conventional profile R-factor.

$$wR_{\mathrm{p}}^2 = \frac{\sum w(|F_{\mathrm{obs}}|^2 - |F_{\mathrm{calc}}|^2)^2}{\sum w|F_{\mathrm{obs}}|^2} \tag{2.30}$$

where wR_{p}^2 is the weighted profile R-factor.

$$\chi^2 = \frac{R_{\mathrm{wp}}^2}{R_{\mathrm{exp}}^2} = \sqrt{\frac{\sum w(|F_{\mathrm{obs}}|^2 - |F_{\mathrm{calc}}|^2)^2}{N - P + C}} \tag{2.31}$$

where R_{exp} is the expected value of wR_{p} assuming the observed data is the best possible, N is the number of data points, P is the number of parameters refined and C is the number of constraints [90, 91].

Chapter 3

The Lanthanide Metals

3.0.1 Introduction

The lanthanide series are a group of elemental metals starting at lanthanum with atomic number 57 and ending with lutetium at atomic number 71. As the periodic table is traversed, the $4f$ shell is slowly filled, which relates to the interesting material properties the lanthanide series possesses. The lanthanide metals are divided into groups based on their valency, with almost all of the lanthanide metals being 'regular' trivalent members, excluding divalent Eu and Yb, and Ce, which behaves uniquely compared to the others. This thesis discusses the high-pressure high-temperature behaviour of 3 members of the lanthanide metals: La, Ce and Gd as determined using x-ray diffraction.

3.1 The Trivalent Lanthanides

As said, the lanthanide series of metals are characterised by the gradual filling up of the localised $4f$ electron shell, which is shielded by the outer $6s$ and $5d$ shells. Due to this shielding effect, the $4f$ electrons do not take part in atomic interactions, which are governed by the outer $6s$ and $5d$ electrons. The lanthanides' electronic properties are largely similar to each other, with any differences being attributed to the different number of $4f$ electrons. The majority of the lanthanide metals (La to Lu, excluding Eu and Yb) are grouped into the "regular" trivalent lanthanides, which have the following electronic structure at

ambient conditions [Xe]$6s^2 5d^1 4f^n$, with the $4f$ shell being filled as the Z number increases. In the cases of divalent Eu and Yb, the $5d$ electron is promoted to the $4f$ shell instead with electronic configuration [Xe]$6s^2 4f^7$ and [Xe]$6s^2 4f^{14}$, respectively [92]. Due to the extra proton in the nucleus and the extra electron in the $4f$ shell, the lanthanide atoms contract as the atomic number increases. The contraction is due to the increased Coulomb force acting on the atom, and the phenomena is called the lanthanide contraction [93].

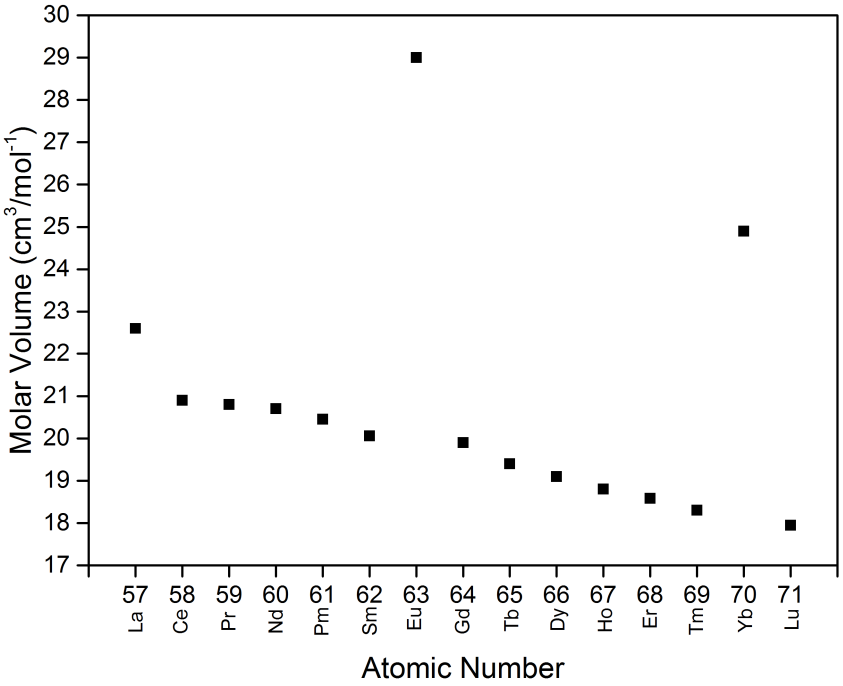

Figure 3.1 *Graph of the atomic volume at ambient conditions vs Z for the lanthanide metals, highlighting anomalously high volumes of divalent Eu and Yb. Image recreated from [94].*

Since the trivalent lanthanide metals are electronically similar, structural trends are observed across the series. The lighter elements (La, Pr, Nd and Pm) crystallize in the dhcp structure at ambient conditions; Sm exhibits the Sm-type structure; and the heavier members (Gd - Lu) all assume the hcp structure (see [15] and the references contained within). This trend is reversed upon compression, the heavier lanthanides transforming from hcp to the Sm-type and dhcp structures found in the lighter members at ambient conditions. The close-packed structures adopted by the lanthanide metals at lower pressures (hcp $\rightarrow$ Sm-type $\rightarrow$ dhcp $\rightarrow$ fcc) only differ by the layer stacking sequence each structure has (see Table 3.1 and Figure 3.2).

Upon further compression, the lanthanide metals transform into a distorted fcc (d-

fcc) phase not seen at ambient pressure in any trivalent lanthanide. At extremely high pressures the lanthanides undergo a transformation to one or more low-symmetry phases, accompanied by a sudden, sharp decrease in volume, which is attributed to the $4f$ electrons becoming de-localised [15]. Johansson *et al.* described the sequence as a change in parameter F, defined as the ratio of the ionic radius (R_{I}) and the Wigner-Seitz radius (R_{ws}), $F = R_{\mathrm{ws}}/R_{\mathrm{I}}$. F increases as Z increases but, on compression, R_{ws} will get smaller, since the valence electrons will have less space to occupy, while R_{I} remains relatively unchanged, which causes F to decrease. Therefore, if pressure is applied on a heavier lanthanide, for example dysprosium, it is possible to reduce F so it is comparable to F from a lighter lanthanide, for example neodymium, at lower pressures, [92]. Duthie *et al.* showed that F is a measure of the number of d electrons, indicating that the transformations through the various close packed phases are due to an $s \rightarrow d$ like transition [95]. This transition is also found in yttrium, and the comparison of F between yttrium (which has no $4f$ electrons) and the heavier lanthanides (Gd - Lu), shows remarkable similarities [96].

Table 3.1 *Table comparing the various atomic layer stacking found in the close packed structure adopted by the lanthanide elements [97, 98].*

Structure	Space-group	Stacking Layer
hcp	$P6_3/mmc$	AB
Sm type	R-3m	ABABCBCAC
dhcp	$P6_3/mmc$	ABAC
fcc	Fm-3m	ABC

Since all of the trivalent lanthanide metals have similar phase transformations, they are said to undergo a common phase transition sequence (hcp $\rightarrow$ Sm-type $\rightarrow$ dhcp $\rightarrow$ fcc $\rightarrow$ d-fcc $\rightarrow$ "volume collapsed" phase). Many studies have focused on Ce and Pr, since the d-fcc and "volume collapsed" structures are adopted at much lower pressures compared to other lanthanide metals. As a result, structural assignment of the d-fcc and "volume collapsed" phases found in the heavier members relies on the better quality of data collected on the lighter members, which will be referred to as "analysis by analogy". However, there are very subtle differences between the different structures proposed for the d-fcc and "volume collapsed" phases, which can result in an incorrect structural assignment. To further complicate the problem, there are some structures that are not universal to the series and are only adopted by particular lanthanides, such as the $hP3$ structure found in Nd [100]. The d-fcc and "volume collapsed"

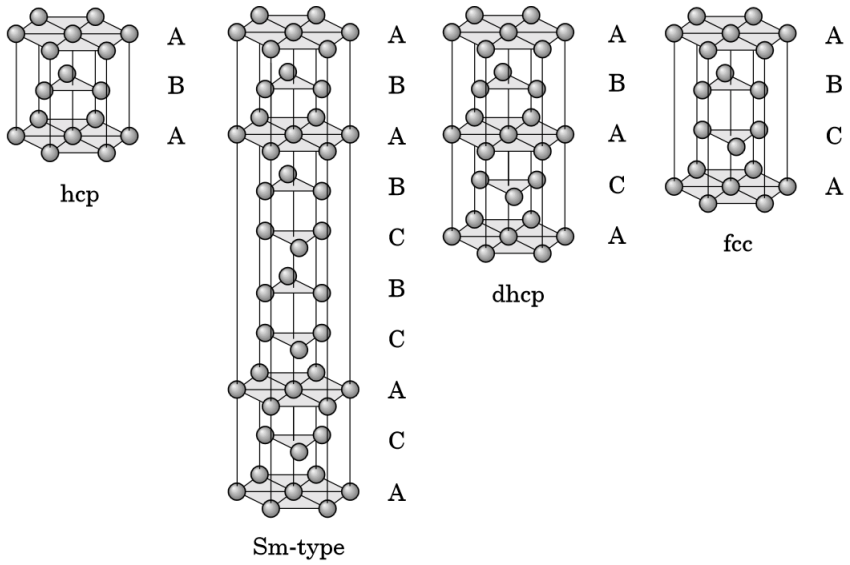

Figure 3.2 *Diagram of the different stacking layers found in the close packed structures adopted by the lanthanide metals. Image modified from ref [99].*

phases, and their structures, are considered separately in more detail in sections 3.2 and 3.3 respectively.

3.2 The Distorted-fcc Phase

After transforming through the various close-packed structures, all of the trivalent lanthanide metals (La to Lu, excluding Eu and Yb) adopt a structure which can be described as a distortion of the fcc structure, with the atoms slightly displaced from the ideal fcc positions. In the heavier lanthanides single-phase fcc patterns are not observed, and the heavier lanthanides transform directly to the d-fcc phase from the dhcp phase ([15] and the references there in). The transition to the fcc phase appears to be suppressed in Gd if a pressure transmitting medium (see section 2.4) is not used [18, 101], suggesting that non-hydrostatic conditions prevent the transformation to the fcc phase. The onset of the phase transformation to the d-fcc phase is accompanied by the appearance of additional weak non-fcc super lattice reflections, and the splitting of various fcc peaks. In general, the more intense weak reflections are observed first, and only when the sample pressure is far beyond the fcc $\rightarrow$ d-fcc phase boundary does the peak splitting becomes resolvable [11]. Krüger *et al.* [11] plotted the ratio of the intensity of the strongest weak peak ((105) indexed to the $hP6$ structure) with

the K_α intensity (see Section 2.7.2 for an explanation) against pressure, and showed that the super lattice reflections always emerged first before any peak splitting effects were observed (see Figure 3.3). Porsch *et al.* [102] confirmed similar behaviour in La, albeit at a lower pressure.

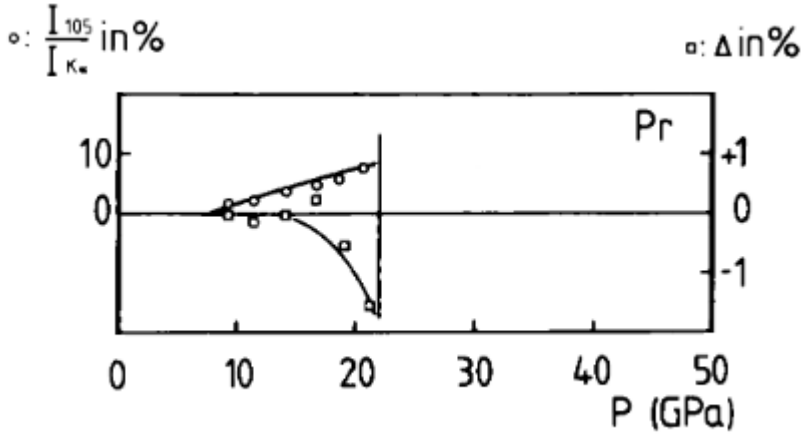

Figure 3.3 *Comparison between the intensity variation of the (105) super lattice reflection (circles) with the variation of the c/a ratio in the d-fcc phase (squares) of Pr. Image taken from [11].*

There are an infinite number of ways to displace the fcc atoms from their ideal positions. For instance, a distortion of the unit cell along the body diagonal, (the 111 direction) will cause the fcc (111) reflection become a doublet while the fcc (200) reflection remains a singlet. Some other examples are presented in Figure 3.4. It is vital to fully resolve as many of the closely-spaced doublets and triplets as possible, to assign the correct structure. It is also necessary to construct the correct supercell in order to account of all of the peak splittings and weak reflections.

The phase transition is regarded as a second order transition for the following reasons (see reference [104] and the references therein):

1. The fcc $\rightarrow$ d-fcc phase transition does not show hysteresis, either with pressure or temperature.

2. There is no detectable discontinuity in resistivity and volume at the phase transition.

3. The d-fcc phase is characterized by the appearance of additional weak reflections which indicates that there is an underlying superstructure, but

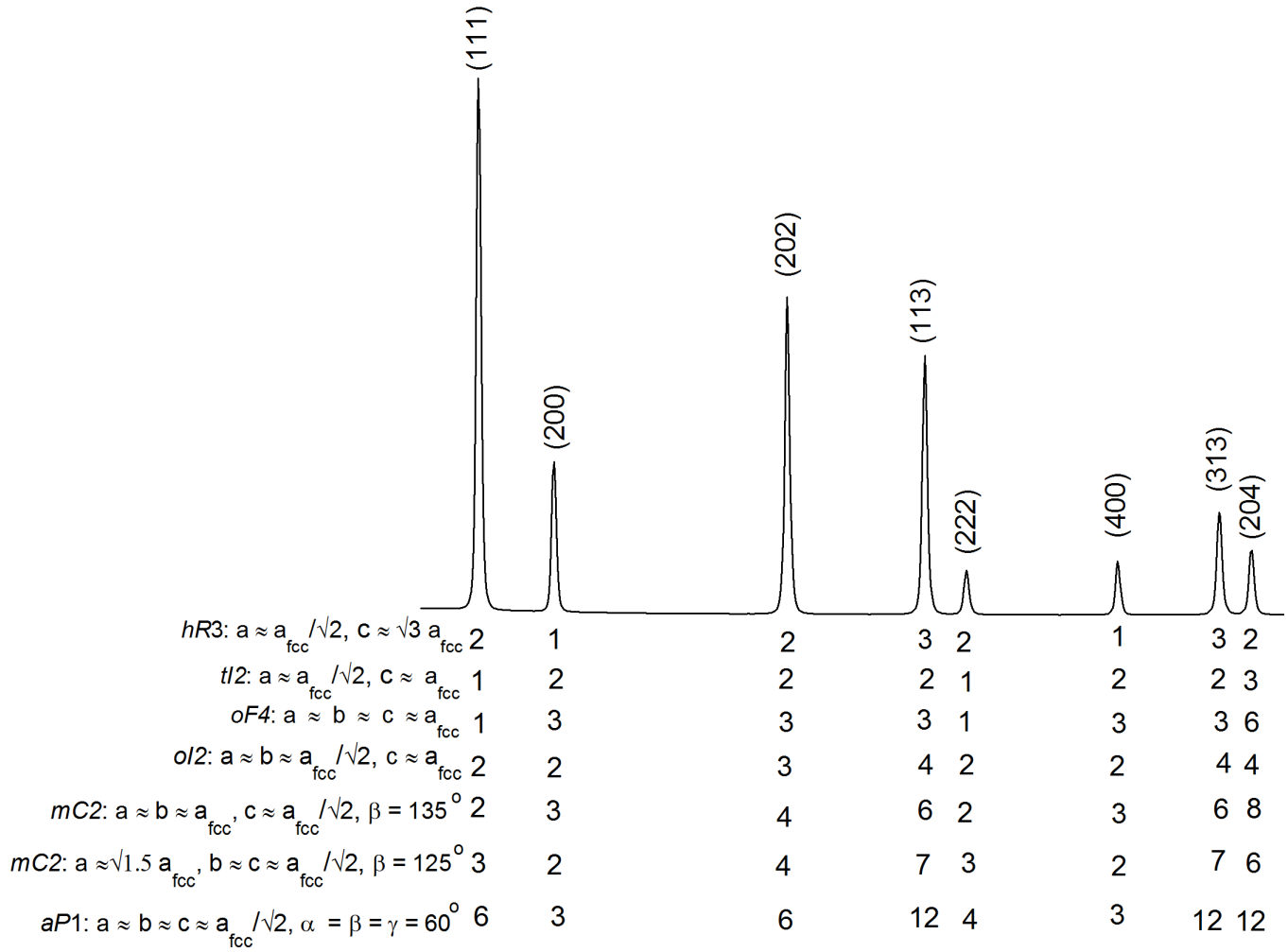

Figure 3.4 *Integrated diffraction profile of fcc Ce. The numbers indicate the extent of the peak splitting effect the fcc structure undergoes for various d-fcc structures [103]. For example, a transformation to the hR3 structure causes the fcc (111) peak to split into two peaks, while the fcc (200) peak remains unchanged. The Pearson symbol for each structure, and how each structure relates to the fcc structure, is presented at the left hand side.*

the fcc x-ray diffraction peaks do not disappear in the d-fcc phase. At high pressure the fcc reflections split into multiple weaker reflections.

4. The intensities of the d-fcc reflections vary over a wide range with pressure, and continuously go to zero at the reverse transition to the fcc phase.

Pr is the lightest lanthanide that adopts the d-fcc phase [105], at 7.4 GPa [106]. There have been many structures suggested for Pr's d-fcc phase, but the now commonly-accepted $hR24$ structure was first proposed Hamaya *et al.* [14]. Hamaya *et al.* observed the fcc (111), (220), (311) and (222) peaks splitting into doublets and triplets, signalling the formation of a rhombohedral lattice (see Figure 3.5). This lattice can be obtained by doubling the a, b and c axis of the hexagonal equivalent of the fcc structure. Hence, the $hR24$ structure can be described by a 2 by 2 by 2 supercell of the fcc structure [14].

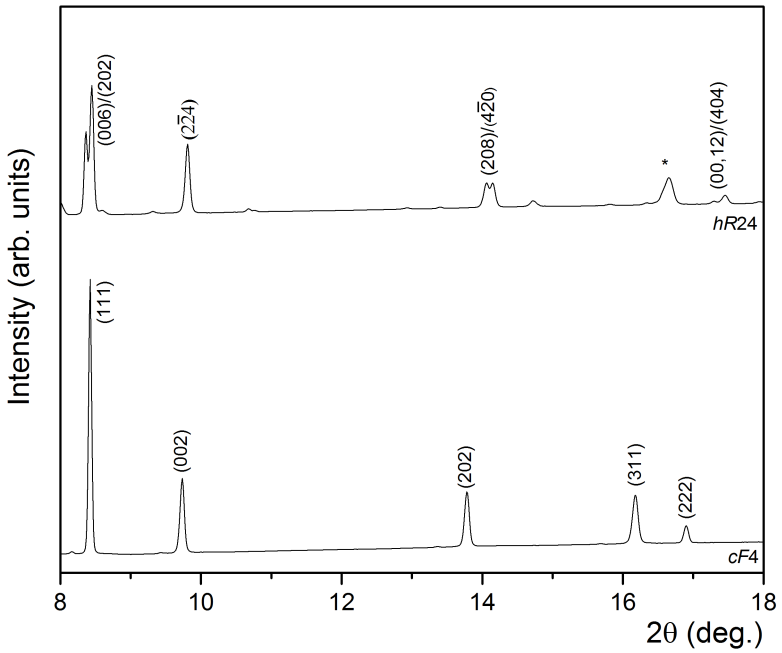

Figure 3.5 *Integrated diffraction profiles from the fcc and hR24 phases of La at 11 GPa and 23 GPa respectively at 445 K collected at the ESRF, emphasizing the fcc reflections splitting into multiple reflections. The asterisk indicates multiple diffraction peaks that can't be resolved fully in the hR24 diffraction profile. The hR24 integrated diffraction profile has been shifted in 2θ by 0.5° to aid comparison.*

Structure	Space-group	fcc Distortion	Wyckoff Positions	Atomic Coordinates
$oP16$	$Pmmm$	$a = b = \sqrt{2}a_{\mathrm{fcc}}$ $c = 2a_{\mathrm{fcc}}$	Not given	Not given
$hP6$	$P3_121$ or $P3_221$	$a = a_{\mathrm{fcc}}/\sqrt{2}$ $c = 2a_{\mathrm{fcc}}\sqrt{3}$	*6c*	Not given
$oC8(1)$	$Cmmm$	$a = 2a_{\mathrm{fcc}}$ $b = c = a_{\mathrm{fcc}}/\sqrt{2}$	*4j*, *4g*	(0,y,0.5), (x,0,0)
$oC8(2)$	$Cmma$	$a = 2a_{\mathrm{fcc}}$ $b = c = a_{\mathrm{fcc}}/\sqrt{6}$	*4g*, *4a*	(0,0.25,z), (0.25,0,0)
$hR24$	$R\bar{3}m$	$a = \sqrt{2}a_{\mathrm{fcc}}$ $c = 2a_{\mathrm{fcc}}\sqrt{3}$	*6c*, *18h*	(0,0,z_1), (x,-x,z_2)
$oI16$	$Ibam$	$a = 2a_{\mathrm{fcc}}$ $b = c = \sqrt{2}a_{\mathrm{fcc}}$	*8g*, *8j*	(0,y_1,0.25), (x,y_2,0)
$aP1$	$P\bar{1}$	$a = b = c = a_{\mathrm{fcc}}/\sqrt{2}$ $\alpha = \beta = \gamma = 60^{\mathrm{o}}$	Not given	Not given

Table 3.2 *Table showing some of the proposed structures to the d-fcc phase of La and Pr, with corresponding space-groups, how the structure relates to the fcc structure and atomic coordinates [14, 97, 103, 104, 106–109].*

It was only when Evans *et al.* performed a high resolution x-ray diffraction experiment on Pr to confirm the $hR24$ structure that it was possible to rule out previously proposed structures such as $oP16$ and $hP6$ [107, 108]. Evans *et al.* were able to confirm the $hR24$ structure due to the appearance of peaks which could be assigned to the (104), ($2\bar{1}6$) and (300) reflections predicted by the $hR24$ structure. The $hR24$ structure has the $R\bar{3}m$ space group and has atoms on the $6c$ (0, 0, z_1) and $18h$ (x, -x, z_2) Wyckoff positions. The $hR24$ structure is equivalent to the fcc structure when the c/a ratio = $\sqrt{6}$, $z_1 = 0.25$, $z_2 = 0.25$ and x = 0.5, and is now believed to occur in all of the trivalent lanthanide with the exception of Sm [16, 18, 96, 104–106, 110–114].

While the $hR24$ structure is reported in all of the heavier lanthanide metals, only Gd, Dy, Er and Tm have had full Rietveld refinements presented in the literature. By contrast, peaks from d-fcc Tb and Ho have been assigned (*hkl*) reflections, but a full Rietveld refinement was not presented. In the case of Dy, Samudrala *et al.* [96] showed diffraction patterns with weak peaks unaccounted for by the $hR24$ structure, but made no comment on these, nor offered an explanation to resolve the discrepancy. Shen *et al.* observed a singlet predicted by the $hR24$ structure splitting into a doublet, and determined the $oC8(1)$ structure best describes the d-fcc phase found in Dy [115].

When Pr is compressed to 13.7 GPa, a subtle transition to a different phase occurs, to which Evans *et al.* assigned the $oI16$ structure with the *Ibam* space group and atoms on the $8g$ (0, y_1, 0.25) and $8j$ (x, y_2, 0) Wyckoff sites [106]. Evans *et al.* pointed out that while the $oI16$ structure best fits the integrated diffraction patterns above 13.7 GPa, the new phase may have a lower symmetry than orthorhombic. In addition, the transition occurs over several GPa, and is only identified by the change in the relative intensities of the (006)/(202) and the (00,12)/(404) doublets (see Figure 3.6). A similar phenomena was also observed in Nd [106].

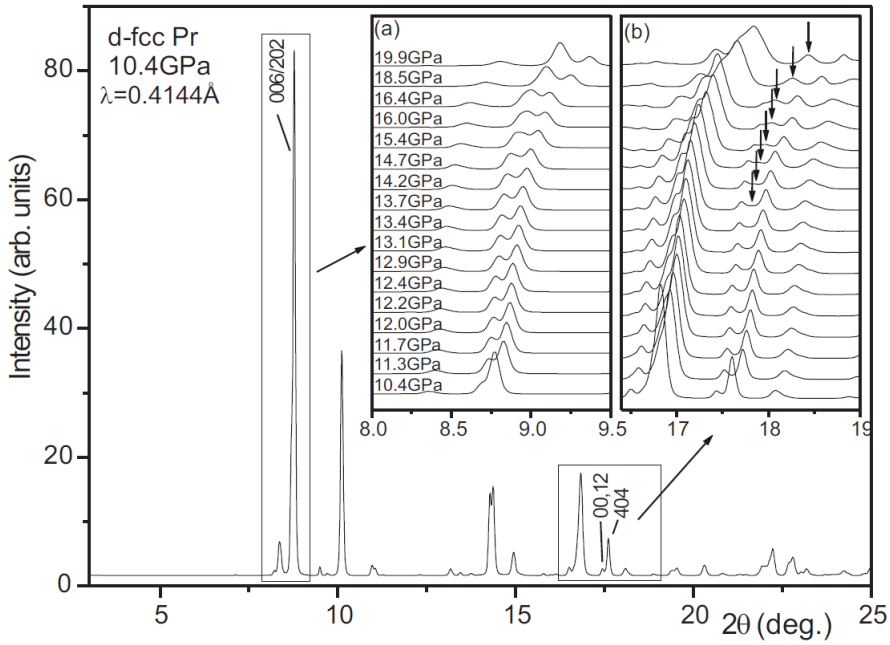

Figure 3.6 *Integrated diffraction profile of the d-fcc phase of Pr. The inserts show the change in peak intensities that indicate a transformation into the oI16 structure. The plot from Evans et al. [106].*

There are other indications of a d-fcc → d-fcc transition. Krüger *et al.* reported the c/a ratio of various lanthanide metals indexed to the $hP6$ structure up to 50 GPa [11]. While the c/a ratio of La, Gd and Tb remained largely consistent with the cubic c/a ratio under compression, the c/a ratio of Pr and Nd change dramatically at 14 and 27.5 GPa, similar to the $hR24 \rightarrow oI16$ transition pressures reported by Evans *et al.* There have been very few studies on the c/a ratios of the d-fcc phase aside from Pr, Nd and Ho [106, 111, 116]. Evans *et al.* reported the $hR24$ c/a ratio increasing with pressure, from the ideal cubic value of $\sqrt{6}$ at 7.5 GPa to 2.487 at 13.4 GPa [106]. By contrast, the c/a ratio of Tb's $hR24$ phase appears to decrease as pressure increases: Cunningham *et al.* reported a

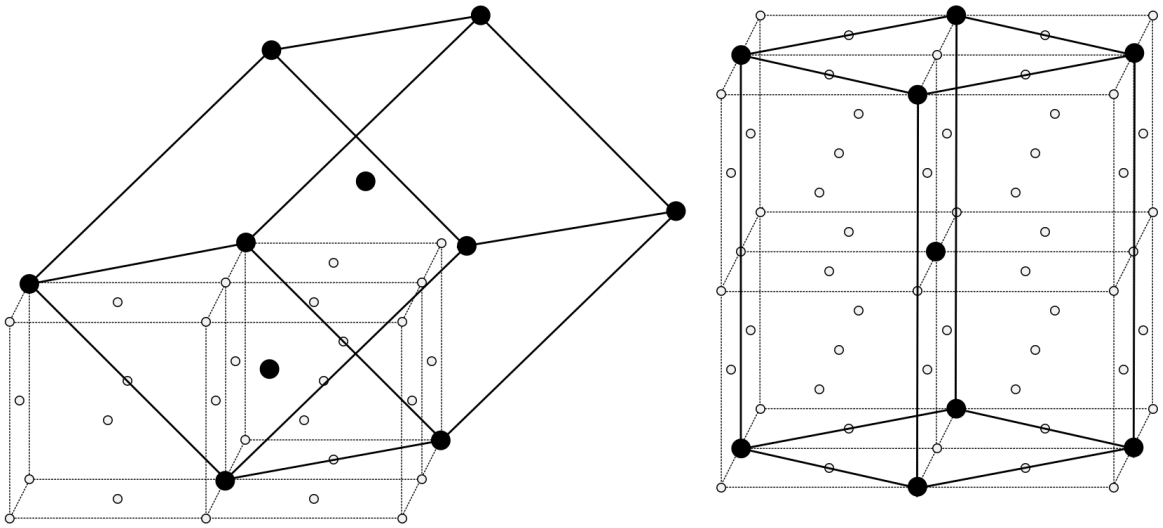

Figure 3.7 *The hR24 (left) and oI16 (right) structures. Both structures are drawn relative to the fcc structure, 3 unit cells of which are shown in the case of the hR24 structure and 8 for the oI16 structure. The lattice points of both the hR24 and oI16 structures are shown by black spheres, at (0, 0, 0), (0.67, 0.33, 0.33), (0.33, 0.67, 0.67) and (0, 0, 0), (0.5, 0.5, 0.5) respectively, while the fcc lattice points are represented by hollow spheres. The hR24 diagram was remade from Evans et al. [106].*

c/a value of 2.38 at 40.2 GPa. However, the 2θ of the (01,11) reflection is lower than the 2θ of the (226) reflection, which conflicts with the lattice parameters Cunningham *et al.* present. Cunningham *et al.* also observed a decrease in the $hR24$ c/a ratio from $\sqrt{6}$ as pressure increases in Ho, but with no obvious peak indexing errors. The behaviour of the $hR24$ structure upon compression appears to be different in different lanthanide metals.

3.3 The post Distorted-fcc Phase

Upon further compression the majority of the lanthanide metals transform into low-symmetry phases, and different structures are observed across the series. Nd and Sm transform into the $hP3$ structure at 35 GPa and 37 GPa respectively [116, 117], before transforming into the monoclinic structure, $mC4$, seen in Ce [118]. Both the $hP3$ and the $mC4$ structures can be described as a distortion of the fcc structure.

The relationship between the $hP3$ lattice parameters with a_{fcc} are $a = a_{\mathrm{fcc}}/\sqrt{2}$, c

$= \sqrt{3}a_{\mathrm{fcc}}$ with $(c/a)_{\mathrm{ideal}} = \sqrt{6}$. The $mC4$ lattice parameters and a_{fcc} are related by $a = c = \sqrt{6}a_{\mathrm{fcc}}/2$, $b = a_{\mathrm{fcc}}/\sqrt{2}$, $\beta = 109.5$ with $(c/a)_{\mathrm{ideal}} = \sqrt{6}$ and $(b/a)_{\mathrm{ideal}}$ $= 0.577$ respectively [119].

The heavier lanthanides (Gd-Tm) directly transform into the $mC4$ structure from the d-fcc phase [16, 18, 112, 120–122], excluding Lu which remains in the $hR24$ structure up to at least 200 GPa [123]. While iso-structural across the whole series, the beta angle of the $mC4$ structure varies widely from 104° to 118° [16, 18, 96, 112, 122, 124]. Transformation into the $mC4$ phase is accompanied by a small, abrupt volume decrease in the heavier members [16, 101, 112, 120, 122, 125], but appears to be continuous in both Nd and Sm [116, 117].

Pr and Nd transform into the $oC4$ structure at 20 GPa [126] and 113 GPa [116] respectively, which is iso-structural to uranium at ambient conditions. The $oC4$ structure can be described as an orthorhombic distortion of the hcp structure $a = a_{\mathrm{hcp}}$, $b = \sqrt{3}a_{\mathrm{hcp}}$, $c = c_{\mathrm{hcp}}$ with $(c/a)_{\mathrm{ideal}} = 1.633$ and $(b/a)_{\mathrm{ideal}} = \sqrt{3}$ [119]. In the case of Pr, the structural change is accompanied by a ∼9% drop in volume [106, 108, 126]. In Nd, the transition to the $oC4$ structure is continuous with no abrupt changes in volume or resistivity, and it is stable up to 152 GPa [119]. At 147 GPa, Pr transforms into another orthorhombic structure with the $P2_12_12_1$ space group. This new structure, $oP4$, can be described as a distorted $oC4$ structure [127].

3.3.1 Mechanisms of the "Volume Collapse" transition

The majority of the trivalent lanthanide metals experience a "volume collapse" transition upon compression to a much more complex structure with a reduction in symmetry, the exceptions being La, Ce, Nd, Sm and Pm. In the cases of La and Pm, it is possible they experience a "volume collapse" transition above the limiting pressure range over which they have been studied. Ce undergoes an iso-structural "volume collapse" transition from an fcc phase to different fcc phase, with the fcc/fcc phase boundary ending in a solid-solid critical point. These unique features mean that Ce has been the subject of many studies aiming to understand $4f$ electron behaviour at extreme conditions. The mechanism driving the "volume collapse" transition in Ce is intensely debated, the two most promising theories being the Mott Transition model, where the $4f$ states undergo a local–itinerant transition which allows the $4f$ electrons to participate in inter-atomic bonding [128, 129], and the Kondo Volume Collapse (KVC) model, where

changes in the Kondo temperature affect the $4f$ conduction electron coupling [130–133]. For the rest of the trivalent lanthanide metals, the "volume collapse" transition is the d-fcc $\rightarrow$ post d-fcc phase transition.

The "volume collapse" transitions found in the lanthanide metals cannot be modelled by only one mechanism. As mentioned in the above paragraph, either the Mott Transition or the KVC model is responsible for both the large volume decrease and the drop of magnetic susceptibility found in Ce [134]. In Gd, the appearance of a low symmetry structure is attributed to the onset of $4f$ binding, indicative of the Mott Transition model [128]. However, the Mott Transition model was ruled out by Maddox *et al.* who argued the transition was consistent with the KVC model [135], while Fabbris *et al.* [136] asserted that the $s \rightarrow d$ charge transfer model is the driving force behind Gd's volume collapse. Furthermore, the "volume collapse" transition occurring in Gd's neighbours, Tb and Dy, appear to be caused by the KVC model, due to a large change in the superconducting temperature at the transition pressure [131, 136].

Fabbris *et al.* have pointed out that two transition metals, Y and Sc, exhibit "volume collapse" transitions similar to the lanthanide metals [137, 138]. Neither Y or Sc possess $4f$ electrons, but both are considered to be trivalent. The observation of a "volume collapse" transition in both Y and Sc raises the possibility that it is not related to the $4f$ electrons at all. Fabbris *et al.* suggested that the "volume collapse" transition in both Y and Sc are induced by a $s \rightarrow d$ charge transfer [136], while Samudrala *et al.* postulated that the s and d band electrons in Y are transferred to the $4f$ band at high pressure [137].

3.4 High-Temperature Behaviour

There have also been high-pressure high-temperature experiments on the lanthanide series of metals. La and Ce transform into a fcc structure upon heating at ambient pressure [139], while Sm appears to undergo a phase transformation to the hcp structure upon heating [139]. Upon further heating La, Ce and Sm adopt a bcc structure before melting [10]. All of the other trivalent lanthanide up to Ho transform directly into the bcc phase before reaching the melt line [10, 139]. Er, Tm and Lu do not undergo any transformations upon heating apart from melting at the 0.8 GPa isobar (see [139] and the references therein). All of the lanthanide melt curves (excluding Pm) have a positive Clapeyron slope up to

at least 0.8 GPa, [139, 140], apart from Ce, which starts with a negative slope, reaches a broad minimum at 3.3 GPa and 935 K before the slope becomes positive [141]. There have been high-pressure high-temperature experiments exploring the fcc/d-fcc phase boundary in La, Ce and Pr [17, 142, 143]. In all cases it is possible to heat through the phase boundary from the d-fcc phase to the fcc phase. The previous work on La and Ce will be discussed in more detail in their respective chapters.

The melt curve of Pr, Nd, Sm and Gd were extended to ∼100 GPa and ∼1000 K by Errandonea *et al.* using laser heating techniques [144]. In Pr's case, the gradient of the melt curve increases until a discontinuity is reached, which was interpreted as the fcc/"volume collapsed"/liquid triple point due to the presence of a fcc/d-fcc/"volume collapsed" triple point at 21 GPa and 537 K [145]. Errandonea *et al.* also observed a dip in Pr's melt curve at ∼60 GPa, but questioned the dip's authenticity due to large temperature uncertainties [144]. Errandonea *et al.* also suggested that if the dip in Pr's melt curve above 60 GPa is authentic, then the negative slope indicates a previously undiscovered high-pressure high-temperature phase. A new phase of Pr, labelled Pr-VI, was discovered above 675 K and 19 GPa by Baer *et al.* who were unable to solve the new phase's crystal structure [17]. However, extrapolating Baer *et al.*'s fcc/Pr-IV and Pr-IV/"volume collapsed" phase boundaries, and superimposing them onto Errandonea *et al.*'s phase diagram show that neither the fcc/Pr-IV or the Pr-IV/"volume collapsed" phase boundaries intercept the dip in the melt curve.

Both Nd and Sm display a discontinuity in the melt curve at the fcc/bcc phase boundary similar to Pr. Both Nd and Sm also display a minimum similar to Ce albeit at much higher pressure and temperatures [144]. The melt curve of Gd, by contrast, continuously rises until the fcc/bcc/liquid triple point is reached at ∼21 GPa and ∼2000 K. The melt curve then rapidly increases before levelling off and reaching another discontinuity, attributed originally to a triple point of the melt/d-fc/"volume collapsed" phases [144]. However, a more recent study by Errandonea *et al.* found that the integrated diffraction patterns in the ranges of 39-52 GPa and 1200-2350 K showed several differences when compared to the d-fcc($hR24$) pattern [18]. These changes were reversible upon cooling, and temperature cycling the sample didn't cause an increase in the intensity of the new peaks. Errandonea *et al.* attribute the new diffraction peaks to be evidence of a transformation to a new phase, though Errandonea *et al.* do not present a solution for the crystal structure of the new phase [18].

3.5 Conclusions

This chapter provided an overview of the known behaviour of the trivalent lanthanide series of metals under pressure. The trivalent lanthanide metals exhibit a common transformation sequence upon compression: hcp → Sm-type → dhcp → fcc → d-fcc → "volume collapsed" phase. It is thought that the high-pressure behaviour of the lanthanides is well known, particularly the lighter members Ce and Pr. However, as has been shown by Evans *et al.* [106], great care has to be taken to distinguish between the different structures suggested for the d-fcc phase. Structural assignment of the high-pressure phases of the heavier lanthanide metals rely on analogy with the lighter members. The high-pressure high-temperature behaviour of the lanthanide metals is less well known, with two lanthanide metals exhibiting unknown structures at elevated pressure and temperature. Furthermore, there are also very few systematic studies of the various phase boundaries at temperature.

Despite occupying unique positions in the lanthanide series (La not having any $4f$ electrons and Gd possessing a half filled $4f$ shell at ambient conditions), La and Gd have not received as much attention as Ce. These elements, and their outstanding issues will be discussed in more detail in their respective chapters. Ce has received the most attention out of the various lanthanide metals due to its single $4f$ electron. Despite Ce's classification as a trivalent lanthanide, Ce's high-pressure behaviour is strikingly different compared to the rest of the series, and will be discussed in much more depth in the next chapter.

Chapter 4

Cerium

4.1 Introduction

Ce only has one electron in the $4f$ electron shell at ambient pressure and temperature, and has the electronic configuration [Xe]$6s^2 5d 4f$ [15]. Due to the $4f$ shell's closeness to the Fermi level [146], the single $4f$ electron is cited as the driving force behind Ce's behaviour. Dispite being considered trivalent, Ce's high-pressure behaviour is very different compared to other trivalent lanthanides. Ce crystallises in either the fcc structure (labelled γ in the literature, $cF4$ in Pearson notation and fcc(γ) in this thesis), or the dhcp structure (labelled β in the literature and $hP4$ in Pearson notation) at ambient conditions [147]. The dhcp phase only appears to be stable after the sample has been cooled in liquid nitrogen then annealled at 348 K [140, 148]. Wittag reported a large resistance drop upon compression at 0.7 GPa and room temperature, signalling the transformation into a new phase [149], which was determined by Lawson *et al.* to have a different fcc structure [147]. The new fcc structure was labelled α (referred to fcc(α) in this thesis), and the transition was accompanied by a large volume decrease, similar to "volume collapse" transitions in other trivalent lanthanides. Ce differs from the rest of the trivalent lanthanides since a high symmetry structure is adopted after "volume collapse" transition, rather than the low symmetry structures the rest of the series exhibits.

The fcc(γ) $\rightarrow$ fcc(α) transition abruptly ends at a solid-solid critical point [139], currently estimated to be at 1.8 GPa and 485 K [143]. The fcc $\rightarrow$ fcc iso-structural

transition, and the solid-solid critical point, are unique to Ce within the elements and each has been the subject of many studies (see [77, 130, 150–153] and the references contained within).

Ce undergoes another transformation at ∼5 GPa and room temperature to a d-fcc phase. The first x-ray diffraction experiments reported that Ce appeared to transform into one of two structures. The first being an orthorhombic structure with 4 atoms per unit cell (labelled α' in the literature, or $oC4$ in Pearson notation), which is iso-structural with the α-U structure adopted by uranium at ambient conditions [154, 155]. The second structure observed is monoclinic and C centered with 4 atoms per unit cell (labelled α'', or $mC4$) [118, 156]. While the $oC4$ structure is not a distorted verison of fcc, the region of phase space where $oC4$ is stable is labelled the d-fcc phase in this thesis to be consistent with the other trivalent lanthanide metals. Other solutions were proposed for the d-fcc phase. McWhan *et al.* suggested that Ce assumed the hcp structure [157], while Schaufelberger assigned a mixed fcc/hcp structure [158]. Both studies had significant misfits between the calculated and observed data. Ellinger *et al.* subsequently interpreted the data collected by McWhan *et al.* to be from an $oC4$ structure [154], and Zachariasen indexed Schaufelberger's data to the $mC4$ structure [159]. More recent studies have observed both the $oC4$ and $mC4$ structures [160, 161]. Zachariasen *et al.* reported that slowly pressure cycling a $oC4/mC4$ mixed-phase sample transforms it into a pure $oC4$ phase, indicating that slower rates of compression favour the $oC4$ structure [162]. Upon heating a $mC4$ sample, it transforms into pure $oC4$ and remains pure upon cooling [159]. Zachariasen *et al.* also noted that both the fcc(α) $\rightarrow$ d-fcc($oC4$) and d-fcc($mC4$) $\rightarrow$ d-fcc($oC4$) transformations require substantial structural rearrangement, while the fcc(α) $\rightarrow$ d-fcc($mC4$) transformation can be achieved through a small distortion of the fcc atomic coordinates [163]. It was determined by McMahon *et al.* that the structure adopted depends on the prior mechanical treatment of the sample [164]: samples cut from an ingot transform into the $oC4$ structure [159–161], while cold-worked samples or small shavings, transform to the $mC4$ structure [118, 156].

Upon further compression, Ce transforms into a body centered tetragonal (bct) structure (labelled ϵ in the literature or $tI2$ in Pearson notation) at ∼12 GPa [156]. The bct structure remains stable up to 208 GPa, the highest pressure to which Ce has been studied [165].

There have been several high-pressure high-temperature experiments exploring

the d-fcc stability region. The earliest studies undertaken by King *et al.* and Endo *et al.* utilized resistivity techniques, and focused on the fcc(α) $\rightarrow$ d-fcc and the d-fcc $\rightarrow$ bct transitions respectively [166, 167]. Both phase boundaries were reported to have negative gradients in these studies. Antonova *et al.* thoroughly examined the fcc(α) $\rightarrow$ d-fcc transition using resistivity and differential thermal analysis (DTA) techniques, and combined their isobaric and isothermal data with the data collected by King *et al.* and Endo *et al.* They proposed the d-fcc phase boundary to be curved at high temperature, with large hysteresis between the fcc $\rightarrow$ d-fcc transition pressure on compression and decompression (see Figure 4.1). While Antonova *et al.* did not directly observe the fcc(α) $\rightarrow$ bct transition at pressure, they extrapolated the data by Endo *et al.* and estimated the fcc(α)/d-fcc($oC4$)/bct triple point to be at 8.3 GPa and 625 K [168].

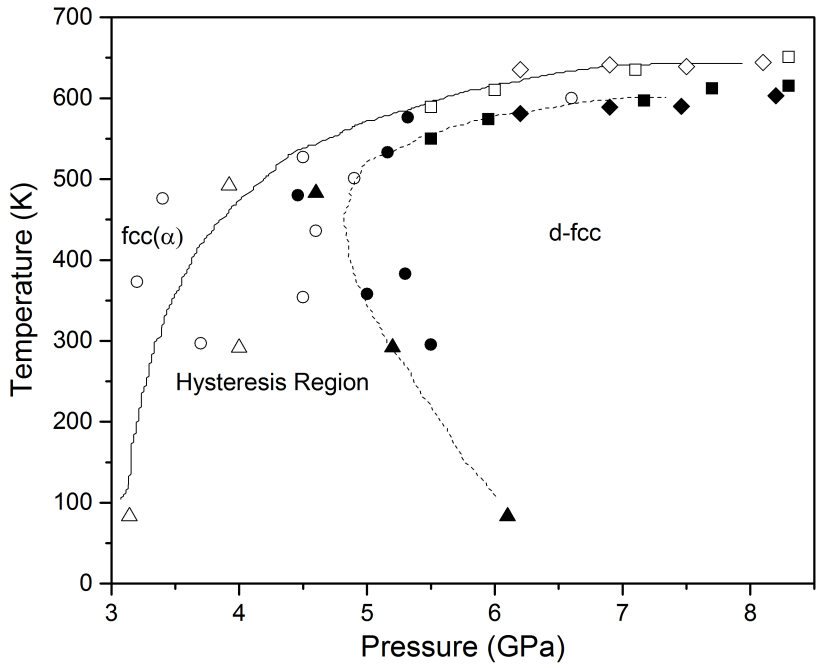

Figure 4.1 *P-T diagram highlighting the large hysteresis region of the fcc(α) $\rightarrow$ d-fcc transition. Black and hollow circles mark resistivity changes on pressure increase and decrease respectively, from Antonova et al. [168]. Black and hollow triangles mark resistivity changes on pressure increase and decrease respectively, from King et al. The black and hollow diamonds mark anomalies in DTA measurements at isobaric cooling and heating respectively from Antonova et al. [168]. Finally, the black and hollow squares mark changes in resistivity at isobaric conditions, but do not specify if the data were collected upon heating or cooling from Antonova et al. [168]. Image adapted from Antonova et al. [168].*

Energy dispersive x-ray diffraction data collected by Zhao *et al.* suggested that

the d-fcc($mC4$) structure transforms into the d-fcc($oC4$) structure above 400 K, which remained stable when cooled back to room temperature [161]. Zhao *et al.*'s diffraction data were generally consistent with the phase diagram suggested by Antonova *et al.*, but could not determine the location or nature of the fcc(α) $\rightarrow$ bct phase boundary [161]. Tsiok *et al.* presented a comprehensive resistivity study at high pressure and temperature to 15 GPa and 710 K [169]. They were able to determine the location and gradient of the fcc(α)/bct phase boundary upon isobaric heating, but did not observe the transition back to bct upon cooling. This led Tsiok *et al.* to suggest that the bct phase of Ce is a meta-stable phase above 11 GPa. Finally, Tsiok *et al.* also noted that the structure adopted by Ce was dependent on the path taken to get to that point in P-T space [169]. Schiwek *et al.* reported a very different fcc(α) $\rightarrow$ bct phase boundary with a much steeper, positive slope. Extrapolating their data, the fcc(α)/bct phase boundary intercepted the d-fcc stability region at its apex, and placed the fcc(α)/d-fcc/bct triple point at 6.9 GPa and 600 K (see Figure 4.2). Additionally Schiwek *et al.* suggested that the fcc(α) $\rightarrow$ bct transition is a second order transition [143].

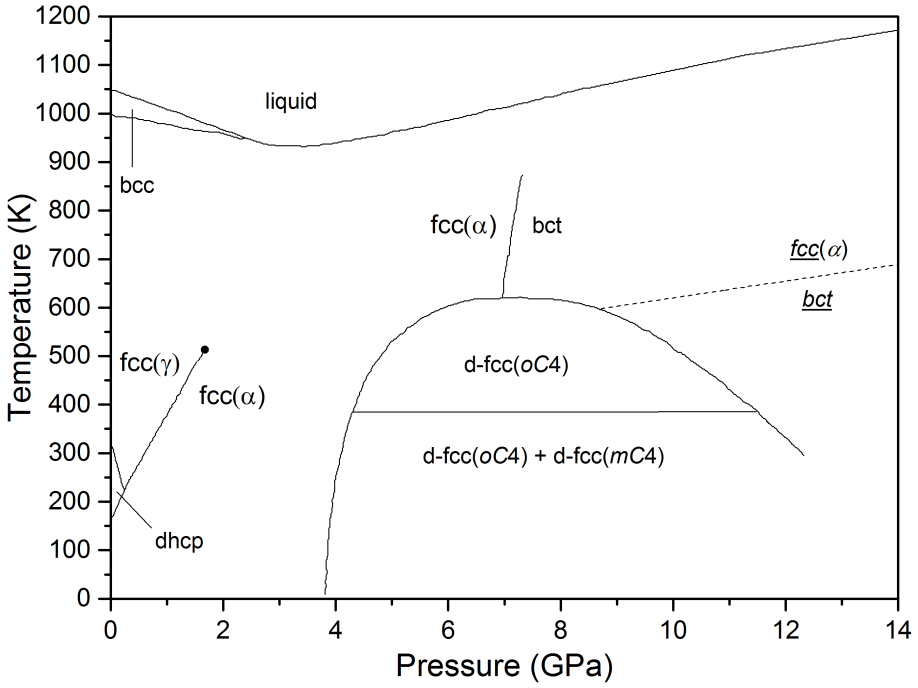

Figure 4.2 *The currently accepted phase diagram of Ce, recreated from Schiwek et al. [143] using solid lines. The dashed line is the fcc(α) $\rightarrow$ bct phase line from Tsiok et al. [169].*

4.1.1 Outstanding Issues

While there have been a considerable number of studies on the behaviour of Ce at pressure and temperature, there remain a number of outstanding issues. The majority of experiments exploring Ce's various phase boundaries used DTA and resistivity techniques, which do not provide any direct structural information. Since the structure adopted by Ce when transforming into the d-fcc phase is dependent on the sample's history, it is not clear if the fcc(α) $\rightarrow$ d-fcc($oC4$) or fcc(α) $\rightarrow$ d-fcc($mC4$) phase boundary was being measured in early experiments [166–168]. Furthermore, there is no evidence to suggest that the fcc(α) $\rightarrow$ d-fcc($oC4$) and the fcc(α) $\rightarrow$ d-fcc($mC4$) phase boundaries have the same shape.

The lack of any substantial x-ray experiments on the fcc(α) $\rightarrow$ bct phase boundary at high temperature make it difficult to determine its shape and nature, with the phase boundary being inferred by combining the diffraction data of Zhao *et al.* [161] and the resistivity data of Endo *et al.* [167]. The only x-ray diffraction study on the direct fcc(α) $\rightarrow$ bct phase transition, above the stability field of d-fcc phase, was performed by Schiwek *et al.* [143], who only reported two data points, which is insufficient to determine the shape of the phase boundary beyond a straight line.

These uncertainties are further emphasized by unpublished data collected by McMahon *et al.* [170], prior to the author of this thesis involvement, on isothermal compression at $\sim$550 K, where an fcc(α) $\rightarrow$ bct $\rightarrow$ d-fcc($oC4$) $\rightarrow$ bct transition sequence was observed. This phase transition sequence contradicts both the currently accepted phase diagram by Schiwek *et al.* and the proposed phase diagram by Tsiok *et al.* Furthermore, this transition implies that the fcc(α) $\rightarrow$ bct does not intercept the d-fcc stability region at the region's maxima. Addressing these issues were the primary drive behind studying Ce, and the results of multiple experiments are presented below.

4.2 Experimental Details

All of the Ce samples used in this thesis were cut from a high purity (99.99+%) Ce ingot, provided by U. Schwarz of the MPI für Chemische Physik fester Stoffe. Since cut samples were utilized in all cells, only the $oC4$ structure was observed above 5 GPa, consistent with the results from McMahon *et al.* [164]. For room

temperature experiments, the samples were loaded into MB DACs equipped with tungsten gaskets, and loaded with a small piece of 1 μm thick Ta foil as a pressure calibrant. The cells were loaded in an oxygen free, water free environment (<1 ppm O_2 and <1 ppm H_2O). No pressure transmitting medium was included to prevent sample contamination, and to minimise any chemical reactions occurring within the sample chamber during sample loading. The room temperature data were collected at the high-pressure beamline I15 at the DLS using a monochromated x-ray beam with incident wavelength ∼0.311 Å, collimated to 30 μm in diameter, with a MAR345 detector placed ∼350 mm from the sample. Data were also collected at the materials science and powder diffraction beamline BL04 at ALBA, using an incident x-ray beam of wavelength ∼0.424 Å collimated to 20 μm in diameter, with a SX165 CCD camera placed ∼200 mm from the sample.

The samples studied in the high-pressure high-temperature experiments were prepared as described in the previous paragraph. Samples were loaded into LLNL DACs equipped with rhenium gaskets, which were then placed into the vacuum vessel described previously in Section 2.5. Ta was the most common pressure marker used, however some cells utilized a Cu or NaCl marker instead. The equations of state used to determine pressure are referenced in Section 2.2.2. Multiple high-pressure high-temperature experiments were completed at the DLS with different experimental setups. Diffraction data were collected at beamline I15 using an incident x-ray wavelength of ∼0.311 Å, with a Perkin Elmer detector placed ∼430 mm from the sample. Two other experiments used a MAR345 detector placed at ∼380 mm and ∼450 mm from the sample with x-ray incident wavelength 0.4246 Å and 0.4133 Å respectively. Data has also been collected at beamline BL04 at ALBA, using an x-ray wavelength of 0.425 Å with the SX165 CCD camera placed ∼180 mm and ∼190 mm from the sample. Finally, a single data point at 12.1 GPa and 448 K was collected at station ID09a at the ESRF, using an x-ray wavelength of 0.411 Å with a MAR555 detector placed ∼400 mm from the sample.

In all experiments, the diffraction images were integrated azimuthally using the Fit2D [171] software and analysed using Le Bail fitting and Rietveld refinement techniques utilizing the Jana software [172]. Since the samples were not loaded with any pressure transmitting medium, the samples may have experienced non-hydrostatic pressure. The methods by Singh *et al.* were used to quantify any non-hydrostatic effects [173]. So called gamma plots were made for various diffraction

patterns at different pressures and temperatures. In a gamma plot, the lattice parameters as determined by single (hkl) reflections from a cubic cell were plotted against 3(1-3cos$^2\,\psi$)Γ, where $\Gamma = [(hk)^2 + (kl)^2 + (hl)^2]/[\mathrm{h}^2 + \mathrm{k}^2 + \mathrm{l}^2]^2$ and ψ is the azimuthal angle between the DAC loading axis and the diffraction plane normal [174]. Following the analysis by Singh *et al.* for a sample under non-hydrostatic conditions the gamma plot will deviate from a straight line [173]. Despite not using a pressure transmitting medium, no measurable non-hydrostatic effects were observed.

4.3 Experimental Results

As has been described in Section 4.2 the DACs used in these experiments used different markers. In the following sections a DAC loaded with a Ta marker will be referred to as a Ta DAC, a DAC loaded with a Cu marker will be referred to as a Cu DAC and a DAC loaded with an NaCl marker will be referred to as an NaCl DAC.

4.3.1 Room Temperature Compression

In most cases, upon closing the DAC the sample was compressed directly into the fcc(α) phase above 2 GPa. However, there were some samples which were in the dhcp phase (referred to as β-Ce in the literature), or in the fcc(γ) phase after the DAC was closed. A pure dhcp phase was never observed, and always co-existed as a mixed phase with fcc(γ). The transformation to a pure fcc(γ) phase was completed by 0.97 GPa. The fcc(γ) $\rightarrow$ fcc(α) transition started at 1.1 GPa and by 1.8 GPa no trace of fcc(γ) remained. Three data sets were collected upon compression at room temperature up to 15 GPa. Two of these used Ta as the pressure marker, while the other utilized Cu. As the pressure was increased, multiple Bragg spots appeared in the raw 2-D image indicating the growth of a single crystal (see Figure 4.3), which is characteristic of the fcc(α) $\rightarrow$ d-fcc($oC4$) transition [160, 164]. The cells with the Ta marker indicated the transition had occurred at 4.0 GPa, while the Cu DAC showed that the transformation had occurred between 4.9 and 5.5 GPa. The fcc(α) $\rightarrow$ d-fcc($oC4$) transition pressure obtained from the Cu marker is in good agreement with previous works [160, 161, 163].

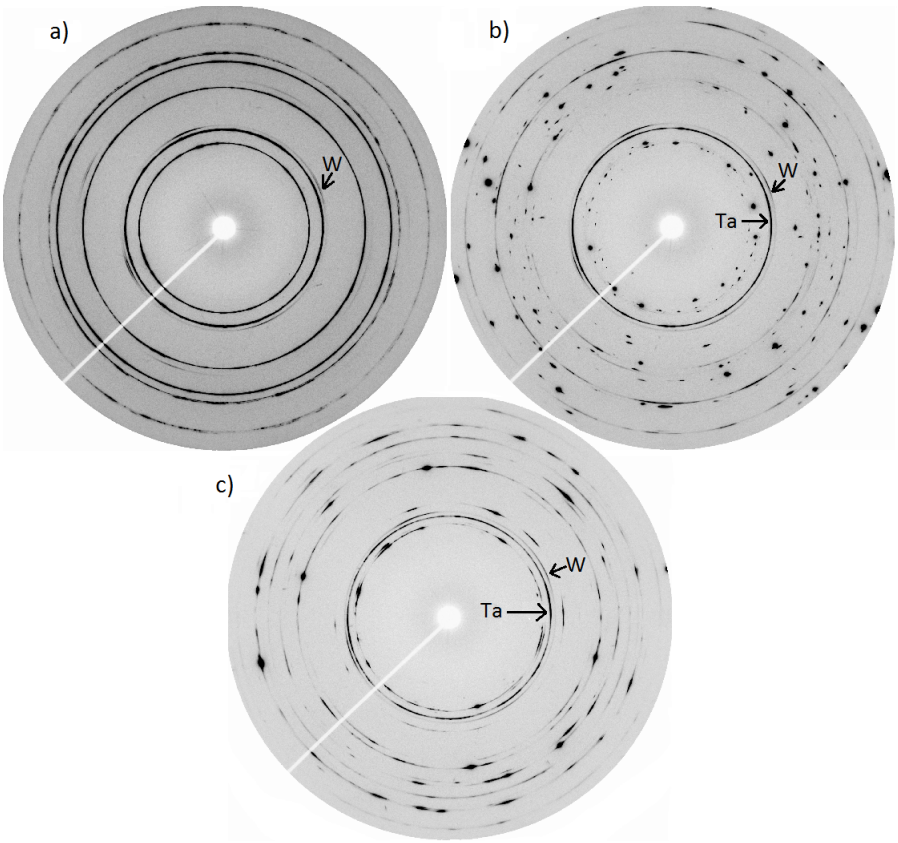

Figure 4.3 *Raw diffraction images from the various structures found in Ce at 296 K: a) the fcc(α) phase at 3.74 GPa b) the d-fcc(oC4) phase at 5.78 GPa and c) the bct phase at 22.5 GPa. The textured Debye-Scherrer rings in image b) are from either Ta or the W gasket. The (110) rings of Ta and W are labelled in each pattern, but in the case of the fcc(α) image the Ta peaks almost perfectly overlap with the fcc(α) peaks. It is clear when Ce undergoes a phase transformation, since the onset of the transformation to the d-fcc(oC4) structure is accompanied by the disappearance of fcc(α)'s smooth powder rings and the appearance of intense spots in the raw image. The appearance of the (110) reflection indicates the transformation to the bct phase, which is highlighted in Figure 4.4.*

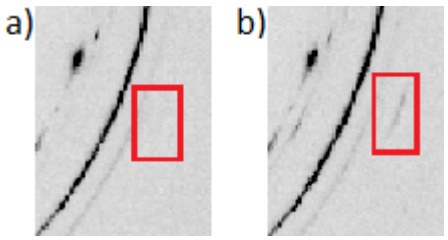

Figure 4.4 *a) Raw diffraction image segment of the d-fcc(oC4) structure at 10.4 GPa b) Raw image segment of the bct structure at 12.6 GPa. The red box highlights the emergence of the (110) reflection, signalling the transformation to the bct structure.*

As the pressure was increased further the d-fcc($oC4$) samples gradually became less single-crystal like and more powder like. The transition into the bct structure was identified by the appearance of the bct (110) peak, and the diffraction pattern from the bct phase was characterized by textured Deybe-Scherrer rings, with non-uniform intensities around the ring (see Figure 4.4). One of the Ta DACs and the Cu DAC place the d-fcc($oC4$) $\rightarrow$ bct transition at 12.6 and 12.8 GPa respectively, in good agreement with previous works [109, 156], while the 2$^{\text{nd}}$ Ta DAC showed the transformation occurring at 15.9 GPa.

The different fcc(α) $\rightarrow$ d-fcc($oC4$) transition pressures are not unique to the room temperature data, and will be discussed in more detail in the next subsection. The different pressures measured for the d-fcc($oC4$) $\rightarrow$ bct transition are not due to the different pressure markers used, since the issue arises between two DACs using Ta marker. In both cases, the sample was cut from the same ingot, and prepared in the same way, so sample differences can also be ruled out. In the case of the 2$^{\text{nd}}$ Ta DAC, the backing seats were designed for standard cut diamonds and had a opening slit, while the other two DACs used backing discs with a full conical opening made to fit Boehler-Almax diamonds, see Figure 4.5 for a comparison.

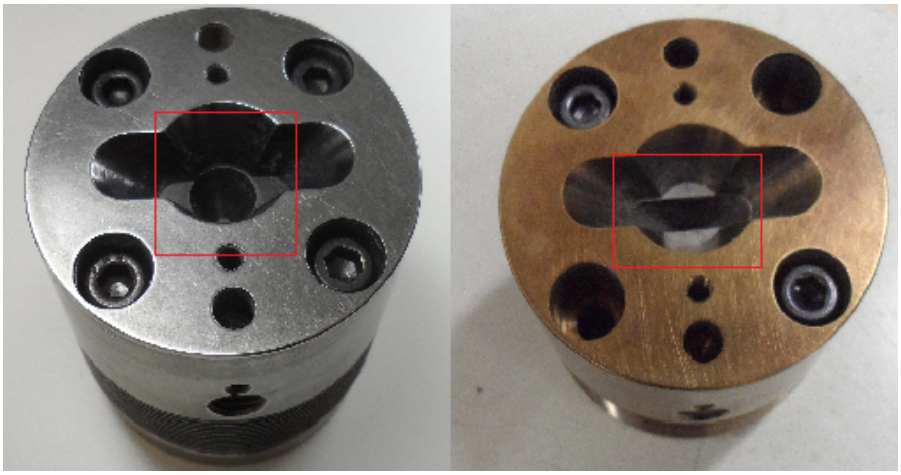

Figure 4.5 *Left: Image of a LLNL cell with a Boehler-Almax backing disc. Right: Image of a LLNL cell with a slit backing disc. The red square highlights the different backing discs utilized in experiments. The DAC on the left used backing discs with a full conical opening compared to the DAC on the right used a backing disc with a slit.*

As can be seen in Figure 4.5, the opening angle of the 2$^{\text{nd}}$ Ta cell is greatly reduced in comparison to the other two cells with BA backing discs. Consequently, the area of the Deybe-Scherrer pattern that can be observed is reduced, as shown in

Figure 4.6. As has been described previously in this chapter, the bct rings are very textured, as shown in Figure 4.4. This textured nature, combined with the unused regions of the detector, raises the possibility that the bct rings first appear in the area of the detector that was being blocked by the slit backing disc. The bct (110) reflection is only observed after a more uniform and intense Debye Scherrer ring is formed upon further compression. As such the 15.9 GPa transition point was not used for analysis, placing the room temperature d-fcc($oC4$) $\rightarrow$ bct transition at 12.7 GPa. The high-pressure high-temperature data that used Ta as a marker had already been collected when this issue had been identified. However, there were no obvious inconsistencies in the rest of the data which had Ta as a marker, suggesting this problem was unique to that particular DAC. The high-pressure high-temperature data that were collected from a Cu or NaCl DAC used full conical backing discs, which resolved this issue.

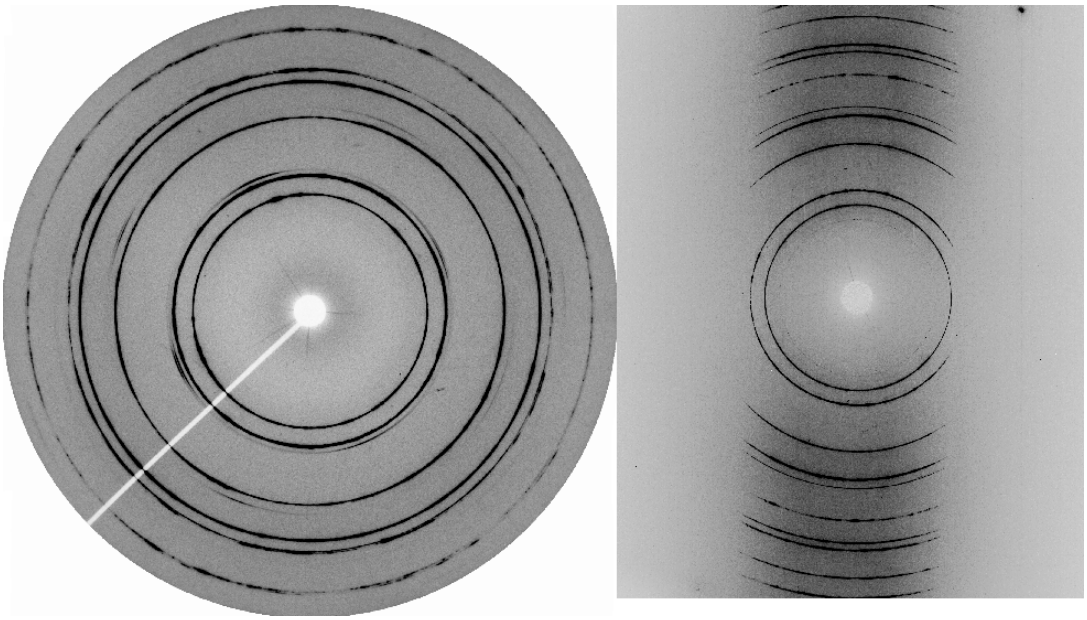

Figure 4.6 *Left: Raw diffraction image collected from an fcc(α) Ce sample contained within a LLNL DAC with a Boehler-Almax backing disc. Right: Raw diffraction image collected from an fcc(α) Ce sample contained in a LLNL DAC with a slit backing disc. The whole detector is able to collect data in the left hand picture, whereas only a portion of the detector is able to collect data in the right hand picture.*

4.3.2 The High-Pressure High-Temperature phase diagram

In this work, the phase boundaries between the fcc(α), d-fcc($oC4$) and bct phases up to ∼775 K and 20 GPa have been studied. Initially, the samples were compressed up to ∼3 GPa into the fcc(α) phase, and then heated to the desired temperature using either the copper heating block, or the vacuum vessel described in Section 2.5. In general, the samples were then iso-thermally compressed until single phase bct diffraction patterns were obtained. Attempts were made to collect data on the fcc(α) → d-fcc($oC4$) and d-fcc($oC4$) → bct phase boundaries on decompression to measure hysteresis effects. However, the LLNL DACs have no mechanism to force the cell apart and guarantee decompression. In addition, the LLNL DACs can become stuck due to the thermal expansion of the metal body. As a result, it was extremely difficult to measure the fcc(α) → d-fcc($oC4$) and the d-fcc($oC4$) → bct phase boundaries on decompression.

Similar to the room temperature compression experiments, the transformation to the d-fcc($oC4$) phase was marked by the appearance of multiple Bragg spots in the 2-D image. The d-fcc($oC4$) stability region appears to be dome shaped, the fcc(α) → d-fcc($oC4$) boundary has a very steep, positive gradient, until 4.2 GPa and 450 K, where the boundary becomes much more gradual until the fcc(α)/d-fcc($oC4$)/bct triple point is reached. The d-fcc($oC4$)/bct boundary remains gradual until 12 GPa, where the d-fcc($oC4$) → bct boundary becomes very steep with a slightly negative gradient, as shown in Figure 4.7. The transition point collected at ∼9 GPa and ∼580 K was collected as the sample was being heated. The data point at 10.4 GPa and 574 K was collected as pressure and temperature slowly drifted upwards after decompressing back through the fcc(α) → d-fcc($oC4$) transition at 11.6 GPa and 524 K. The data collected on the fcc(α) → bct phase boundary were collected from a single cell going back and forth across the phase boundary, up to 773 K, with no observable hysteresis. Above 773 K the temperature measurement started to fluctuate rapidly, making an accurate determination of the sample's temperature almost impossible. Furthermore, above ∼670 K contaminant peaks were observed, growing in intensity as temperature increased. After the experiment, the diamond anvil culets were discoloured, indicating that the Ce sample had reacted with the diamond to form a carbide. The results showed that the phase line had a negative gradient, contradicting previous results (shown in Figure 4.2), and emerges from the fcc(α)/d-fcc($oC4$)/bct triple point at ∼7.7 GPa and ∼590 K. The phase diagram is presented in Figure 4.7.

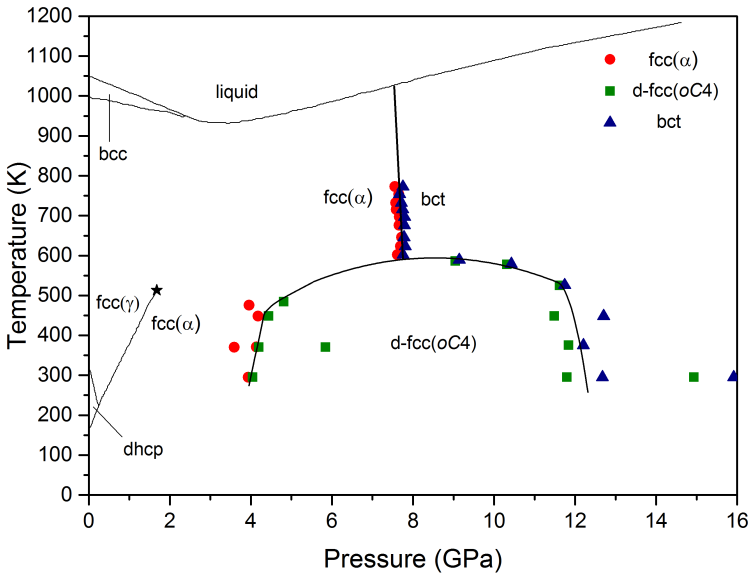

Figure 4.7 *Proposed phase diagram of Ce from Ta DACs. Circles show where fcc(α) was found, squares show where d-fcc(oC4) was found, triangles show where bct was found. The star is the fcc(γ)/fcc(α) critical point from Schiwek et al. The two data points collected above 14 GPa and 300 K were collected from the Ta DAC with the slit seat, and was not included in analysis. The solid lines are the suggested phase boundaries.*

All of the data presented in Figure 4.7 used Ta as the pressure marker. Ta is a very appealing pressure marker for these experiments. The thermal expansion co-efficient of Ta is very small, such that within the pressure range studied the pressure correction needed to account for the Ta's thermal expansion is small, and largely independent of pressure [175]. Ta crystallises in the bcc structure, which reduced the number of diffraction peaks that can potentially overlap with the Ce peaks. However, Ta has two major problems: firstly, Ta's incompressibility makes it unsuitable for determining small pressure shifts, with small changes in Ta's lattice parameter corresponding to large pressure changes. Secondly, the Ta diffraction pattern overlaps almost perfectly with fcc(α)'s diffraction pattern just before the transformation to the d-fcc($oC4$) structure and the bct structure (see Figure 4.8) at all temperatures.

Due to the overlap of Ce and Ta at both the fcc(α) $\rightarrow$ d-fcc($oC4$) and the fcc(α) $\rightarrow$ bct transitions, and reliance on a single Ta peak for pressure determination, there were concerns that the pressure was being determined incorrectly. In order to confirm the disparate fcc(α) $\rightarrow$ bct phase boundary compared to the boundary by Schiwek *et al.* [143], some data points were re-collected using different markers,

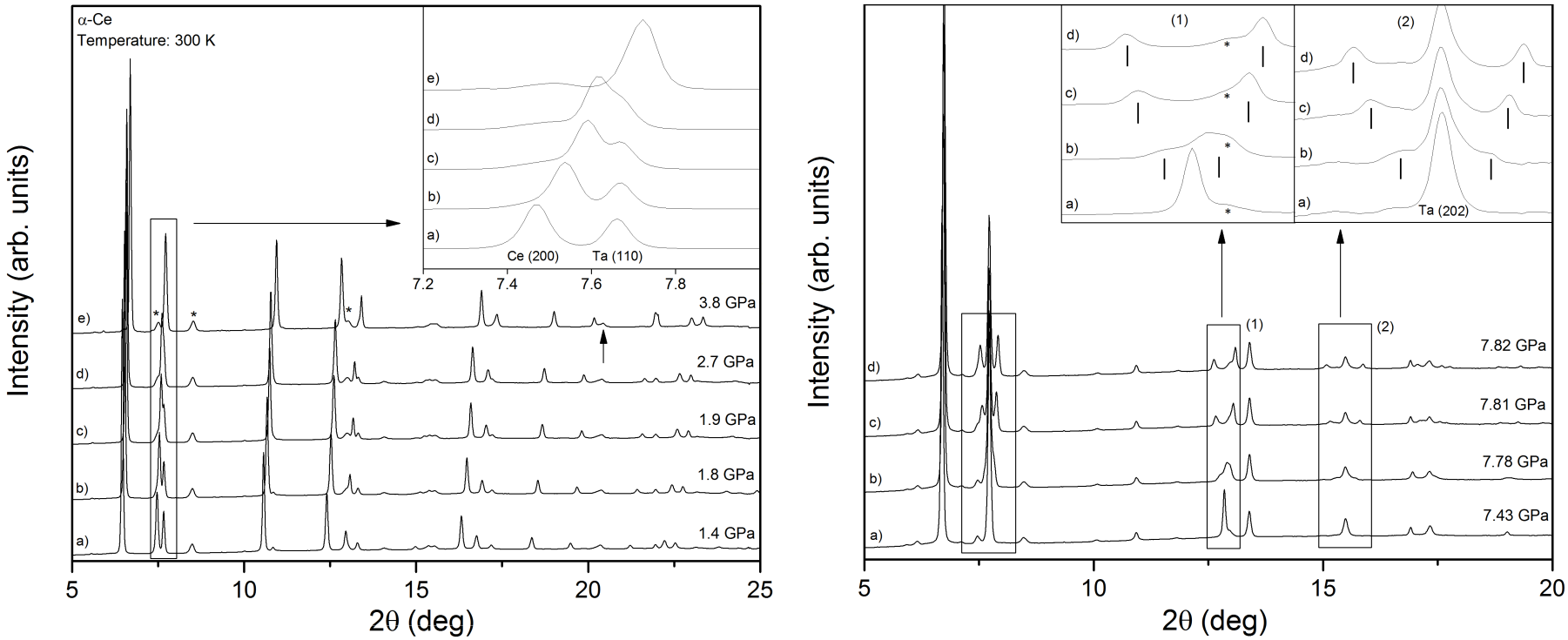

Figure 4.8 *Left: Waterfall plot of fcc(α) Ce on compression at room temperature to just before the fcc(α) → d-fcc(oC4) transition. The integrated diffraction pattern also contains peaks from the Ta marker and Re gasket. The insert highlights how the fcc(α) (200) reflection starts to overlap with the Ta (110) reflection as pressure increases. The arrow in the main profile identifies the Ta (213) reflection which is the first Ta peak that does not overlap with either the fcc(α) or the Re gasket. Consequently, the (213) reflection was used for pressure determination. The asterisks in the main profile show the positions of the first 3 non-overlapped Re peaks. Right: Waterfall plot showing fcc(α) Ce transforming into the bct structure at 623 K, with the boxes from left to right drawing attention to the fcc(α) (200), (311) and (400) singlets respectively. The left insert highlights the fcc(α) (311) singlet splitting into the bct (103)/(211) doublet, with a Re peak being highlighted by the asterisk. The right insert shows the fcc(α) (400) reflection splitting into the bct (004)/(220) doublet. The fcc(α) (200) and Ta (110) peaks completely overlap just before the transition, resulting in the splitting of the fcc(α) (200) reflection being almost completely obscured by the Ta (110) reflection.*

Cu and NaCl. The NaCl marker also served as a barrier between the culets and the Ce sample, and possibly reduced non-hydrostatic effects by acting as a pressure medium. The combined results are shown in Figure 4.9.

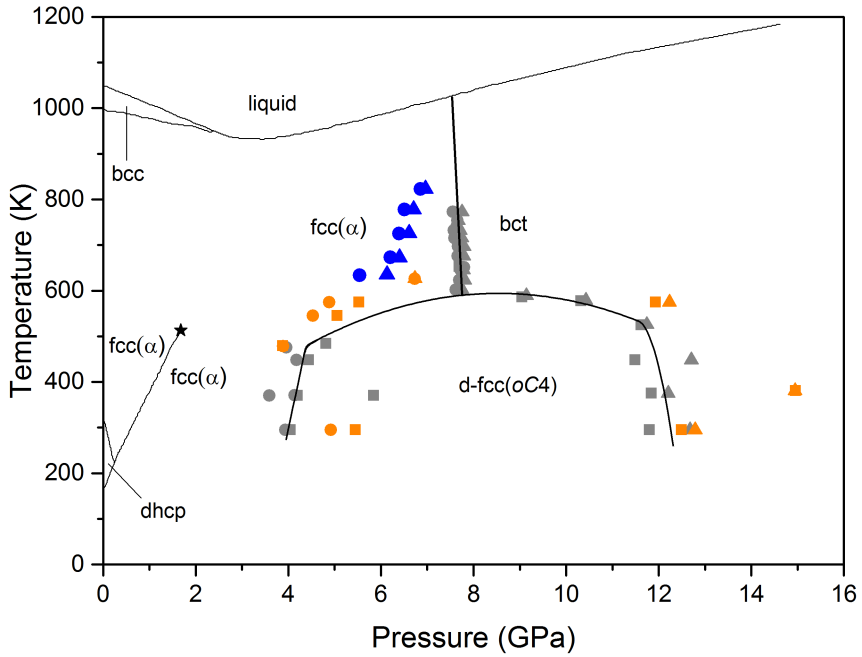

Figure 4.9 *High-pressure high-temperature phase diagram of Ce to 16 GPa and 1200 K. Circles pin-point where fcc(α) was found, squares mark the presence of d-fcc($oC4$) while triangles identify the bct phase. Grey points were taken with Ta pressure maker, orange used copper, and blue utilized NaCl. The solid black lines are suggested phase boundaries from the Ta data, while the dashed lines map out the d-fcc($oC4$) stability region utilizing all of the data collected. The rest of the phase boundaries and the black star which shows the location of the fcc(γ)/fcc(α) critical point are from Schiwek et al. [143].*

The transition pressures from the Cu DAC's are particularly concerning, since the scatter of transition points do not reveal any tends regarding the d-fcc($oC4$) region of stability. Furthermore, most of the transition pressures and temperatures do not appear to be reproducible.

4.4 Discussion

As can be seen in Figure 4.9, the data points collected using the three different pressure markers give very different pressure readings for the fcc(α) $\rightarrow$ d-fcc($oC4$) and d-fcc($oC4$) $\rightarrow$ bct phase transitions at the same temperature. Only the

d-fcc($oC4$) $\rightarrow$ bct transition pressure at room temperature was insensitive to the pressure marker. At $\sim$500 K, the fcc(α) $\rightarrow$ d-fcc($oC4$) transition pressure as determined by Ta is higher compared to the same transition pressure as determined by Cu, while at room temperature, the reverse is true. As a result, the transition pressures as determined by one marker cannot simply all be shifted by the same pressure to correspond with the transition pressures as determined by the other markers.

This led to the question of whether the transitions are actually occurring at different pressures with different markers, or if there was a problem with the pressure marker's EoS. Ideally two diffraction patterns, one from a Ta DAC and one from a Cu or NaCl DAC, with the same sample volume and temperature were identified, insuring that the two samples were at the same pressure (see Figure 4.10). Any different in pressure according to the two different markers was then applied to the transition pressure at the same temperature. If the transition pressures between different DAC's matched, then the marker's EoS was likely the issue. If the transitions pressures did not coincide, then the sample was undergoing the transition at very different pressures.

However, in general, such identical patterns were rare. It was necessary to make a "pressure calculator" for the various phases of Ce, by fitting a quadratic to the P-V data, which returned a pressure value if the Ce volume is known. Using this calculator, the calculated pressure P_{calc} for both patterns was determined (see Table 4.1), giving a value for the pressure difference between the 2 profiles ΔP_{calc}. The pressure difference as determined by the pressure markers, $\Delta P_{\mathrm{marker}}$, was then calculated, and the pressure shift, $P_{\mathrm{shift}} = \Delta P_{\mathrm{marker}} + \Delta P_{\mathrm{calc}}$, was determined. The pressure shift was then added to one of the transition pressures, typically from the Cu DACs, to compare the two transition pressures. If this shifted transition pressure from the Cu DAC was consistent with the transition pressure from the Ta DAC (ie, the transition was occurring at the same sample volume) there was likely a problem with the marker's EoS.

This comparison method has some assumptions. In order to determine the magnitude of the pressure shift at a particular temperature, it is necessary to have an isothermal compression of Ce and the marker, at said temperature. The pressure of the Ce could then be calculated from the Ce volume directly, calibrated against the marker. In general, these pressure calculators were made using data from DAC's loaded with Ta, due to the larger number of diffraction patterns collected from Ta DACs compared to Cu and NaCl DACs. But a

corresponding pressure calculators were made using the P-V data from Cu or NaCl and DACs where possible, and both calculators returned consistent pressures. Any pressure variations due to differences in temperature between the two samples were calculated using the thermal EoS's mentioned in Section 2.2.2. It is important to note that this method only determines if the sample volume, and thus the pressure, is the same regardless of calibrant just before a transition.

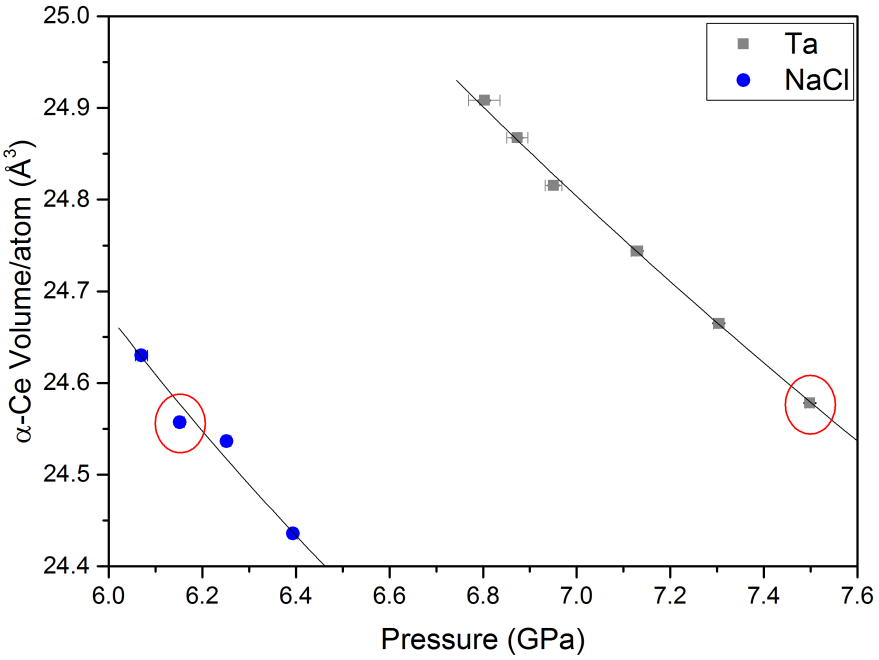

Figure 4.10 *Isothermal P-V plot at 725 K of fcc(α) Ce just before the phase transition to the bct phase. The grey squares are data points whose pressures are determined from a Ta marker; the blue circles have had the pressures determined using NaCl. The data points within the red circle are two data points collect from different DACs with the smallest fcc(α) volume difference. Subsequently, the circled points were used to determine P_{shift}. A 2^{nd} order polynomial were fitted to both data sets to create the pressure calculators to determine P_{calc}.*

In general, at the same Ce sample volume, the Ta pressure marker indicates a higher pressure compared to the Cu marker. The only exception was the room temperature fcc(α) $\rightarrow$ d-fcc($oC4$) transition where the reverse was true. Four P_{shift} were calculated to compare the mismatched data collected from Ta and Cu DACs at ~5 GPa and 300 K, ~4 GPa and ~474 K, ~10 - 12 GPa and ~577 K and ~12 - 15 GPa and ~377 K. These P_{shift} were -1.15 GPa, 0.38 GPa, 1.72 GPa and 0.80 GPa respectively. The pressure shifts were applied to the

T (K)	Marker	V/atom	P_{calc}(Ta)	P_{marker}	P_{shift}
718.6(1)	Ta	24.5781(5)	7.4766(13)	7.498(9)	
731.8(1)	NaCl	24.557(3)	7.529(7)	6.152(9)	
	Ta-NaCl		0.053(7)	1.346(13)	1.294(15)

Table 4.1 *Table showing the processes needed to determine the shift needed to make the data from the NaCl consistent with the Ta cell. P_{calc}(Ta) is the pressure of the sample according to the sample volume and the pressure calculator as determined by Ta. P_{marker} is the pressure according to the marker. P_{shift} is the number added to the pressure as determined by the NaCl marker so the data from the NaCl DAC is consistent with the Ta DAC data. In this case, the shift in pressure due to different temperatures was 0.03 GPa. Since this shift due to different temperatures is an order of magnitude larger than P_{marker}'s error, it was used as the error in further analysis.*

data from the Cu DAC's, since there are fewer transition points compared to the data collected from the Ta DACs, and the Cu DAC data set has much more scatter compared to the Ta DAC data set. But otherwise, the decision change the Cu DAC transition pressures over the Ta DAC transition pressures was arbitrary. Once the pressure shift had been applied to the data, three of the five comparable transition pressures were consistent between different DACs. The exceptions are the d-fcc($oC4$) $\rightarrow$ bct transformations at 377 and 577 K, which occurs at different Ce volumes between different DACs. This implies that the d-fcc($oC4$) $\rightarrow$ bct transformation occurs at different pressures. Measuring the Ce volumes at the phase boundary shows that the Ce in the Cu cell is more compressed when compared to the Ce contained within the Ta cell, as expected from the pressure marker readings. There is no reason to discount any of these data points, and the origin of the large pressure discrepancy between the Ta and Cu data sets just before the d-fcc($oC4$) $\rightarrow$ bct transformation is unknown. The data points above 13 GPa were ignored when drawing the d-fcc($oC4$) stability region, and further work is required to confirm if either transition pressure is correct at elevated temperature.

4.4.1 The fcc(α) $\rightarrow$ bct transition

Similar to the d-fcc($oC4$) stability region, the location and gradient of the fcc(α) $\rightarrow$ bct phase boundary in P-T space appears to be dependent on the pressure marker used, in this case either Ta or NaCl. The boundary, as determined by Ta

has a very steep negative gradient, while the NaCl data suggests a more gradual gradient with a positive slope. Due to the very different gradients, a simple systematic error between the two boundaries can be ruled out. It is possible that the different hydrostatic conditions between the Ta and NaCl DACs could result in a different phase boundary. But, this would suggest that the pressures from the Ta DAC's would higher than what was measured, making the pressure differences between the two sets of data even more pronounced. Data on Ti collected by Errandonea *et al.* showed that the difference in transition pressure between a sample with no PTM, and a sample with NaCl PTM is ∼2 GPa [176], which is comparable to the pressure variation of the fcc(α) → bct transition between the Ta and NaCl DACs. But, Errandonea *et al.* also showed that the more hydrostatic the PTM, the higher the pressure required to observe a transition [176], which is the opposite to what is observed between the Ta and NaCl DACs.

In order to resolve this discrepancy, the fcc(α) sample volumes from a Ta DAC and a NaCl DAC were compared at 623, 725 and 773 K. While data were collected at 678 K using both NaCl and Ta as a marker, it proved impossible to compare the two data sets. Due to the lack of data collected by a Ta DAC above 800 K, no comparison could be made with the NaCl data points at 823 K. For these reasons a P_{shift} was not calculated for the transition at 678 K or 823 K.

The same comparison technique described previously was used to compare samples with Ta and NaCl markers. In general, the Ta marker read a higher pressure than the NaCl marker just before the fcc(α) → bct phase transition. However, the fcc(α) sample volumes at 630 K, 725 K and 772 K just before the fcc(α) → bct transition are very similar, (as illustrated in Figure 4.11). This implies that both phase boundaries are the same, and the discrepancy is due to pressure determination from different pressure markers. Unfortunately, this does not give any indication about which phase boundary is correct.

The fcc(α) volume vs temperature was plotted to provide insight into the location of the fcc(α) → bct phase boundary in P-T phase. As can been seen from Figure 4.11, in both the Ta and NaCl cells, the Ce volume just before the phase transition decreases as temperature increases. This suggests that as the temperature increases, the transition pressure should increase, and therefore, the fcc(α) → bct boundary has a positive gradient. Furthermore, the data collected from the Ce in NaCl cells, had far less contaminants and marker/sample overlap, and hence more likely to be correct. Unfortunately, the location of the boundary in P-T space as determined by the NaCl marker contradicts the fcc(α) → bct →

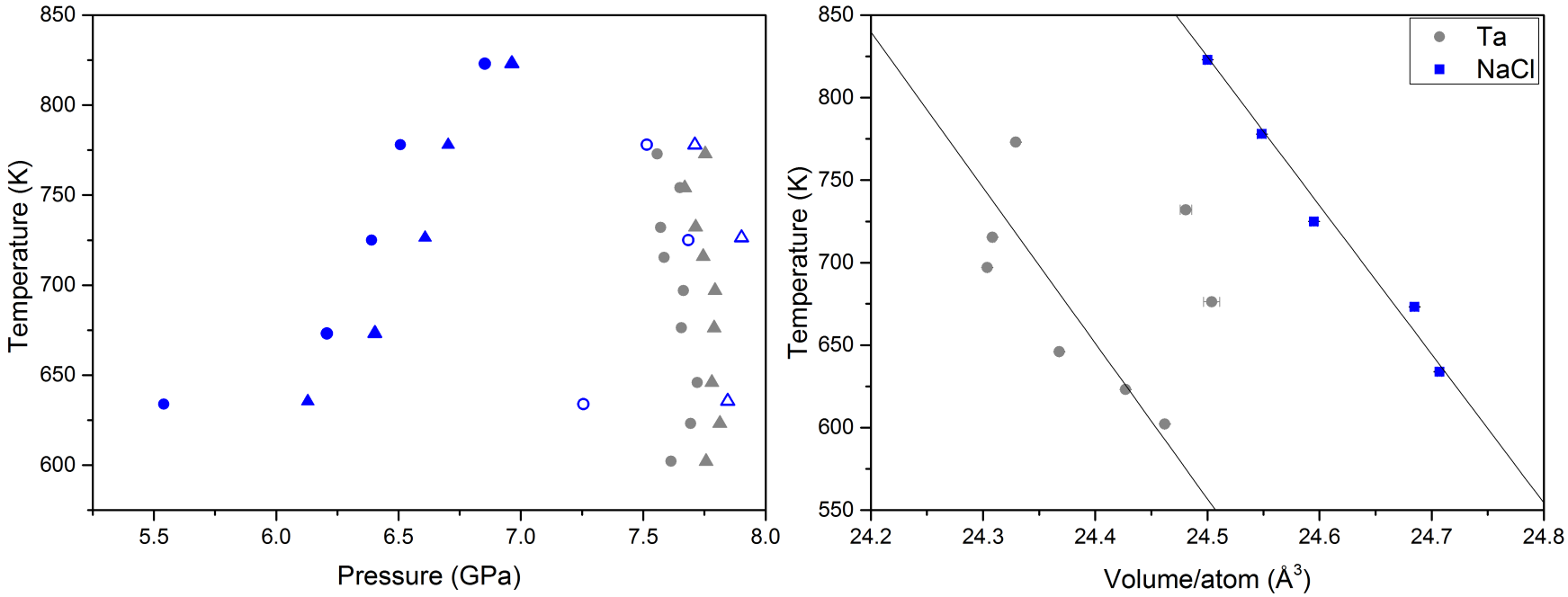

Figure 4.11 *Left: P-T plot of the fcc(α) (circles) $\rightarrow$ bct (triangles) phase boundary as determined using Ta (grey data points) and NaCl (blue points) upon compression. The hollow data points are the NaCl data points shifted by applying P_{shift}, highlighting that the transition occurs at the same Ce volume. Right: Plot of the fcc(α) volume just before the transformation to the bct phase against T in Ce. Blue squares are data points collected from cell using NaCl as a marker, while the grey circles are from cells with Ta marker. The solid lines are linear fits to each of the data sets.*

d-fcc($oC4$) $\rightarrow$ bct observed in previous, preliminary data. Taking into account all of the information above, the most plausible Ce phase diagram is presented in Figure 4.12.

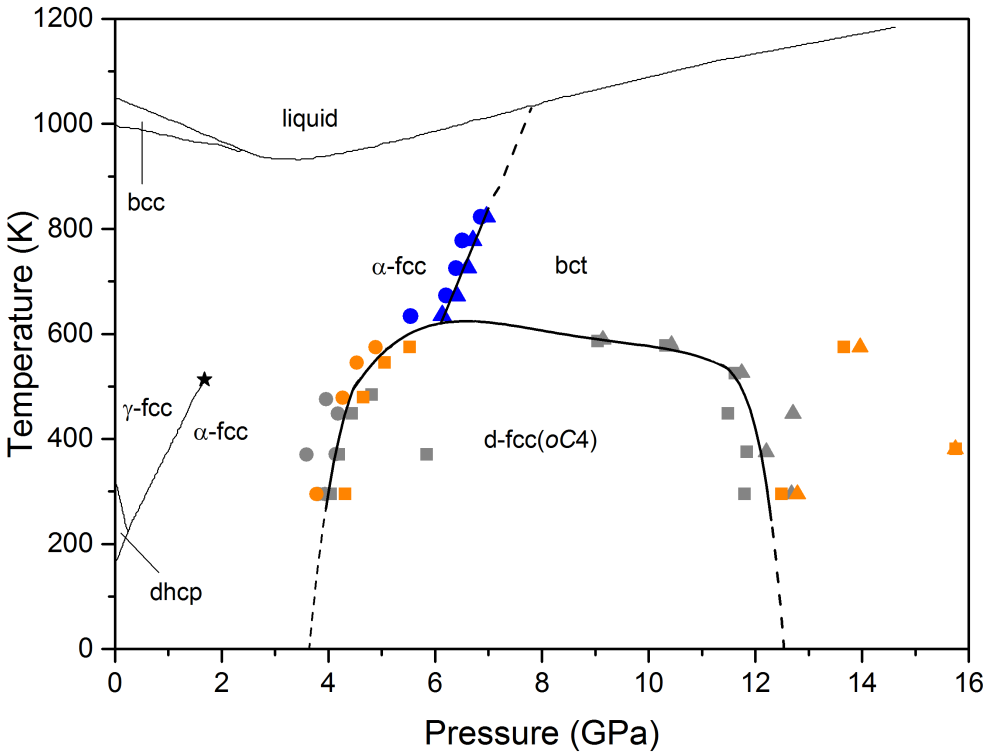

Figure 4.12 *Suggested phase diagram of Ce. Circles are where fcc(α) was observed, squares highlight the d-fcc($oC4$) phase and triangles mark the bct phase. Grey data points used Ta as a marker, orange data points utilized Cu marker, and the blue points employed NaCl. The fcc(α) $\rightarrow$ bct transition according to the Ta DAC's were not considered when determining the phase boundary. The solid black lines are suggested phase boundaries based from the data collected for this thesis. The thinner lines and the black star data point was taken from Schiwek et al. [143].*

Finally, the nature of the fcc(α) $\rightarrow$ bct transition at temperature was determined. No transition pressure hystersis was observed, which suggests a second order transition, but does not explicitly rule out a first order transition. The power law described by Evans *et al.* [106]:

$$y = A(x - x_0)^{\mathrm{B}} \tag{4.1}$$

was fitted to data collected on iso-thermal compression at 602 K, 623 K, 643 K and 772 K. A and B are variable parameters, y = c/a, x is V/V_0 and x_0 is set to the lowest V/V_0 while Ce is in the fcc(α) phase at that particular

isotherm. Up to 623 K, it appears that the transition is second order, with no discontinuity in the c/a ratio as a function of V/V_0. At 643 K, the power law becomes a poor fit to the data, and a very sharp change in c/a ratio is observed after the fcc(α) $\rightarrow$ bct transition, indicating a first order transition. At 773 K, no discontinuity is observed in the c/a ratio after the transition, similar to the iso-thermal compressions at 602 and 623 K (see Figure 4.13). One would expect a discontinuity in the phase boundary if such a change was occurring. However, no discontinuity in the phase boundary is detected as the temperature increases. It is suspect that a discontinuity was only observed at 643 K. It is possible that the pressure steps at 602 K, 623 K and 773 K were too large to detect the sharp drop in c/a indicating a first order phase transition, but as the pressure was changed by 0.1 - 0.2 GPa between data collection it seems unlikely.

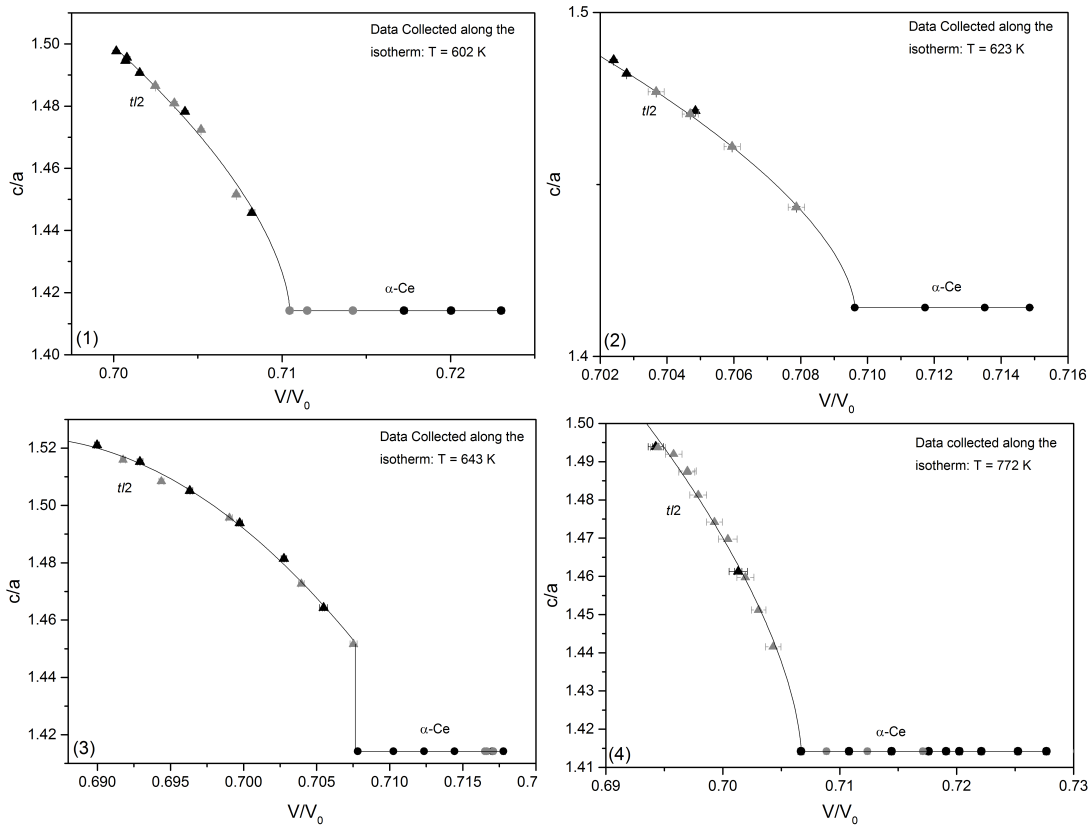

Figure 4.13 *Plots of the c/a ratio against V/V_0 at various isotherms in Ce. The lines in plots (1), (2) and (4) are weighted least-squares fits of the data to the power law (See Equation 4.1). The line in plot (3) is a weighted least-squares fit of the data to a quadratic function, and is a guide to the eye only. The black data points were collected on pressure increases, while grey data points were collected on pressure decrease. The circles mark the observation of fcc(α) phase and the triangles show where bct phase was found.*

4.5 Conclusions

Angle dispersive x-ray powder diffraction experiments have been performed on Ce up to 22.5 GPa and 773 K, examining the d-fcc($oC4$) stability region and the fcc(α) $\rightarrow$ bct transition. While the low pressure fcc(α) $\rightarrow$ d-fcc($oC4$) transition pressures are consistent across different experiments and with previous works, the transformation to the bct phase from d-fcc($oC4$) can occur anywhere between 12 and 15 GPa. This is inconsistent with the boundaries reported by Endo *et al.* and Tsiok *et al.*, who both suggest a well-defined d-fcc($oC4$) $\rightarrow$ bct phase line. Furthermore, the d-fcc($oC4$) $\rightarrow$ bct transition pressure is not reproducible at temperature and can't be explained due to different pressure markers, or by inconsistent use of backing discs with full conical openings. As a result, the d-fcc($oC4$) $\rightarrow$ bct phase line cannot be confirmed at elevated temperature. The two different phase boundaries for the fcc(α) $\rightarrow$ bct transition can be explained by the different markers reading different pressures at the same sample volume, and not by a change in hydrostatic conditions between the samples. Since the fcc(α) volume just before the transition decreases as temperature increases, the positive phase boundary measured by the NaCl appears to be the true boundary, which puts it at a slightly lower pressure compared to the boundary by Schiwek *et al.*

Finally, some evidence suggests that the fcc(α) $\rightarrow$ bct transition is first order, which is a discontinuity in the c/a ratio as the sample goes through the transition. No such discontinuity occurs at 602, 623 and 773 K and there is no observable hysteresis in the transition pressure at any temperature. This suggests that, if the boundary is first order, the data collected at those temperatures were not taken in small enough pressure steps to adequately resolve the transition properly, but this seems unlikely due to the small pressure steps between data collection. The first order nature suggested here confirms the conclusion reached by Zhao *et al.* and contradicts the data collected by Schiwek *et al.*

Chapter 5

Lanthanum

5.1 Introduction

Surprisingly, there is relatively little information on La's behaviour at high pressure compared to its neighbours, Ce and Pr. There have been substantially fewer high-pressure studies on La, no in-depth report on the structure of La's d-fcc phase, and the behaviour of La above 100 GPa is completely unknown. This is surprising, as La is unique amongst the lanthanide metals due to the lack of $4f$ electrons at ambient conditions, and electron occupation of the $4f$ shell is predicted to occur only at ∼1100 GPa [177]. Despite this lack of $4f$ electrons, La crystallizes in the dhcp structure at ambient conditions, which is observed in all other trivalent lanthanide metals (excluding Ce) at various pressures and room temperature, and exhibits the trivalent lanthanide transformation sequence (dhcp → fcc → d-fcc) on pressure increase [105]. Piermarini *et al.* reported the presence of a fcc structure in La at 3.5 GPa using x-ray diffraction techniques, and McWhan *et al.* determined the dhcp → fcc transition to occur at 2.4 GPa [178].

The first x-ray diffraction study on La's d-fcc phase was performed by Grosshans *et al.* [105], who observed the appearance of the d-fcc superlattice reflections at 7 GPa. Grosshans *et al.* suggested the existence of a soft phonon mode, $\overrightarrow{q}$, causes the static distortion of the fcc structure, where $\overrightarrow{q}$ corresponds to the zone-boundary L point in the Brillouin zone of the fcc lattice, and points along the (111) cubic direction, which is the c axis in the hexagonal representation of the

fcc lattice [105]. The zone boundary softness results in a distortion which doubles the length of the hexagonal c axis. As a result, Grosshans *et al.* assigned the $hP6$ structure to the d-fcc phase, and observed the d-fcc superlattice reflections to continuously increase in intensity as pressure was increased [105].

Porsch *et al.* later fitted various structures to integrated diffraction profiles from La's d-fcc phase, with the aim of solving its structure. They determined that there were 4 possible candidates. They stated that due to the absence of any splitting of the fcc (200) reflection at the fcc $\rightarrow$ d-fcc phase transition, which is consistent with the persistence of a threefold-rotational axis, the $hR24$ structure first reported by Hamaya *et al.* in Pr was a candidate for the structure of La's d-fcc phase. However, Porsch *et al.* made no attempt at structural refinements, citing concerns about textural effects affecting the EDXRD peak intensities. They also suggested the $oC8(1)$, $oC8(2)$ and $aP1$ structures as possible candidates for La's d-fcc phase (as described in Table 3.2). The fcc $\rightarrow$ d-fcc transition is considered to be second order, since there is no measurable volume discontinuity between the two phases [104]. Using Landau theory, Porsch *et al.* determined that the fcc $\rightarrow$ $oC8(1)$ transition to be a second order transition, while transitions to the $hR24$, $oC8(2)$ and $aP1$ structures were first order transition. Porsch *et al.* concluded that the only valid structure for La's d-fcc phase was the $oC8(1)$ structure [104].

A further study by Porsch *et al.* compressed La up to 67 GPa [102], to determine if it underwent the "volume collapse" phase transition to the low symmetry structures found in other lanthanide metals [11]. They observed that the d-fcc satellite reflections decreased in intensity above 53 GPa, and had completely disappeared at 60 GPa, leading to a re-entrant transition back into the fcc structure. Due to the presence of the d-fcc structure in La, the authors concluded that $4f$ electrons do not affect the stability of the d-fcc structure in the lanthanides. Porsch *et al.* also reported that the high-pressure fcc structure found at 60 GPa is the same the fcc structure found between 2.3 and 7 GPa [102].

Currently, La is the only known trivalent lanthanide that undergoes a re-entrant phase transition back to fcc. However, similarities can be drawn with divalent Yb, which undergoes the transformation sequence: fcc $\rightarrow$ bcc $\rightarrow$ hcp $\rightarrow$ fcc(II) under pressure [179]. Like La, Yb transforms back into the fcc structure as pressure increases. Eventually, Yb [117] adopts the $hP3$ structure [180] found in Nd and Sm above 35 GPa and 36 GPa respectively [116, 117]. This raises the possibility that La might also adopt the $hP3$ structure if compressed sufficiently.

The first attempt to map out the phase diagram of La above room temperature was performed by McWhan *et al.* using resistivity measurements. They determined that the dhcp → fcc phase boundary has a negative gradient [181], which was later followed to below 150 K by Balster *et al.* [182]. They also observed kinks in the superconducting transition temperature, T_c, as a function of pressure, at pressures corresponding to the dhcp/fcc and fcc/d-fcc phase boundaries. Extrapolating the boundaries further suggested the dhcp/fcc/d-fcc triple point to be at ∼100 K and ∼5.3 GPa. The kinetics of the dhcp → fcc transition were studied by Markau *et al.* using x-ray diffraction [183], and they obtained a similar dhcp → fcc phase boundary to both Balster *et al.* and McWhan *et al.* Markau *et al* also established a region of hysteresis between the dhcp and fcc phases. The most recent high-pressure high-temperature study of La was performed by Seipel *et al.* who focused on the fcc → d-fcc phase transition [142], and extended the fcc → d-fcc phase boundary to high temperature. The current phase diagram of La is shown in Figure 5.1.

5.1.1 Outstanding Issues

Oddly, La is one of the very few elements that has not been studied above 100 GPa, (another being Pm due to its radioactive nature [110]). Since La and Yb share a similar re-entrant phase transition, there is the possibility that La will adopt a more complex structure at higher pressures, despite lacking $4f$ electrons. There also hasn't been a comprehensive structural study of the d-fcc phase found in La using Rietveld refinement techniques. While the phase diagram is well known at low pressures, the re-entrant transition has not been studied at high temperature. The work in this thesis aims to shed some light on these issues, to definitively determine the structure of the d-fcc phase and to determine the structural sequence in La to 200 GPa for the first time.

5.2 Experimental Details

All of the samples used in this thesis chapter were cut from high purity (99.99+%) La ingots, provided by U. Schwarz of the MPI für Chemische Physik fester Stoffe. For room temperature experiments the samples were loaded into MB diamond anvil cells equipped with tungsten gaskets and loaded with either a small (∼2 μm)

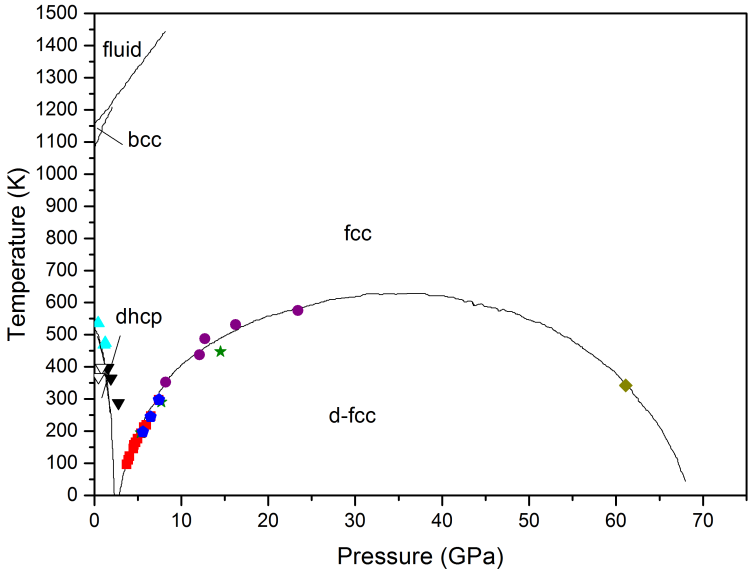

Figure 5.1 *The currently published phase diagram of La. The melt and fcc/bcc phase lines are taken from Young [10], the dhcp/fcc phase line is the center of the "region of indifference" discussed by Krüger et al. [11], and the fcc/d-fcc boundary is from Seipel et al. [142]. The purple circles are data points from Seipel et al. [142], the yellow diamond point is from Porsch et al.[102], blue triangles are from McWhan et al. [181], and inverse triangles are from Merkau et al. [183] with solid black points on pressure increase and hollow points on pressure decrease. The red squares are data points taken from Balster et al. [182]; the green stars are from Krüger et al. [11] referencing Grosshans [184]; and the blue pentagons are data points from Grosshans et al. [185].*

piece of ruby, or a 1 μm thick piece of Ta foil as a pressure calibrant. The cells were loaded in an oxygen-free, water-free environment (<1 ppm O_2 and <1 ppm H_2O). A variety of PTMs have been utilized in the literature, with mineral oil being the most common [102, 104], but silicon oil [142] and NaCl [182] were also used. In general, no pressure transmitting medium was included in the current studies to prevent sample contamination, and to minimise any chemical reactions occurring within the sample chamber during sample loading. A single LLNL DAC for extremely high-pressure studies at 300 K, which will be referred to as the HP cell, used silicon oil as a pressure transmitting medium. The room temperature data were collected at the high-pressure beamline P02.2 at PETRA-III, DESY using an incident x-ray wavelength ∼0.289 Å, and a Perkin Elmer (XRD1621) detector placed ∼360 mm from the sample. The extremely high-pressure data were taken on the high-pressure beamline I15 at the DLS, utilizing an incident wavelength of ∼0.413 Å and a MAR345 detector placed ∼350 mm from the sample.

High-pressure high-temperature data were collected at multiple high-pressure beamlines at various synchrotron facilities, beamline P02.2, ID09 and I15 at PETRA-III, ESRF and DLS, respectively, using incident x-ray wavelengths of ∼0.485 Å, ∼0.416 Å and ∼0.423 Å, respectively. The DACs were all equipped with slit backing discs and tungsten gaskets, with the cells being prepared in the same way as described in the previous paragraph for the room temperature experiments, and in experimental details sections in other chapters. Heat was applied to the sample via the copper heating block and the vacuum vessel as described in Section 2.5. Ta, Au and Ruby were used as pressure markers. The equation of states used to determine pressures are referenced in Section 2.2.2. The methods of Singh *et al.* were utilized to determine if samples were experiencing non-hydrostatic effects (see Section 4.2). In all cases no non-hydrostatic effects were detectable up to 60 GPa. Only the HP cell went above 60 GPa, and no detectable non-hydrostatic effects were measured up to 71 GPa. Above this pressure it became very difficult to employ the methods by Singh *et al.* [173], since too few peak positions could be determined with sufficient precision.

5.3 Results

Similar to Section 4.3, data were collected using DAC's loaded with various pressure markers. As with the previous chapter, DACs loaded with Ta as a

marker will be referred to as Ta DACs or Ta cells, and a DAC which used Au as a marker will be referred to as an Au DAC. Finally ruby DAC refers to the single DAC which utilized ruby as a marker.

5.3.1 Characterisation of Contaminants

While every effort was made to load high purity samples without contaminants, small amounts of contaminants were detected in most samples. It was not always possible to avoid contaminated areas of the sample with the x-ray beam during the DLS and ESRF experiments at I15 and ID09, due to the larger beam sizes used on those beamlines. Two different contaminants were identified, both of which adopted the fcc structure. During experiments, the contaminant with the smaller unit cell volume, labelled contaminant 1, was more prolific. Attempts were made to locate a clean sample area by moving the sample in the plane perpendicular to the direction of the synchrotron beam, but without success. The contaminant with the larger unit cell volume, labelled contaminant 2, was less abundant, and typically it was possible to align the sample in such a way that the synchrotron beam did not diffract from contaminant 2. An integrated diffraction profile of d-fcc La fitted to the $oI16$ structure (discussed later) and both contaminants is presented in Figure 5.2. Contaminant 1 has a very similar lattice parameter to the so called s-fcc phase of LaH_2 as reported by Machida *et al.* [186]. Contaminant 2 was not identifiable, but it is unlikely to be La_2O_3, since La_2O_3 has a hexagonal structure up to ∼20 GPa [187] (see Figure 5.3).

5.3.2 Improving the Data Quality

As has been shown in Section 3.2, solving the structure of the d-fcc phase requires that the many doublets and triplets be as well-resolved as possible. Evans *et al.* reported that annealing the d-fcc phase of Pr led to significant sharpening of the diffraction peaks [106]. Substantial time and effort were therefore devoted to improving the quality of the diffraction data analysed in this thesis, by pressure cycling the sample, annealing the sample at various temperatures and compressing the sample at temperatures above 300 K. The best diffraction data from the d-fcc phase were collected upon pressure decrease with the La coming back into the d-fcc phase from the fcc phase found at ∼55 GPa, with the peaks being 50% sharper compared to those typically found on compression. Pressure

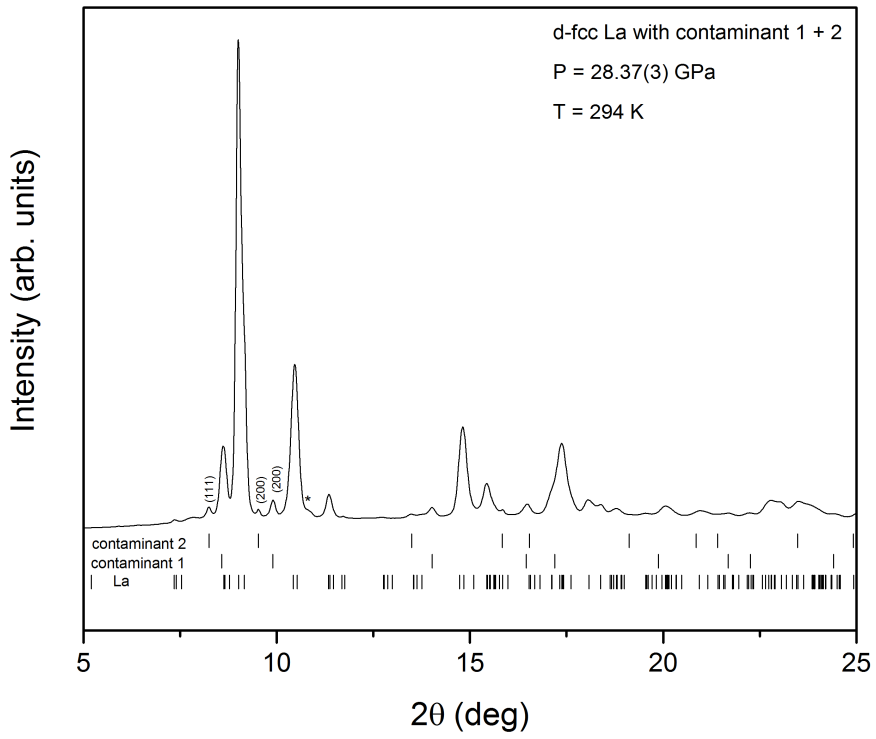

Figure 5.2 *Integrated diffraction pattern of d-fcc(oI16) La and both cubic contaminants at ∼28 GPa. The ticks marks indicate the calculated peak positions of the d-fcc(oI16) phase and the two contaminants. The (200) peak from contaminant 1, and the (111) and (200) peaks of contaminant 2 are labelled. The higher-angle contaminant peaks are dwarfed by the sample peaks. The asterisk identifies the (110) Ta peak.*

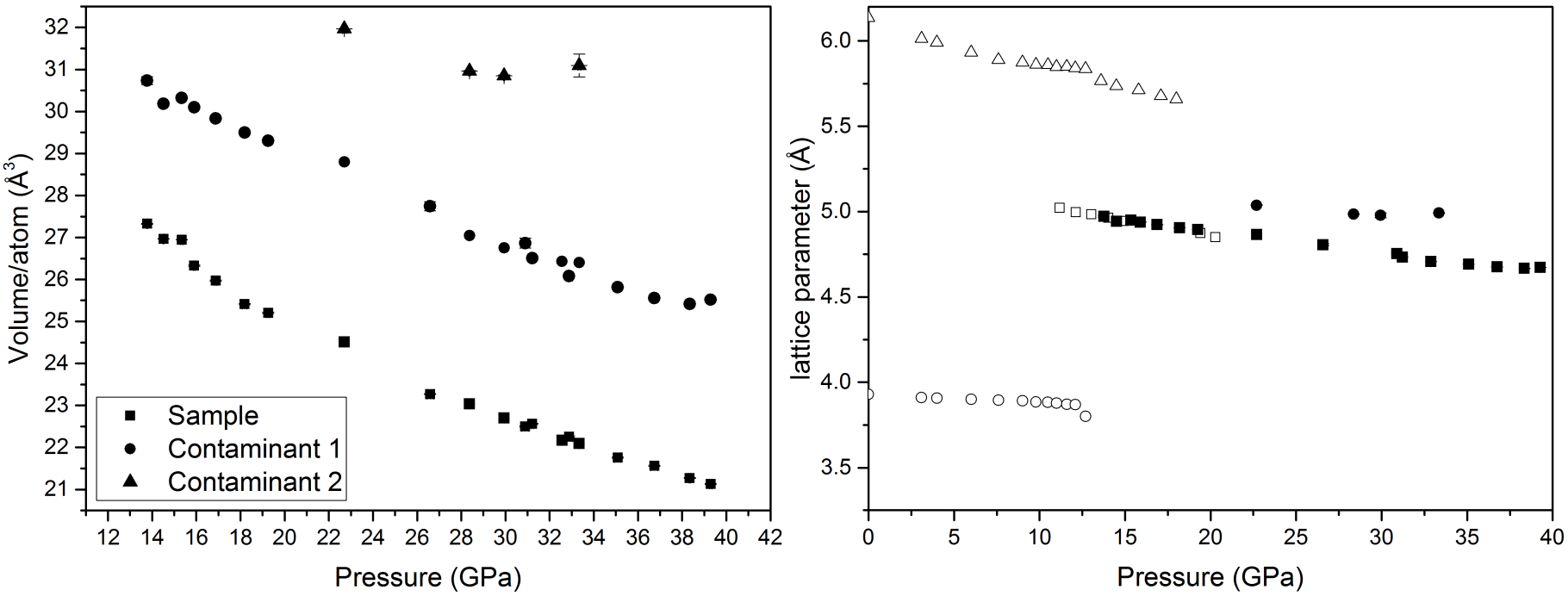

Figure 5.3 *Left: Plot of the atomic volume of d-fcc La and both cubic contaminants against pressure. The square data points are from d-fcc La, the circles are from contaminant 1 and the triangles are from contaminant 2. The volume of contaminant 2 was calculated from the (200) peak, while contaminant 1 was typically calculated from the (200) peak but for one data point, the volume needed to be calculated using the (111) reflection instead. Right: Pressure dependence of the LaH_2 and La_2O_3 lattice parameters. The unfilled squares are the lattice parameters of s-fcc LaH_2 collected by Machida et al.[186], while the solid black squares are data from contaminant 1 collected during this thesis. The black circles mark the lattice points of contaminant 2. Due to the nearly complete data overlap, contaminant 1 is almost certainly LaH_2. The hollow circles and hollow triangles are the a and c lattice parameters, respectively, of La_2O_3, as reported by McClure [187].*

cycling and annealing the sample also improved the data quality, though the peak sharpening was not as pronounced as that obtained by decompression back though the re-entrant transition. On decompression, the various transitions occurred ∼2 - 4 GPa lower compared to compression. Compressing the sample at high temperature proved to be ineffective, due to the dome-like stability region of the d-fcc phase (see Figure 5.1). As temperature is increased, the d-fcc doublets merge back to singlets as the ceiling of the fcc/d-fcc phase boundary is approached (see Figure 5.4).

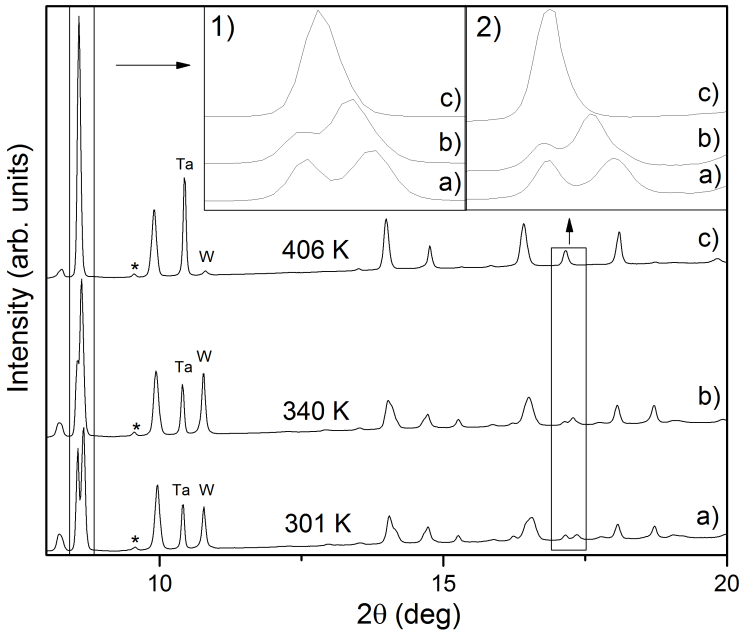

Figure 5.4 *Integrated diffraction profile from d-fcc(hR24) La at 13.5 GPa and a) 301 K, b) 340 K and c) 406 K. As the temperature increases, the peak splitting effects which are used to identify the d-fcc phase's structure become less pronounced, and merge into singlets above 340 K as the structure enters the fcc phase. Inserts 1 and 2 highlight the recombination of the d-fcc(hR24) (006)/(202) and d-fcc(hR24) (00,12)/(404) doublets, respectively, as temperature increases.*

5.3.3 La's d-fcc Phase

Multiple data sets were collected from La samples upon compression. Three were collected at room temperature, each with a different pressure marker; one each with Ta, Au and ruby. The dhcp phase was observed up to 3.2 GPa but was completely gone by 6.4 GPa. The super lattice reflections signalling the transition into the d-fcc phase first appeared at 9.6 GPa. At room temperature the splitting

of the fcc singlets into d-fcc doublets/triplets in La is less pronounced than in Pr [11], but is first observable at 10.8 GPa. Attempts were made to fit previously proposed d-fcc structures (see Table 3.2, Section 3.2). The majority of structures gave significant misfits: observed peaks were not predicted and many calculated peaks were not present in the integrated diffraction patterns. Three structures were able to predict all of the observed peaks, the $hR24$ structure, the $oI16$ structure and the $oP16$ structure. However, the $hR24$ structure was favoured since it required fewer refineable parameters in order to fit the data. The $hR24$ structure remains stable up to ∼22 GPa upon compression at 300 K.

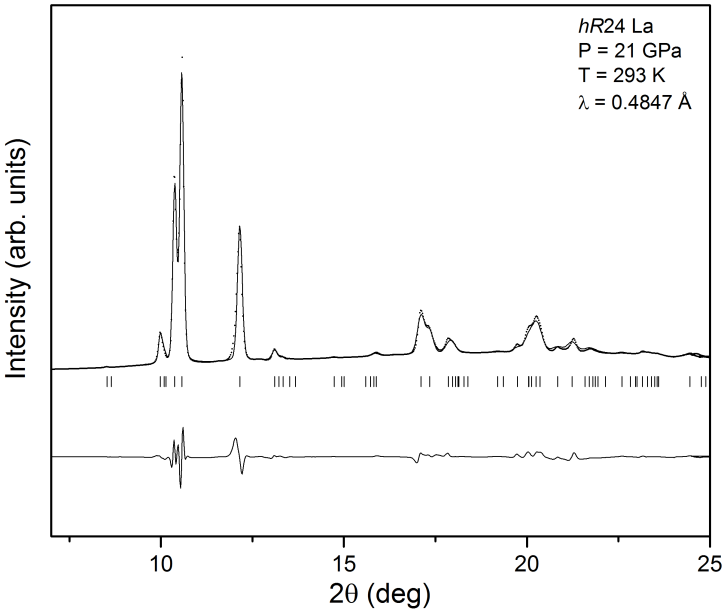

Figure 5.5 *Rietveld refinement of the hR24 structure to an integrated diffraction pattern of d-fcc La at 21 GPa. The dots are the data points while the solid black line is the calculated intensity of the fit. The tick marks indicate the position of the calculated peaks. The hR24 structure is able to explain all of the observed peaks. The diffraction pattern was collected from a sample on decompression from the high pressure fcc phase above 60 GPa. The slightly misfitted (2-24) hR24 peak at 12.2 deg is due to the presence of the (110) Ta directly underneath it.*

Upon further pressure increase at 300 K, the d-fcc($hR24$) (006)/(202) doublet experiences intensity changes between 19-22 GPa, similar to that observed during the d-fcc($hR24$) → d-fcc($oI16$) transition found in Pr by Evans *et al*, and these are reverseable on decompression [106]. This behaviour is also observed in the d-fcc($hR24$) (00,12)/(404) doublet, with the (00,12) peak slowing growing in intensity while the (404) peak becomes less intense. However, during this process the doublet appears to transform into a flat topped peak, strongly suggestive of

an unresolved triplet.

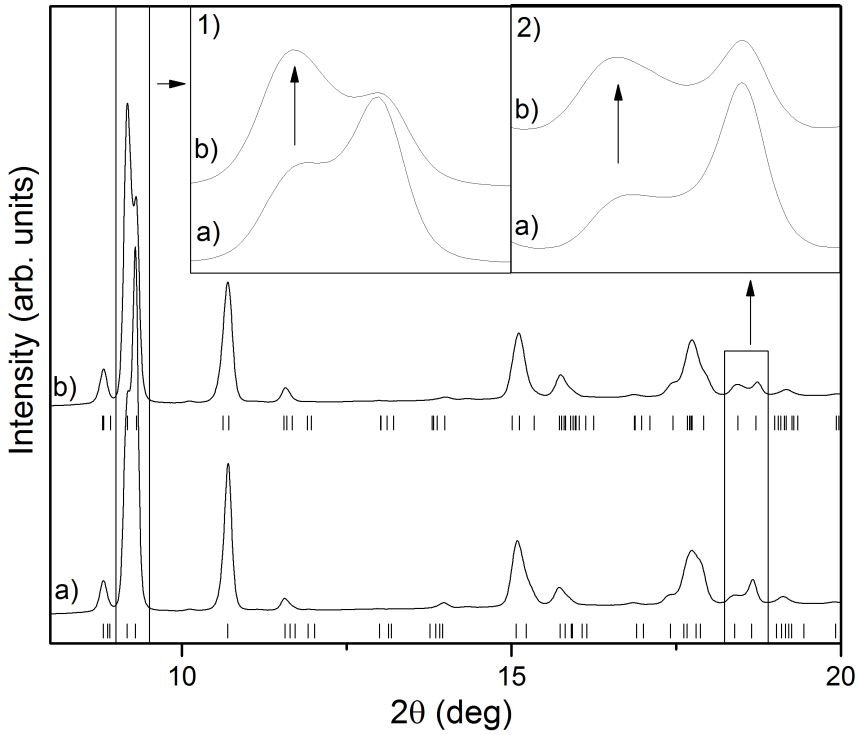

Figure 5.6 *a) Integrated diffraction profiles on pressure decrease of a) d-fcc(hR24) La at 23.7 GPa and b) d-fcc(oI16) La at 24.5 GPa, highlighting the changes in intensity experienced by La undergoing the d-fcc(hR24) → d-fcc(oI16) transformation. The tick marks below each profile indicate the position of each structure's predicted peaks.*

The presence of a new peak is at odds with both the $hR24$ and $oI16$ structures. The intensity distribution around the Debye-Scherrer ring is uneven, and in an attempt to extract more information, the raw image file was split into 8 equal, 45 degree segments and each was azimuthally integrated separately. This revealed a very sharp third peak in a single segment (see Figure 5.7), and while some d-fcc structures predict multiple peaks at this 2θ instead of a doublet, such as $hP6$, each structure also has significant misfits in other parts of the pattern. It should be noted that the extra peak has only been clearly observed in a single integrated diffraction pattern, and attempts to observe this third peak in other integrated diffraction patterns were unsuccessful. Another explanation for the appearance of an extra sharp peak is that the sample had adopted a d-fcc($hR24$)/d-fcc($oI16$) mixed phase in that particular pattern. However, considering the shape of the peak, and since it was only observed in one segment of one diffraction pattern it is very likely that the peak is not from a La phase.

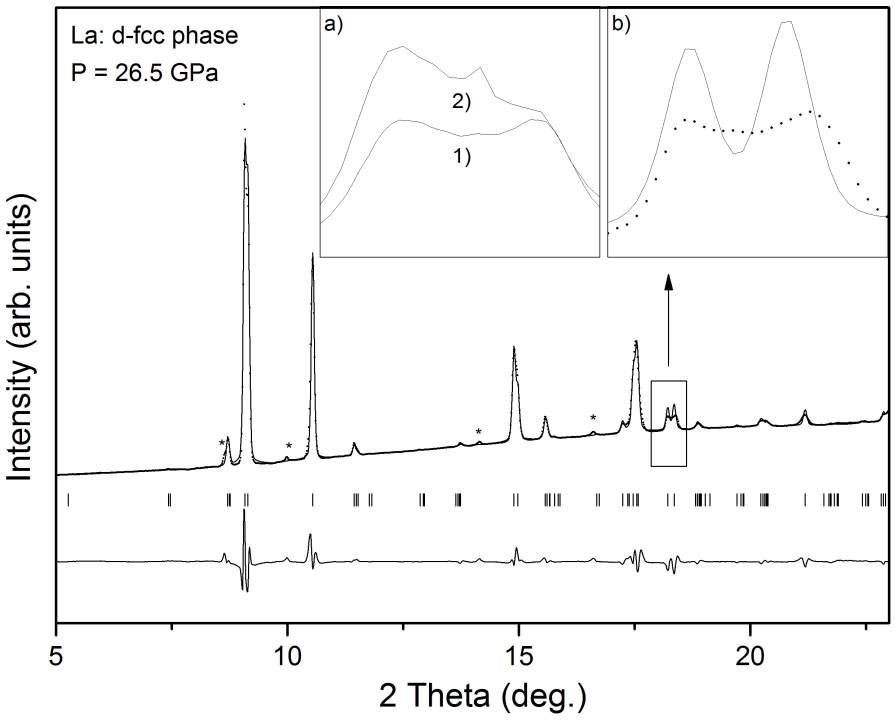

Figure 5.7 *Integrated diffraction profile of d-fcc La at 24.5 GPa and 412 K, fitted to the hR24 structure. Despite the good fit, the (00,12)/(404) doublet has been flattened to a plateau and does not fit the doublet predicted by the hR24 structure, as highlighted in insert b). Insert a) compares 1) the integrated diffraction profile of the full (00,12)/(404) Debye-Scherrer ring to 2) an integrated diffraction profile of a single 45º arc of the (00,12)/(404) ring.*

Attempts were made to fit the various proposed structures to the integrated diffraction profiles of d-fcc La above 22 GPa. Since no peaks emerge or disappear, and any new splitting effects from the new phase are unresolved, the $hR24$ and $oI16$ structures are again, viable solutions. The $oP16$ structure was discounted, since it predicts many peaks which are not observed. Rietveld refinements of both the $hR24$ and $oI16$ structure to La's d-fcc phase above 22 GPa found that, while both fit the data well, the $oI16$ fits slightly better (see Figure 5.8). This suggests that above 22 GPa, La does adopt the $oI16$ structure, similar to Pr [106], but the structural changes are obscured by La's wider peaks.

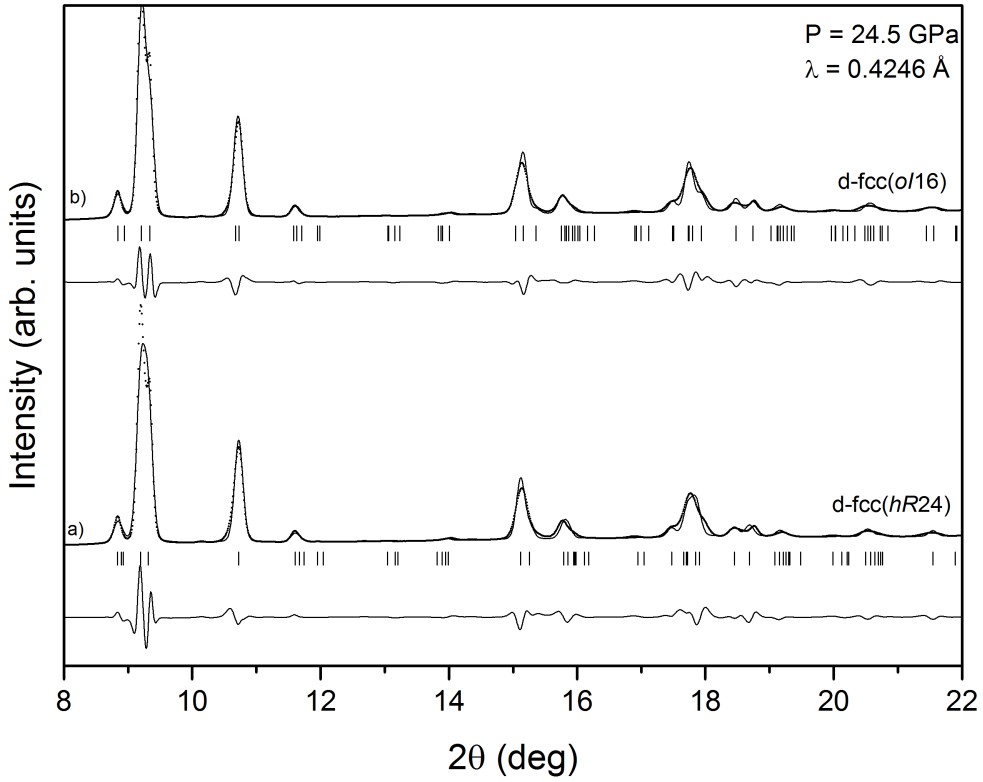

Figure 5.8 *Rietveld refinements of d-fcc La after the intensity changes to a) the hR24 structure and b) the oI16 structure. Both structures are good fits to the d-fcc phase of La, with all of the observed peaks predicted by both structures.*

The doublets and triplets that characterise the various d-fcc structures remain observable up to 40.1 GPa at room temperature, while the d-fcc phase's superlattice reflections disappear by 54.0 GPa, signalling the re-entrant transformation to the fcc phase is complete.

5.3.4 Expanding La's phase diagram

Data were also collected along multiple isotherms to determine the d-fcc phase's region of stability, and to determine the location of the (006)/(202) intensity changes in P-T space, and therefore map out the d-fcc($hR24$) $\rightarrow$ d-fcc($oI16$) phase boundary.

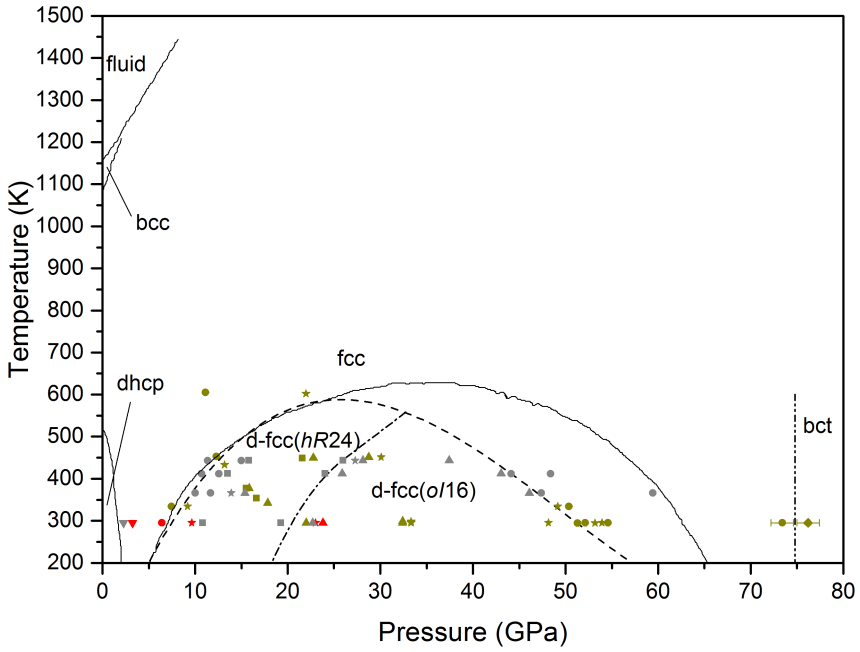

Figure 5.9 *Phase diagram of La, imposed on the phase diagram from the literature. Inverse triangles show where the dhcp phase was found, circles highlight where fcc was observed, stars indicate the d-fcc phase with inadequate peak splitting to determine the structure, squares show the d-fcc(hR24) phase, upward triangles mark out the d-fcc(oI16) phase and the diamond signals the bct phase. The grey data points were collected from Ta DACs, red data points were collected from ruby DACs and the dark yellow points were collected from Au DACs. The dashed line indicates the fcc/d-fcc phase boundary, while the dot dash line shows the d-fcc(hR24)/d-fcc(oI16) phase boundary, as determined by the (006)/(202) peaks swapping intensities.*

The drawn phase boundaries suggest that the fcc phase gradually becomes more dense than the d-fcc phase as pressure increases, leading to the dome like stability region of the d-fcc phase, and calculated densities before and after the transition confirm that this is the case. While there is no data near the top of the d-fcc stability region to determine the location of the fcc/d-fcc($hR24$)/d-fcc($oI16$) triple point, an analogy can be drawn with the dome like stability region of the bcc/fcc phases in lithium [188]. Extrapolating the bcc/fcc phase boundary places the bcc/fcc/melt triple point near the apex of the dome, which suggest that the fcc/d-fcc($hR24$)/d-fcc($oI16$) triple point would also be near the apex of the d-fcc region.

The various transition pressures at room temperature, and the d-fcc($oI16$) $\rightarrow$ fcc transition pressures at high temperature, are consistent between different experiments. But, similar to the Ce results, there are obvious inconsistencies

between the data collected at high pressure and temperature from the Au and Ta DACs. The Ta DACs generally had the d-fcc($hR24$) $\rightarrow$ d-fcc($oI16$) phase transition occurring at higher pressures, compared to the Au DACs, suggesting a systematic error between the two markers' EoSs. Pressure calculators were made using the data collected from Ta DACs, due to more numerous data points and smaller temperature variation between said data points. Two pressure calculators were made at 373 K and 444 K, and two P_{shift} were determined, -0.09(4) GPa and 3.80(11) GPa respectively.

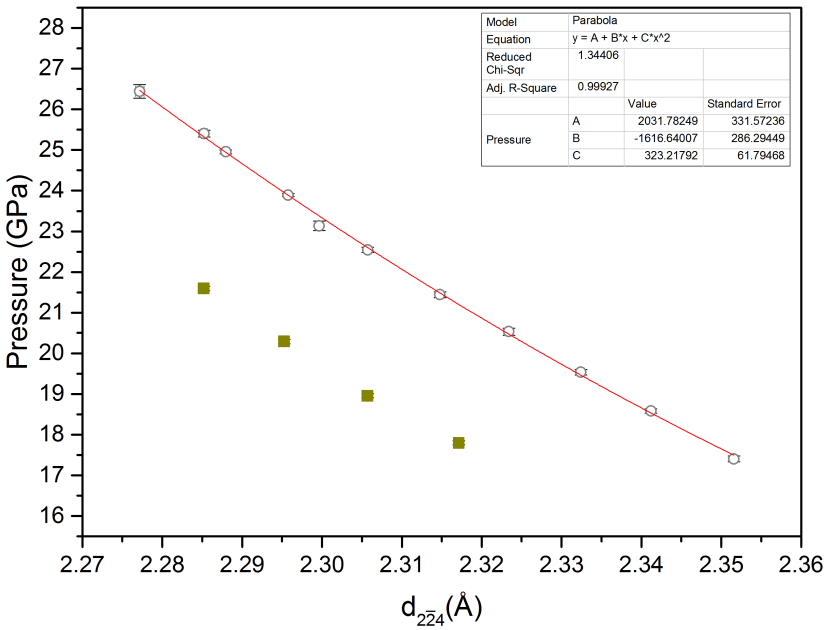

Figure 5.10 *Plot of pressure, as measured by the Ta and Au markers, against the d-spacing of the d-fcc(hR24) La (2-24) singlet. The unfilled grey circles indicate pressures determined using Ta, and the dark yellow squares have had the pressures determined by Au. A 2^{nd} order polynomial was fitted to the Ta data to create a pressure calculator. The Au pressures are consistently lower than the Ta pressures during iso-thermal compression at 445 K, by around 3.8 GPa.*

Fortuitously, applying P_{shift} to the transition pressures at the corresponding from Au DAC's makes them consistent with the data collected from Ta DAC's (see Figure 5.11 and Figure 5.9). Again, there was no particular reason to modify the Au DAC data over the Ta DAC data other than to make the phase diagram easier to draw. This means that the phase transformations are occurring at the same location in P-T space, and suggests that there are problems with the EoS used to determine pressure from the marker. It is very peculiar that at 366 K, fcc La directly transforms into the d-fcc($oI16$) phase, at $\sim$7 GPa compared to

T (K)	Marker	$d_{2\text{-}24}$ (Å)	P_{calc}(Ta)	P_{marker} (GPa)	P_{shift} (GPa)
443.85	Ta	2.2853(4)	25.32(5)	25.41(8)	
448.75	Au	2.28521(9)	25.324(13)	21.60(5)	
	Ta-Au		0.00(5)	3.81(9)	3.80(11)

Table 5.1 *Table showing the pressure shift needed to make data from the Au DAC consistent with the Ta DAC data. P_{calc} is the pressure of the sample according to the sample volume, which is the same in both cells, and the pressure calculator as determined using Ta. P_{marker} is the pressure according to the marker. P_{shift} is the offset added to the pressure as determined by the Au marker, so that the Au DAC data are made consistent with the Ta DAC data.*

the d-fcc($hR24$) → d-fcc($oI16$) transition at 300 K and 444 K (see Figure 5.11). All of the high-temperature data were collected from DACs equipped with slit backing discs, and as was the case with the Ce data, regions of the detector were unable to collect diffracted radiation from the sample (see Figure 4.5 in Section 4.3). This resulted in the inability to collect intensity from the complete Debye-Scherrer ring. While this restriction is not an issue for good powders with uniform Debye-Scherrer rings, the Debye-Scherrer rings observed in the raw 2-D image from the d-fcc phase of La are very textured. This raises the possibility that, due to the orientation of the sample within the DAC, combined with the sample's textured nature, the d-fcc($hR24$) and d-fcc($oI16$) structures are being incorrectly identified.

A diffraction pattern collected from a DAC with slit backing discs was simulated by creating a mask in the program Fit2D, which was applied to a raw 2-D image of d-fcc lanthanum collected at room temperature, from a DAC with Boehler-Almax backing discs. This resulted in only a strip of the observed pattern being azimuthally integrated by the Fit2D program. Two masks were created, to simulate two different orientations of the sample. Applying a mask can dramatically alter the intensity distribution of the d-fcc($hR24$) (006)/(202) doublet, as shown in Figure 5.12. Applying one particular mask changes the doublet intensities in such a way to suggest the sample has adopted the d-fcc($oI16$) structure, while applying a different mask changes the position of the (006) peak. This result raises the possibility that the fcc → d-fcc($oI16$) transition at 366 K is incorrect, while the fcc → d-fcc($hR24$) and d-fcc($hR24$) → d-fcc($oI16$) transitions at 366 K are unobservable, due to the partial, textured doublet rings in the raw image.

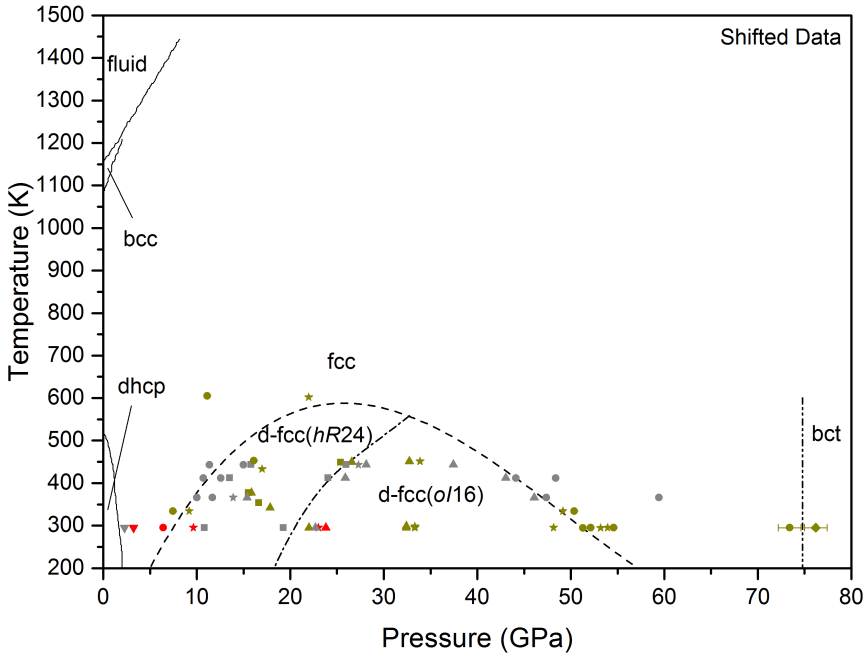

Figure 5.11 *Proposed phase diagram of La with the yellow points at 373 K shifted by -0.09(4) GPa, and the yellow points at 445 K shifted by 3.80(11) GPa. Inverse triangles are where the dhcp phase was observed, circles highlight the presence of the fcc phase, stars indicate the d-fcc phase with inadequate speak splitting to determine the structure, squares show where the d-fcc(hR24) phase was found, upward triangles mark the d-fcc(oI16) phase and the diamond signals the bct phase. The grey data points were collected from Ta DACs, red data points were collected from a ruby DAC and the golden points were collected from Au DACs. The dashed line indicates the fcc/d-fcc phase boundary, while the dash dot line shows the d-fcc(hR24)/d-fcc(oI16) phase boundary as determined by the (006)/(202) peaks swapping intensities.*

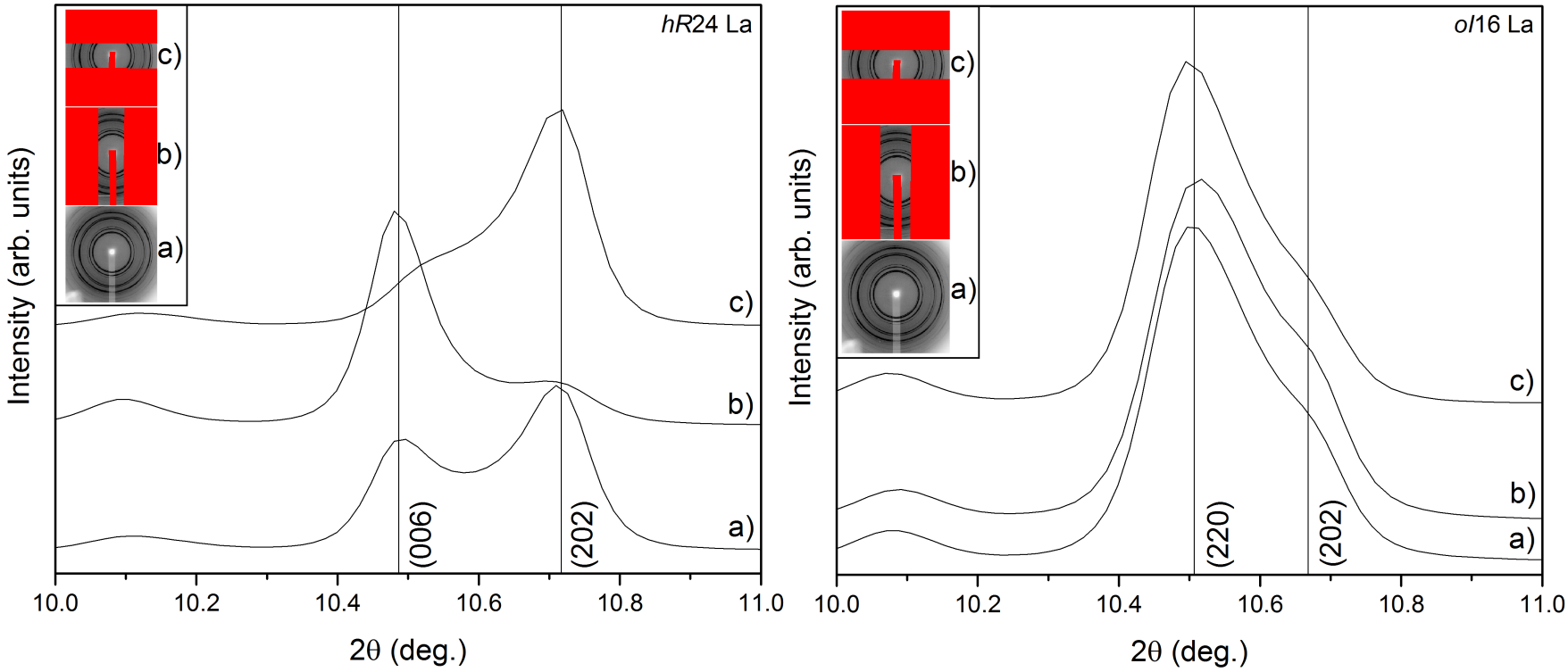

Figure 5.12 *Left: Integrated diffraction patterns of d-fcc(hR24) La focusing on the (006)/(202) doublet with a) no mask, b) a vertical slit mask and c) a horizontal slit mask. Right: Integrated diffraction patterns of d-fcc(oI16) lanthanum focusing on the (220)/(202) doublet with a) no mask, b) a vertical slit mask and c) a horizontal slit mask. The inserts shows the mask that was used for each of the corresponding integrated diffraction profiles.*

5.3.5 The behaviour of La above 76 GPa

Above 76 GPa, various fcc peaks become slightly asymmetric. Upon further compression, the asymmetry becomes more apparent and eventually the peaks split into doublets at ∼150 GPa. These new doublets remain pronounced up to 280 GPa, the highest pressure reached. Of the five observable fcc peaks, the (200), (220) and (311) peaks all split into doublets, while the (111) and (222) reflections remain singlets. This is consistent with the transformation to the bct structure. This suggests that above 76 GPa, La begins a very sluggish transformation to the bct phase, as seen in Figure 5.13. A fit to the bct structure is shown in Figure 5.14.

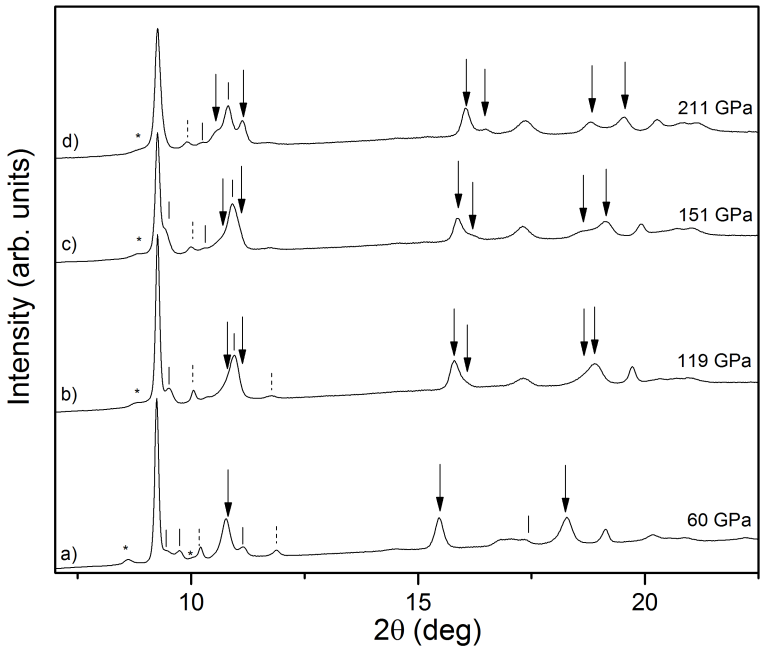

Figure 5.13 *Integrated diffraction profiles of a) fcc La, b) La with the fcc (200), (220), (311) lattice reflections becoming asymmetric, c) bct La with the fcc (220) peak beginning to split and the fcc (311) peak fully split, d) fully transformed La with the bct structure. The arrows, from left to right, highlight the fcc (200), (220) and (311) lattice reflections splitting into doublets as pressure increases. The asterisks indicate contaminant peaks, the solid ticks highlight both ambient and compressed Re peaks, the dashed ticks show the Au marker peaks. The upper three patterns have been shifted in 2θ to aid comparison between the patterns.*

In order to determine B and its derivative, B', the P-V curve was fitted to various equations of state, using the EoSfit7-GUI program [190]. Due to the pressure discrepancies between DACs with different pressure markers, and since the only

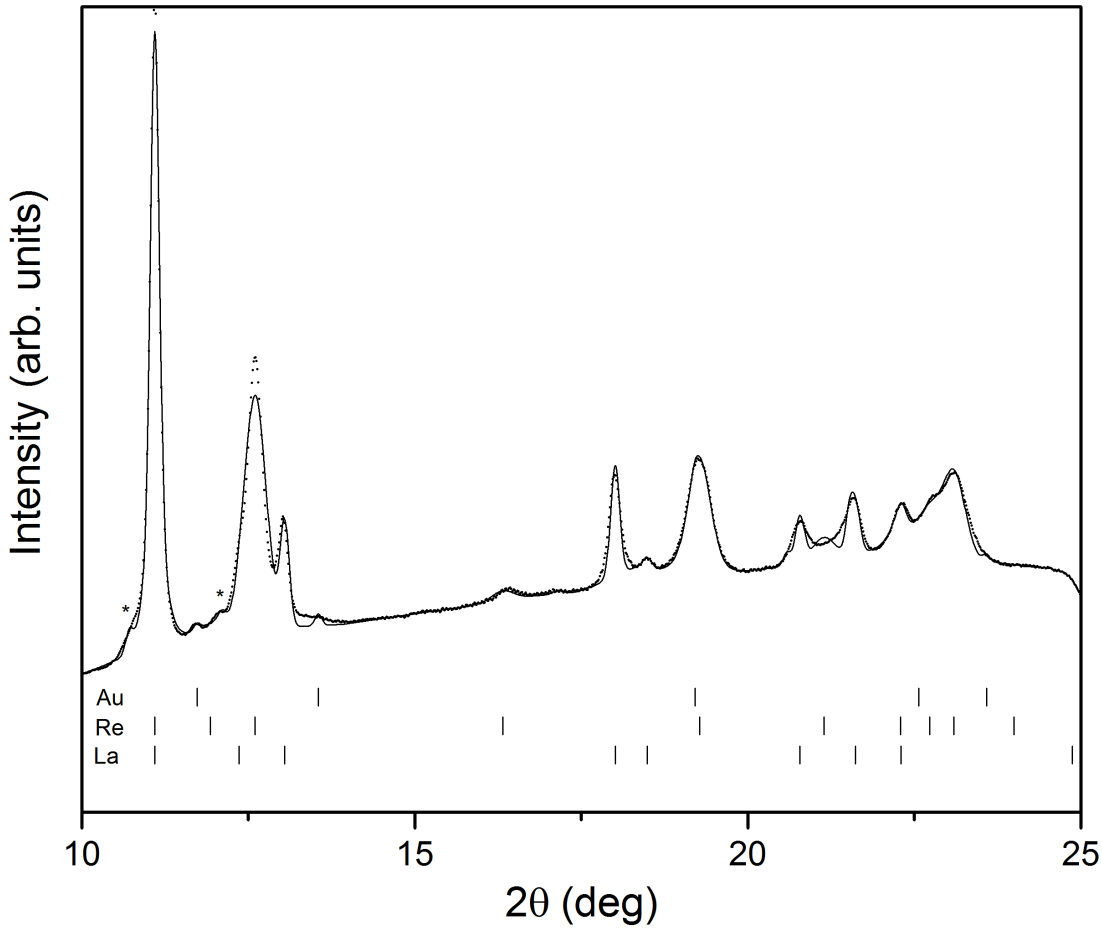

Figure 5.14 *Le Bail refinement of the bct structure to La at 280 GPa, the highest pressure reached, with lattice parameters a = 2.753(5) and c = 3.838(2). The ticks show the calculated positions of the La sample, Re gasket and Au pressure marker peaks, and the asterisks highlight the unknown fcc contaminant peaks, which are still present at this pressure.*

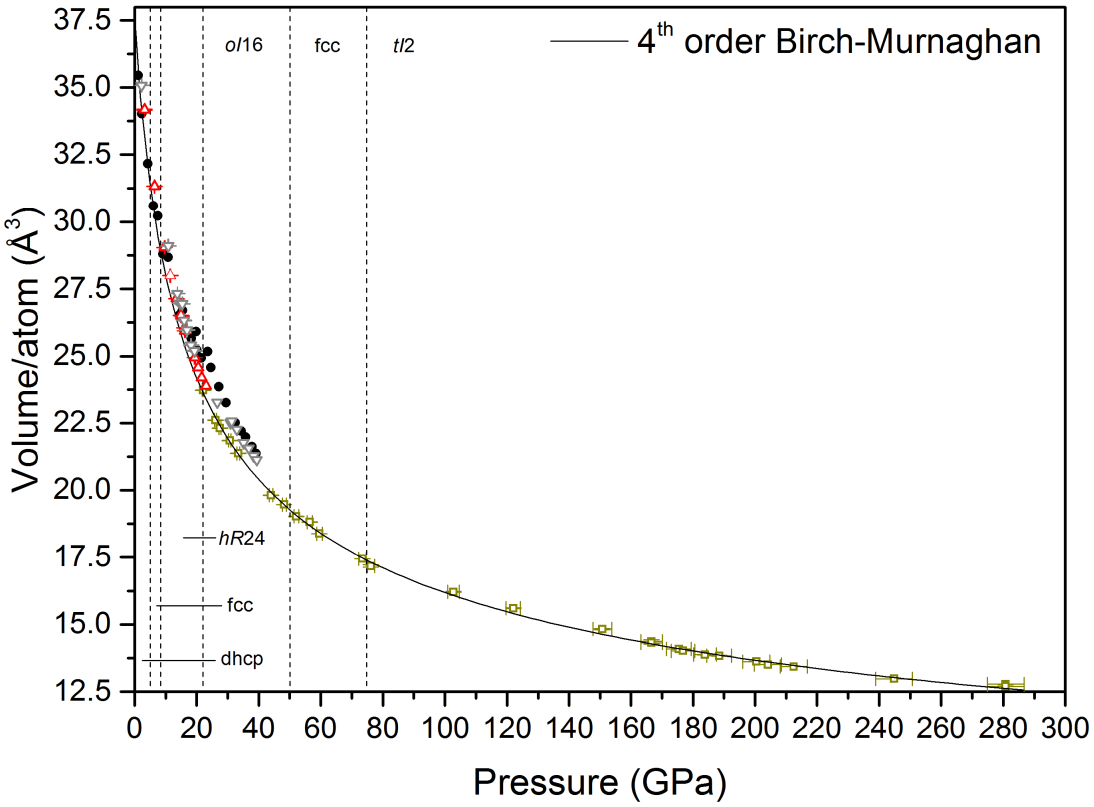

Figure 5.15 *Volume per atom plotted against pressure on ambient temperature La. The solid line is the calculated volume per atom as determined by the 4^{th} order Birch-Murnaghan EoS. The hollow yellow squares are data collected from the HP cell (described in Section 5.2), the upward hollow red triangles were collected from a Ruby DAC, while the downward hollow grey triangles were from a Ta DAC. The solid black circles are data presented by Grosshans et al. [189]. The dashed vertical lines divide the data into the different structures assumed by La. Due to the small culets used in the HP cell, the sample was compressed to 22 GPa upon closing the DAC.*

room temperature data collected from a Au DAC was from the HP cell, only data collected from the HP cell were used to ensure consistancy. V_0 was fixed to the experimental value of 37.35 Å^3 [191], since the refined value of V_0 was much larger than the experimental value, or lead to the fit becoming unstable. All other parameters were refined to obtain the best possible fit. The data best fitted the 4$^{\text{th}}$ order Birch-Murnaghan EoS [47] (See Figure 2.5), with the smallest reduced χ^2, which is given in Equations 2.5 and 2.4 [44]. The refined parameters are B = 21.9(10), $B' = 3.09(16)$ and $B'' =$ -0.060(5), and are lower than all of the previous experimental values, as summarised by Grosshans *et al.* [189]. The entire data set were also fitted to the Vinet and 3$^{\text{rd}}$ order Birch-Murnaghan EoS, but returned un-physically small refined values of B and B' and a larger reduced χ^2, hence they were not used. As seen in Figure 5.15, Grosshans *et al.*'s data diverges from the observed and calculated P-V curve above 8 GPa. However, Grosshans *et al.* did not fit their data to either the $hR24$ or $oI16$ structure, so different observed sample volumes in the d-fcc pressure region is unsurprising. This, combined with the lack of Au DAC data below 20 GPa, explains the different values for B and B'.

5.4 Conclusions

Angle-dispersive x-ray diffraction studies have been performed on La at high pressure and temperature, up to 602 K and 280 GPa. La appears to undergoes the d-fcc($hR24$) $\rightarrow$ d-fcc($oI16$) transition similar to Pr above 22 GPa at 300 K. It is strange that at 377 K La undergoes a fcc $\rightarrow$ d-fcc($oI16$) transformation, bypassing the d-fcc($hR24$) structure altogether. A possible explanation that, due to the textured Debye-Scherrer rings and the failure to observe the full ring resulted in the phase being misidentified. However, both the d-fcc($hR24$) $\rightarrow$ d-fcc($oI16$) and the d-fcc($oI16$) $\rightarrow$ re-entrant fcc phase boundary have been mapped out at temperature.

Data were also collected above 67 GPa for the first time, and La undergoes a peak splitting effect indicating a transformation to a bct structure above 76 GPa, which remains stable up to 280 GPa. These high-pressure data were fitted to a 4$^{\text{th}}$ order Birch-Murnaghan equation of state, and La's bulk modulus and its pressure derivatives were experimentally determined. The calculated P-V curve diverges from data collected by Grosshans *et al.* in the d-fcc region, possibly due to Grosshans *et al.* fitting their data to a different d-fcc structure.

Chapter 6

Gadolinium

6.1 Introduction

As has been described in previous chapters, the crystal structure of the heavier lanthanide metals are much more difficult to study, as all of the high-pressure phases are stable at significantly higher pressures compared to the lighter members of the series. This has led to the collection of lower quality diffraction data, which, in turn, has led to "analysis by analogy", which uses the better data collected on the lighter lanthanide metals at lower pressures to assign structures to the high-pressure phases of the heavier lanthanide metals.

Due to its half-filled $4f$ electron shell, Gd is uniquely placed to act as a bridge between the light and heavy lanthanide metals. Gd crystallises in the hcp structure at ambient conditions, and follows the common trivalent lanthanide transformation sequence (hcp $\rightarrow$ Sm-type $\rightarrow$ dhcp $\rightarrow$ fcc $\rightarrow$ d-fcc $\rightarrow$ "volume collapsed" phase on compression) [15]. The transformation to the d-fcc and "volume collapsed" phases occur at much higher pressures than one would expect from the lanthanide transformation sequence, due to Gd's very stable half-filled $4f$ shell (see Figure 6.1). To further complicate matters, Gd is also one of the most difficult lanthanide metals in which to identify the structure of the d-fcc phase, since the rhombohedral distortion, and hence the splitting of the fcc peaks that accompanies the transition is much smaller compared to other lanthanide metals [11].

While the hcp $\rightarrow$ Sm-type transition in Gd was first observed by Bridgman using

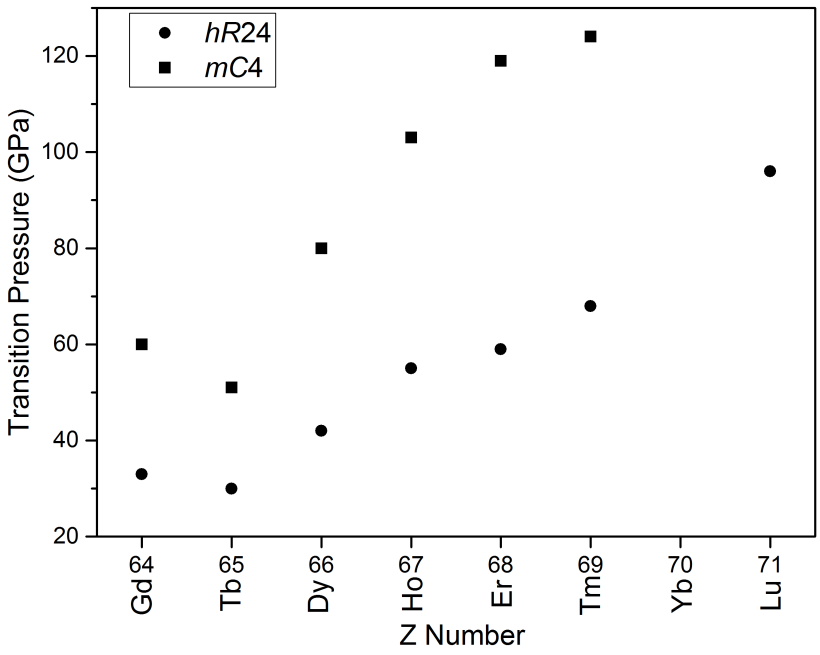

Figure 6.1 *Transition pressures to the d-fcc(hR24) phase and the "volume collapsed"(mC4) phase observed in the heavy lanthanide metals. In Tb though to Lu, the transition pressure decreases at Z decreases, apart from Gd, at which point the transition pressures increases as Z increases (see [15, 96] and the references therein).*

resistivity measurements, the earliest x-ray diffraction study of this transition was performed by Jayaraman *et al.* [192], who also observed additional diffraction peaks at 4 GPa and 400 K, and attributed the new peaks to the appearance of the dhcp phase. McWhan *et al.* observed magnetic changes in Gd at around 5 GPa, signalling the change to the dhcp phase, but did not observe any changes in their x-ray diffraction data at 5 GPa [193]. Benedict *et al.* confirmed that both the Sm-type $\rightarrow$ dhcp and the dhcp $\rightarrow$ fcc transitions are observed in Gd, but determined a very small fcc stability range of $\sim$2.5 GPa [194]. A very thorough high-pressure high-temperature experiment up to $\sim$8 GPa and $\sim$973 K by Hamaya *et al.* mapped out the hcp $\rightarrow$ Sm-type, Sm-type $\rightarrow$ dhcp, hcp $\rightarrow$ dhcp phase boundaries and placed the hcp/Sm-type/dhcp triple point at 6.1 GPa and 873 K [195].

The first x-ray diffraction study to compress Gd above 100 GPa was performed by Akella *et al.* [196], who observed the Sm-type $\rightarrow$ dhcp and dhcp $\rightarrow$ fcc transformations at 6.5 GPa and 24 GPa respectively. The latter transition was found to be very sluggish, with a dhcp/fcc mixed phase region existing from 24-29 GPa. Akella *et al* observed the transformation to the d-fcc phase at 50 GPa,

and assigned a triple hexagonal close packed structure to the new phase, with no measurable volume discontinuity across the transition [196].

The first study to explicitly investigate the structure of Gd's d-fcc phase was performed by Hua *et al.*, who observed the hcp → Sm-type and Sm-type → dhcp transitions at 0.8 and 6 GPa respectively in agreement with previous works [101]. Hua *et al.* did not collect any data between ∼20 and ∼40 GPa and hence, did not detect the fcc phase, but observed a transformation directly to the d-fcc phase from the dhcp phase at 59 GPa [101]. Hua *et al.* confirmed the existence of the new phase above 60 GPa first found by Akella *et al.*, but assigned a body centered monoclinic structure containing 2 atoms, which resulted in a discontinuous 5% volume decrease at the transition pressure [101]. The cause of the sharp volume decrease was attributed to the $4f$ electrons becoming de-localised. However, it should be noted that the calculated density of a structure depends on the structure assignment. The new structure remained stable up to ∼120 GPa, and Hua *et al.* presented a room temperature EoS for Gd. However, they commented that their unrealisticly low value for Gd's bulk modulus was an indication that their structural assignment was incorrect. Beaver *et al.* used image plate and Rietveld refinement techniques to fit their data at 46 GPa to the $hR24$ structure found in Pr. They do not, however, give any transition pressures or an EoS for Gd at high pressure [197].

The most comprehensive high-pressure high-temperature study on Gd was undertaken by Errandonea *et al.* [18], with the aim of resolving the inconsistencies found in previous works. Errandonea *et al* [18]. observed the dhcp → fcc transition at 26 GPa, and the fcc → d-fcc transition at 33 GPa. They also presented a Rietveld refinement of the $hR24$ structure to d-fcc Gd at 39 GPa [18]. Errandonea *et al.* cited the use of a helium PTM as the reason for the large stability region of the fcc structure, and suggested all previous studies without a "soft" PTM were not operating under quasi-hydrostatic conditions. Errandonea *et al.* also observed the transformation to the "volume collapsed" phase beginning at 57 GPa, with the sample fully transformed at 65 GPa. They presented an excellent Rietveld refinement of the $mC4$ structure found in Ce to the d-fcc phase of Gd at 65 GPa, which remains stable up to above 90 GPa. Errandonea *et al.* also performed laser heating experiments on Gd and found that at 39 GPa and 1200 K, Gd undergoes substantial structural changes. In particular the low angle peaks decreased in intensity, and were replaced by several weak peaks. They ruled out a reaction to gadolinium oxide, and attributed the change to a

transformation to a new phase, Gd-IX. Unfortunately, they were unable to assign a crystal structure to this phase due to the unusual peak intensities caused by preferred orientation [18]. The most recent version of the Gd phase diagram is presented in Figure 6.2.

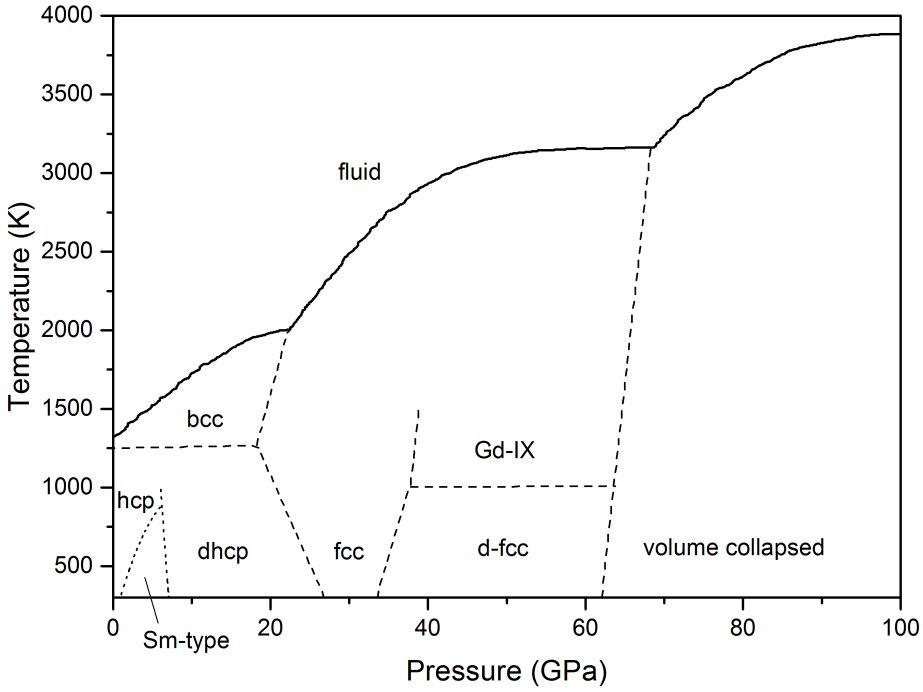

Figure 6.2 *Current phase diagram of Gd. The dotted hcp/Sm-type and Sm-type/dhcp phase boundaries are recreated and extrapolated from Hamaya et al. [195]. The solid melt line is taken from Errandonea et al. [144]. The dashed lines are phase boundaries predicted by Errandonea et al. [18].*

6.2 Outstanding Issues

As stated previously, Gd is reported to have the same d-fcc($hR24$) structure found in the lighter lanthanide metals [14, 15, 197], before it transforms to the "volume collapsed" monoclinic $mC4$ structure, accompanied by a 5% volume decrease at 65 GPa [18]. This behaviour contrasts sharply with what is observed in both Pr and Nd. The former not does adopt the $mC4$ structure, while in the latter there is no reported volume discontinuity at the transformation to the $mC4$ phase. The 5% volume change reported in Gd is also larger compared to other "volume collapse" transitions found in other heavy lanthanide metals [96, 112, 121, 122], and may indicate issues with the structural assignment of the $mC4$ phase.

Tb is a prime example of this, where "analysis by analogy" was used to assign incorrect (hkl) reflections to the various d-fcc peaks [16]. This incorrect structure assignment resulted in a 5% drop in volume across the d-fcc($hR24$) $\rightarrow$ volume collapsed($mC4$) transition [16]. Also, the $mC4$ structure does not fit the "volume collapse" transition phase of Tb, see Figure 6.3. Finally, the structure of Gd-IX currently remains unsolved. These problems were the driving force behind this study of Gd.

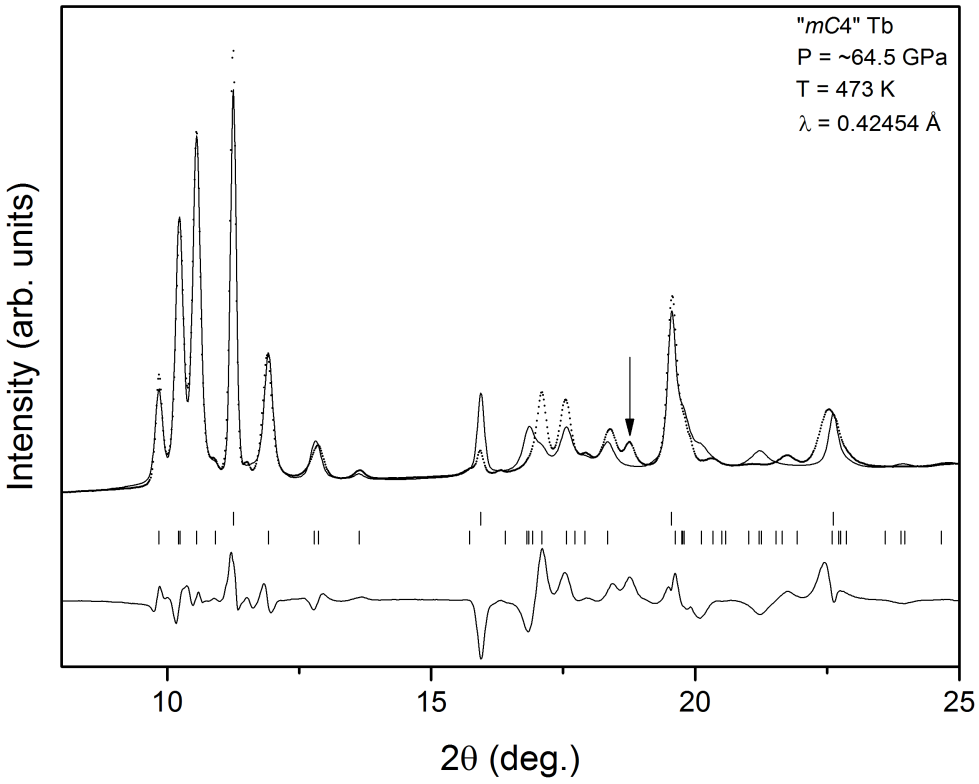

Figure 6.3 *Rietveld refinement of the mC4 structure to an unpublished diffraction pattern from the "volume collapsed" phases found in Tb. The unpublished Tb diffraction data were collected by Dr Rachel Husband on one of her experiments as part of her PhD. As well as the obvious intensity misfits, the downward arrow highlights the single peak which is not predicted by the mC4 structure.*

6.3 Experimental results

Again, in this chapter, all data were collected from samples cut from high purity (99.99+%) Gd ingots, provided by U. Schwarz of the MPI für Chemische Physik fester Stoffe. For room temperature experiments, the samples were loaded into

MB diamond anvil cells equipped with tungsten gaskets and loaded with either a small ($\sim$2 μm) grain of Ta, or a 1 μm thick piece of Ta foil as a pressure calibrant. Again, the cells were loaded in an oxygen free, water free environment (<1 ppm O_2 and <1 ppm H_2O). No pressure transmitting medium was included to prevent sample contamination during loading, and to minimise any chemical reactions occurring within the sample chamber.

The room temperature data were collected during two experiments at the high-pressure beamline I15 at the DLS with a MAR345 detector with incident wavelength of $\sim$0.413 Å. High-pressure high-temperature data were collected at multiple high-pressure beamlines at various synchrotron facilities, beamline P02.2, ID09 and I15 at PETRA III, ESRF and DLS, respectively, using incident x-ray wavelengths of 0.485, 0.412 and 0.425 Å, respectively. In all experiments, the DACs utilized tungsten gaskets. In the high-temperature experiments, heat was applied to the sample as described in Section 2.5. As has been described in previous chapters, the equations of state used to determine pressures are referenced in Section 2.2.2. A single dataset of Dy was collected from a single DAC up to 100 GPa during a Ce experiment at the DLS, with an incident x-ray wavelength of 0.4246 Å. Again, the methods developed by Singh *et al.* were utilized to quantify any non-hydrostatic effects the samples were experiencing [173], and in all cases no non-hydrostatic effects were detected.

6.3.1 Identification of Contaminants

As described in previous chapters, every effort was made to load clean samples, with multiple reloading during experiments. However, trace amounts of contaminants were detected in all samples. While it was possible to avoid the regions of contaminated sample on the beam lines with smaller beam sizes, the contaminants were unavoidable in experiments performed at the DLS and ESRF. Again, two contaminants were identified, each of which could be fitted with the fcc structure. For consistency with previous chapters, the contaminant with the smaller unit cell volume is labelled contaminant 1 and the contaminant with the larger unit cell volume is labelled contaminant 2. An integrated diffraction profile with both contaminants is shown in Figure 6.4, and their high-pressure behaviour is shown in Figure 6.5. Extrapolation of the data to ambient pressure suggests that contaminant 2 is GdH_2, but contaminant 1 was not able to be determined (see Figure 6.5).

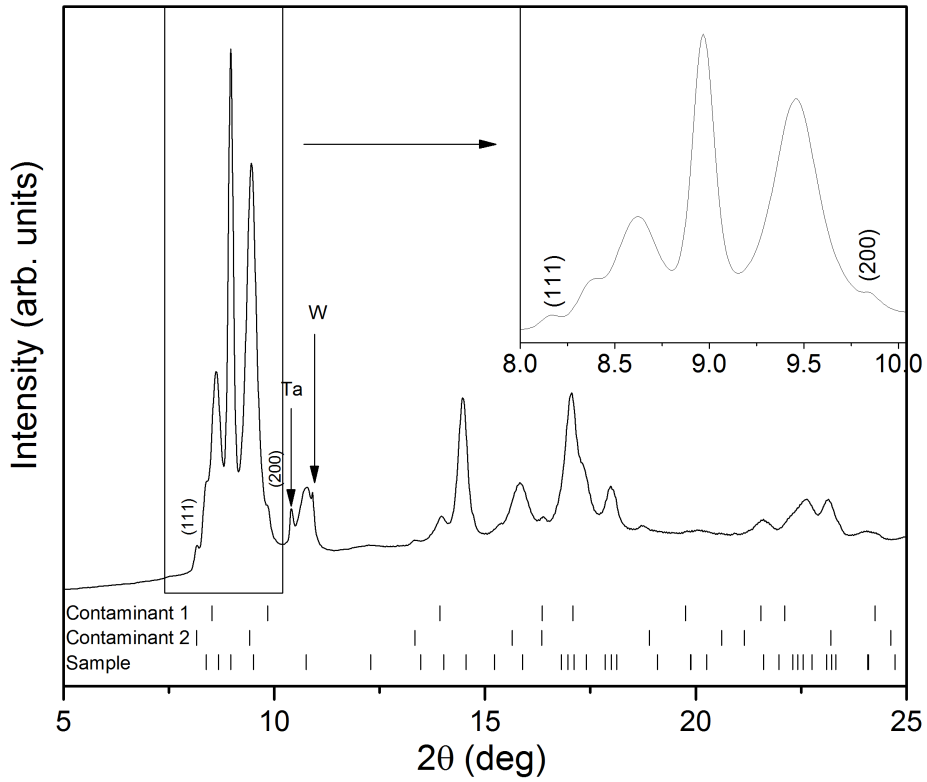

Figure 6.4 *Integrated diffraction pattern of dhcp Gd and both contaminants at ∼17 GPa and 295 K. The tick marks distinguish between the sample and contaminant peaks. The Ta (110) peak and W (110) peak are highlighted with vertical arrows. In the integrated diffraction pattern, the (111) fcc peak of contaminant 2 and the (200) fcc peak of contaminant 1 are labelled. In almost all integrated diffraction patterns only 1 peak from each contaminant was visible. The insert zooms in on the low angle peaks, and emphasizes the two contaminant 1 peaks.*

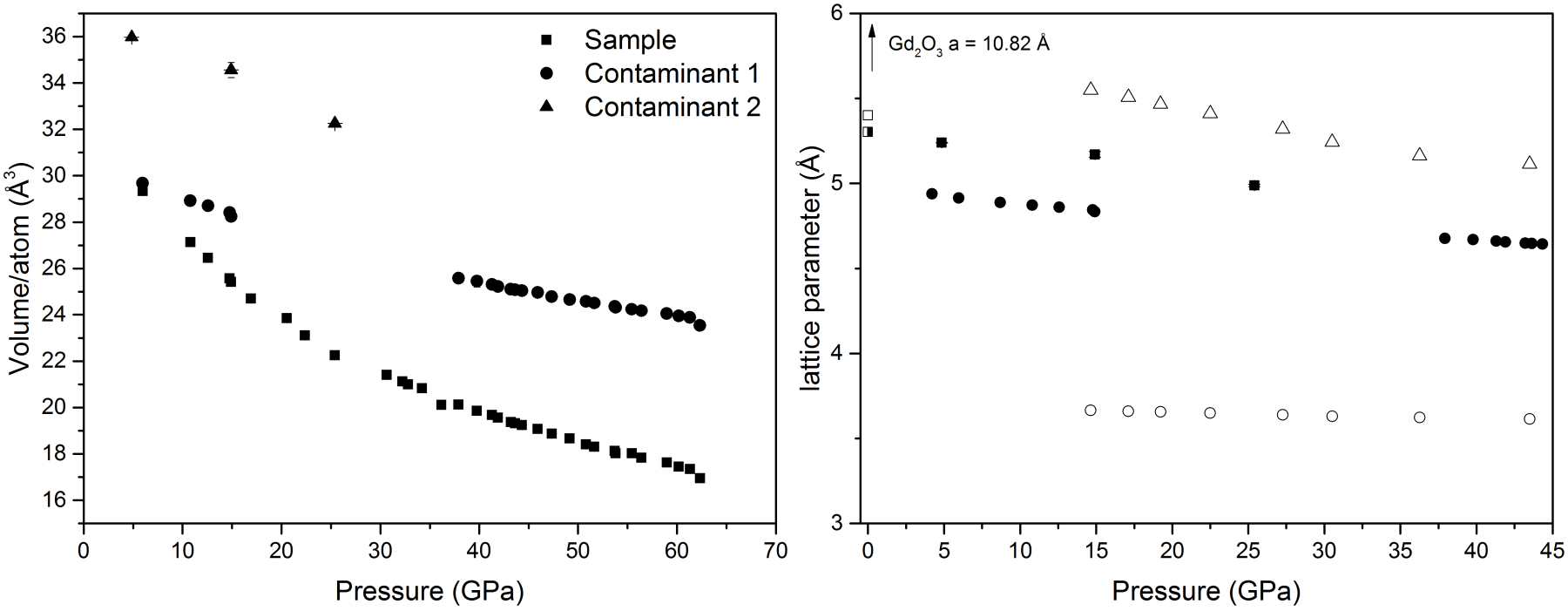

Figure 6.5 *Left: P-V plot of Gd and both contaminants up to 63 GPa. The square data points are from dhcp Gd; the circles are data points from contaminant 1 and the triangles are from contaminant 2. The volume from contaminant 1 was calculated from the (200) peak, the volume from contaminant 2 was calculated from the (111) peak. The sample volume was calculated from either Le Bail or Rietveld refinements. Right: High-pressure behaviour of both contaminants present in most of the Gd samples. The hollow circles and triangles are the a and c lattice parameters of Gd_2O_3 as reported by Zhang et al. [198]. At ambient conditions, Gd_2O_3 adopts a cubic structure, but its lattice parameter is much larger than both contaminants lattice parameter. The hollow square and half filled square are the ambient lattice parameter of cubic GdO and GdH_2 as reported by Semiletov et al. and Wyckoff respectively [199, 200]. The black squares are the lattice parameter of contaminant 2 which are consistent with the ambient lattice parameter of GdH_2.*

6.3.2 The Phase Diagram of Gd

Two data sets were collected on Gd at room temperature. The lowest pressure measured was 0.98 GPa, and, as such, single phase hcp-Gd was not detected, but was always observed alongside the Sm-type phase. The transformation from pure Sm-type to dhcp was detected at 8.9 GPa, with the transformation fully completed by 10.2 GPa. The dhcp phase begins to transform directly into the d-fcc phase at ∼33.6 GPa, by-passing the fcc phase completely, similar to the results reported by Hua *et al.* [101]. The d-fcc phase remains stable up to 62 GPa, the highest pressure reached at room temperature. Throughout the whole stability range of Gd's d-fcc phase, the peak splitting effect is much smaller compared to La. This made it impossible to determine if Gd undergoes the changes in peak intensity indicative of the d-fcc($hR24$) to d-fcc($oI16$) transition, because the (006)/(202) doublet is under-resolved.

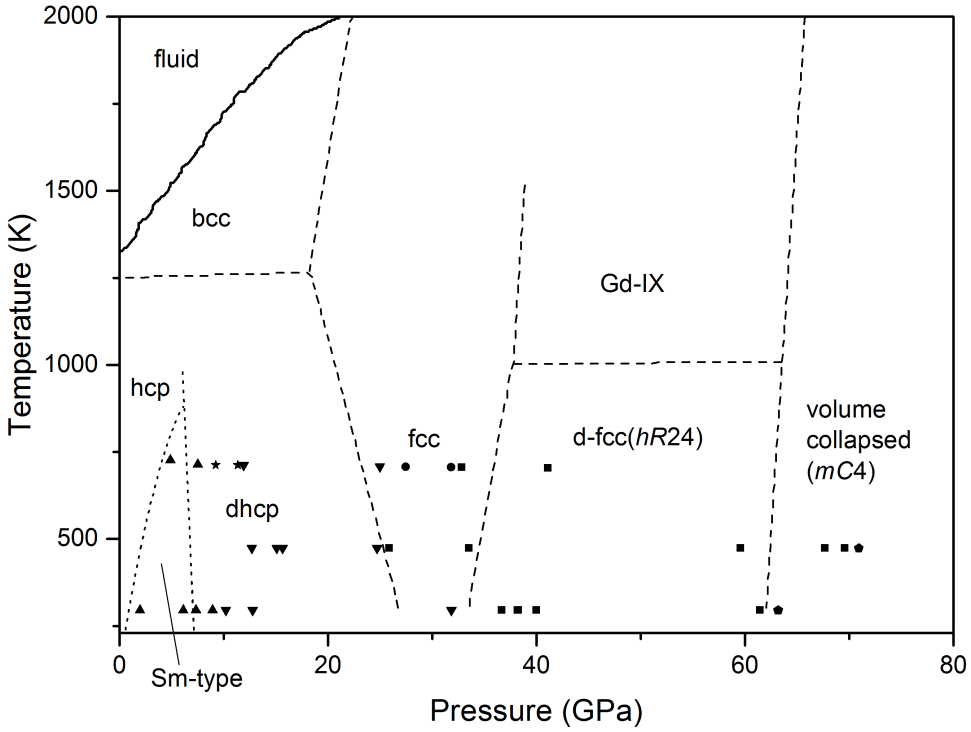

Figure 6.6 *Data points on collected on Gd superimposed on the previously proposed phase diagram in Figure 6.2. Upwards triangles are Sm-type data points, inverse triangles are dhcp data points, circles are fcc data points, squares are d-fcc data points, pentagons indicate the post d-fcc phase and stars highlight mixed phase data points.*

Multiple experiments were performed studying Gd at high pressure and temperature, half of which used a pressure marker. The cells with a Ta marker were

used to create a pressure calculator, so the pressure of the non-marker cells, on which most the structural analysis was performed, could be determined. No marker was included to ensure that none of the weakly split sample peaks were overlapped with a non-sample peak. The samples were heated to the required temperature and then iso-thermally compressed. The combined results of the room temperature and high temperature experiments are shown in Figure 6.6.

Firstly, the Sm-type $\rightarrow$ dhcp transition seem to occur at higher pressures than what has been reported in the literature [101, 196]. Another interesting feature of the phase diagram is that below 473 K, Gd does not adopt the fcc phase, instead transforming directly into the d-fcc phase. Conversely, at 703 K, Gd transforms from the dhcp phase into the fcc phase at 27 GPa, which remains stable until 31.8 GPa when Gd transforms into the d-fcc phase. Due to the presence of contaminants, determining the structure of Gd's d-fcc phase proved challenging.

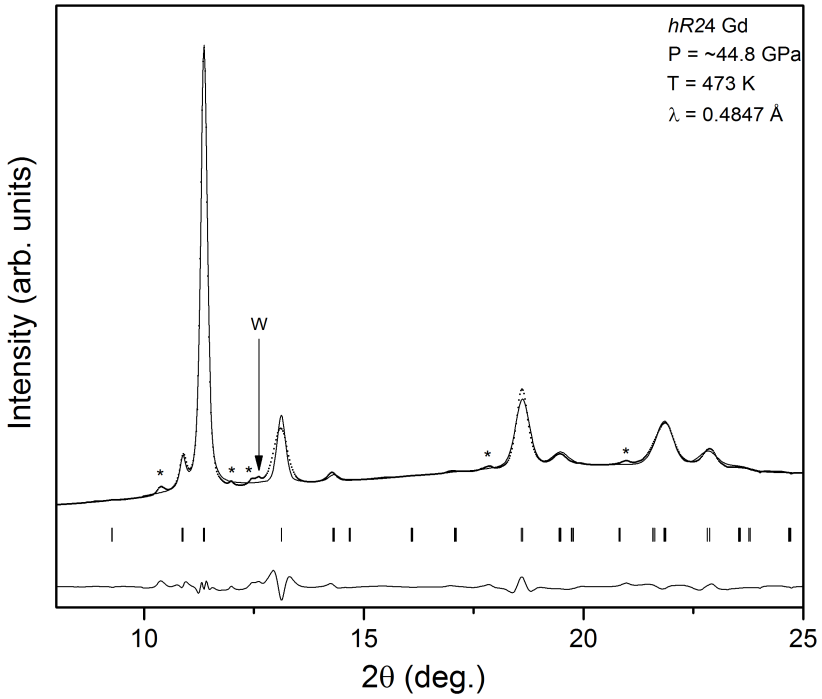

Figure 6.7 *Rietveld refinement of the hR24 structure to an integrated diffraction pattern from Gd at ∼44.5 GPa. The dots are data points while the solid black line is the calculated intensity of the fit. The tick marks indicate the position of the calculated peaks. The asterisks highlight the contaminant peaks discussed in Section 6.3.1. The (110) peak of the W gasket is also indicated.*

While the $hP6$ and $oC8$ structures appear to fit the integrated diffraction pattern, both of the proposed structures have super-lattice reflections overlapping with the

contaminant 2 (113) peak, but none of the other observed contaminant peaks. Regardless of the structure selected, it was always necessary to include both contaminants to account for all of the observed peaks. Furthermore, the absence of the predicted $hP6$ (103) peak in the diffraction pattern ruled out the $hP6$ structure, while a number of small misfits rule out the $oC8$ structure. All of the observable peaks can be accounted for by the $hR24$ structure (see Figure 6.7) and the two contaminants with minimal overlap between the three structures' diffraction profiles. There was also no evidence of a transformation to the $oI16$ phase found in Pr and La, since the (006)/(202) doublet was not resolved at any pressure (see Figure 6.8). There was also no indication of a transformation to Gd-IX, indicating that the phase boundary is higher than 700 K, but lower than $\sim$1200 K.

Finally, data were also collected on the "volume collapsed" phase at both room temperature and 473 K. Attempts were made to fit the data to the $mC4$ structure using lattice parameters suggested by various previous studies [16, 18, 96, 112, 122, 124], with the best fit shown in Figure 6.9. As can be seen in Figure 6.9 there is a single peak which is not predicted by the $mC4$ structure. For comparison, the $mC4$ structure has been fitted to the "volume collapsed" phase found in both Tb and Dy (see Figure 6.9), and it appears that all 3 heavy lanthanide adopt the same structure, which can not be fitted to the $mC4$ structure.

Extensive attempts were made to index both all, and subgroups of, the observed peaks to hexagonal, orthorhombic and monoclinic unit cells, using the powder indexing software DICVOL [201]. Each unit cell was searched for separately, over volume ranges of 100 Å^3 (0-100 Å^3, 100-200 Å^3 etc) up to 500 Å^3. The ratios of all of the observed peaks were also calculated to determine if a set of observed peaks could be assigned the ($hk0$) set of reflections from a hexagonal structure. Once the set of observed peaks were assigned to the various ($hk0$) reflections, the c lattice parameter was chosen to systematically fit an (hkl) reflection to the remaining low angle, intense peaks. The resulting structures failed to account for a large number of observed peaks in the integrated diffraction pattern. Constructing larger supercells resulted in more of the observed peaks being accounted for, but significant misfits remained. Despite exhaustive effort, the structure of the "volume collapsed" phase of Gd and its neighbours Tb and Dy, remains unsolved. One possibility is that the structure is incommensurate, similar to divalent Eu [202]. If true, then in order to solve the structure successfully, the parent and satellite reflections would have to be correctly identified, which is

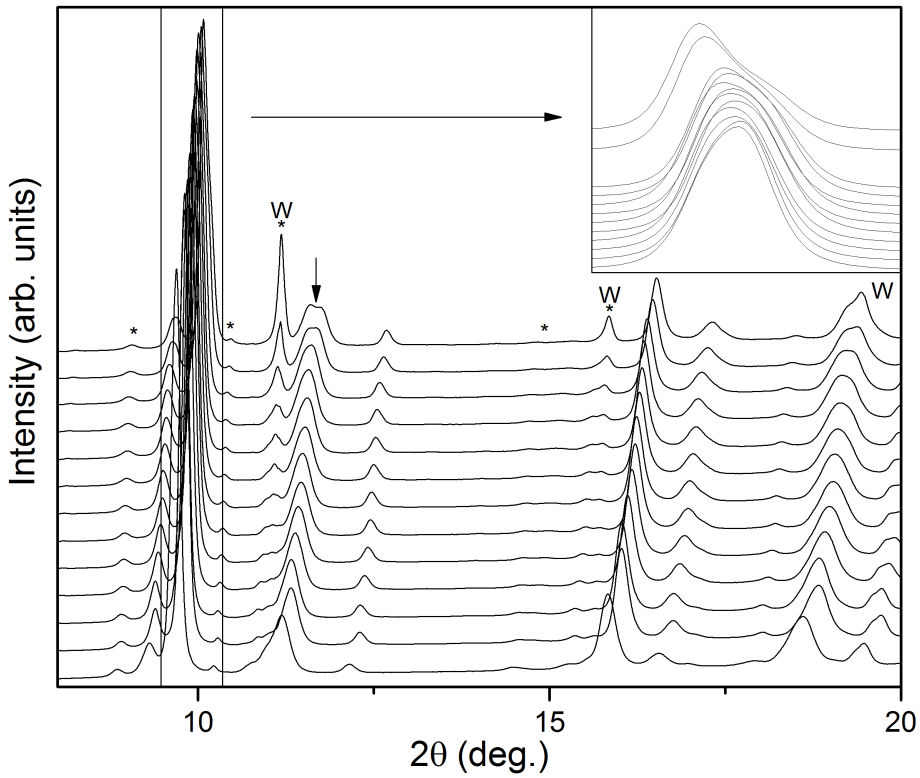

Figure 6.8 *Waterfall plot of diffraction profiles from the d-fcc phase of Gd upon compression from ∼43 GPa to ∼68 GPa. There is very little change in the sample's peaks on compression, with no extra peaks appearing or any obvious change in intensity until the transformation to the "volume collapsed" phase. The W gasket peaks are also highlighted, and the asterisks indicate contaminant peaks. The insert highlights the behaviour of the under-resolved d-fcc(hR24) (006)/(202) doublet as pressure increases, and demonstrates the difficultly of distinguishing between the various proposed structure for the d-fcc phase; the (006)/(202) doublet in the insert has been shifted in 2θ to aid comparison. The insert also highlights the emergence of the mC4 (-111) peak in the 2^{nd} integrated diffraction pattern from the top from the d-fcc(hR24) (006)/(202) doublet. The arrow in the main plot highlights the emergence of the mC4 (111) peak.*

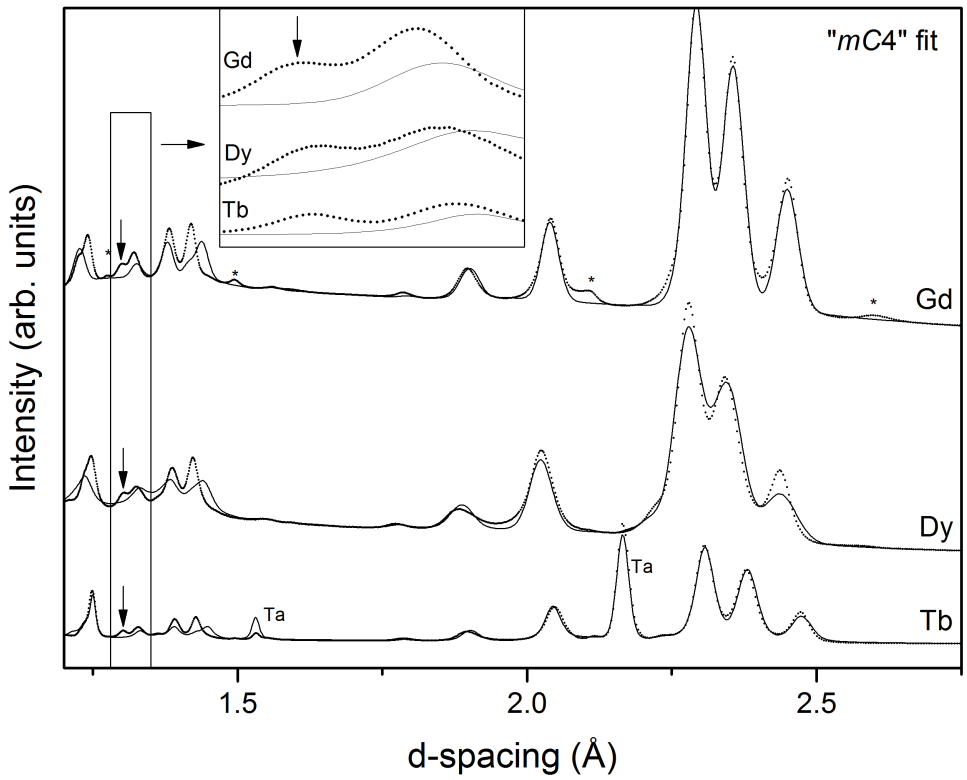

Figure 6.9 *Rietveld refinements of the mC4 structure to diffraction patterns from the "volume collapsed" phases found in Gd, Tb and Dy at 74.8 GPa, 64.5 GPa and 75.2 GPa respectively, and 473 K, 300 K and 300 K respectively. The downward arrow highlights the single peak which is not predicted by the mC4 structure. The asterisks show the contaminant peaks. The Ta peaks are also labelled. The integrated diffraction patterns have been shifted in d-spacing to aid comparison. The refined lattice parameters of Gd are a = 4.862(4), b = 2.859(3), c = 4.67(2), β = 105.56(19) with Wyckoff position 4i (x, 0, z) where x = 0.310(4), z = 0.263(7). The refined lattice parameters of Tb are a = 4.941(5), b = 2.897(4), c = 4.65(2), β = 105.8(2). The Wyckoff positions are 4i (x, 0, z), with x = 0.3071(8), z = 0.252(2). The unpublished Tb diffraction data were collected by Dr Rachel Husband on one of her experiments as part of her PhD. The refined parameters of Dy are a = 4.808(6), b = 2.807(5), c = 4.55(2), β = 106.122(12). The Wyckoff positions are 4i (x, 0, z), with x = 0.3041(8), z = 0.255(2).*

almost impossible from a 1-D powder diffraction pattern. A single crystal of the 'volume collapsed" phase would be needed in-order to solve an incommensurate structure, but it is extremely difficult to reliably grow a single crystal of a metal at such extreme conditions.

6.4 Conclusions

Angle dispersive x-ray powder diffraction experiments have been performed on Gd up to 100 GPa and 700 K, examining Gd's high-pressure structures. While the d-fcc $\rightarrow$ "volume collapsed" phase transition at room temperature is in agreement with previous works, there are small disagreements with all other transition pressures. A transition to the Gd-IX phase was not observed, suggesting the phase is only stable above 700 K. Gd doesn't appear to undergo a transformation to the d-fcc($oI16$) phase found in La and Pr, but the data does not resolve the d-fcc($hR24$) (006)/(202) doublet, making structural determination very challenging. The structure Gd and its neighbours adopt in the "volume collapsed" phase are all very similar to each other, with further work being required to determine the structure the heavy lanthanide metals adopt at high pressures.

Chapter 7

Conclusions and Future Work

The previous chapters present the high-pressure high-temperature behaviour of three lanthanide metals: Ce, La and Gd. Ce has received the bulk of attention compared to the other two, and its phase diagram has been mapped out at temperature. Ce is known to adopt either the $oC4$ or the $mC4$ structure at high pressure, but all of the previous resistivity experiments which mapped out the phase diagram do not distinguish which phase boundary was being measured. To further complicate matters, there is no evidence to suggest that the $oC4$ and $mC4$ phase boundaries are interchangeable. During an isothermal compression at temperature, Ce underwent the transformation sequence fcc(α) $\rightarrow$ bct $\rightarrow$ d-fcc($oC4$) $\rightarrow$ bct which contradicts the previously accepted phase boundary. A systematic study of Ce's various phase boundaries was undertaken to resolve these issues.

The results in this thesis suggest a different phase boundary for Ce compared to previous work upon pressure and temperature increases. The fcc(α) $\rightarrow$ d-fcc($oC4$) phase boundary is very steep, but rapidly flattens as the fcc(α)/d-fcc($oC4$)/bct triple point is approached. The boundary remains very gradual until $\sim$12 GPa then rapidly becomes very steep and has a negative gradient. This contrasts with previous phase diagrams, which suggests a much more gradual d-fcc($oC4$) $\rightarrow$ bct slope. There are also very striking differences regarding the d-fcc($oC4$) $\rightarrow$ bct transition pressure between experiments at temperature. In particular, at 373 K and 600 K, where there is a 4 GPa discrepancy between different samples. The fcc(α) $\rightarrow$ bct transition at temperature was also studied, and was found to have a positive gradient and is a first order transition at 643 K.

La, by comparison has received very little attention. At 76 GPa, three out of five observable fcc reflections, the (200) (220) and (311), become asymmetric and begin to split into doublets, while the (111) and (222) peaks remain singlets. This splitting suggests the fcc phase found at 60 GPa transforms into the $tI2$ structure. In order for a full Rietveld refinement treatment of La above 76 GPa to be successful, better quality x-ray diffraction data and a much smaller beam size to avoid gasket contamination would be required. The high-pressure beamline P02.2 at PETRA-III would be ideal, due to their ability to obtain a small beam size. Furthermore, the structure of La's d-fcc phase had not been studied in great detail previously using Rietveld refinement techniques. Changes in various peak intensities at around 22 GPa and 300 K suggests that La undergoes a transformation from the d-fcc($hR24$) structure to the d-fcc($oI16$) structure. The d-fcc phase's stability region at temperature was also mapped out, and the d-fcc($hR24$) $\rightarrow$ d-fcc($oI16$) phase boundary was determined. Since identifying the d-fcc($hR24$) $\rightarrow$ d-fcc($oI16$) phase transition requires observing peak intensity changes, it is necessary to observe the full Debye-Scherrer ring. Therefore, future experiments exploring the d-fcc phase of the lanthanide metals require a backing disc with a full conical opening.

It has proved much more difficult to determine if Gd under goes a similar transformation, due to the peak splitting effect in Gd being almost non-existent compared to La, and the constant presence of contaminants. There is no evidence of the intensity changes indicating a transformation to the d-fcc($oI16$) phase found in other lanthanide metals. This work has shown that the accepted structure of the "volume collapsed" phase found in Gd in incorrect, but despite considerable effort, the structure remains unsolved. If the "volume collapsed" phase is incommensurate, then the structure would prove almost impossible to solve using powder x-ray diffraction. Further work will be required in order to correctly determine the "volume collapsed" phase's structure. Attempts were made to reach the Gd-IX phase reported by Errandonea *et al.* [18], but sufficiently high temperatures could not be reached, putting the lower temperature boundary between 703 and 1100 K. It is apparent that the ability to obtain high quality x-ray diffraction data from samples at high pressure and temperatures up to and beyond 1000 K is vital. In order to determine the structure of this currently unsolved phase, further work is required to improve the heating vessel's capabilities to reach higher temperatures.

With that goal in mind, towards the end of my studies, heaters were developed

in collaboration with Simon MacLeod from AWE to extend the vacuum vessel's capabilities to obtain and accurately measure the temperature of compressed samples. Since a vacuum vessel needs to be utilized to protect the diamonds from oxidation at high temperatures, the usable apparatus is restricted by the available space inside the heating vessel. An external heater is an accurate and reliable method to apply temperature, but it is very difficult to extend the temperature range. While laser heating is capable of heating samples from 500 K to over 4000 K the temperature uncertainty is very large, and is more pronounced at lower temperatures [203]. An wire heater is a comparatively small device that can easily fit inside the vacuum vessel. I built and tested several wire heaters with the intention to extend the maximum temperature range that can be reached within the vessel.

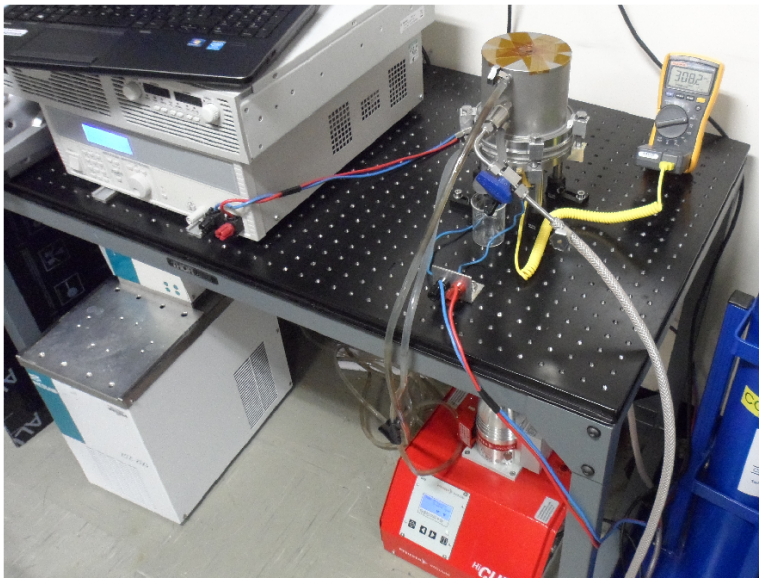

Figure 7.1 *Image of the equipment set up used to test the various heaters. The heaters attached to the tungsten carbide discs were attached to a piston cell described in Section 2.1. The cell was then loaded into a vacuum vessel as described in Section 2.5 to measure the maximum temperature achievable.*

0.42 mm thick Kanthal wire and 0.25 mm thick Clapton wire were glued onto ceramic rings using thermal cement, either using Resbond 903 or Resbond 901. The cement electrically insulated the seat from the wire, and also served as the thermal conductor. A new development was to shield the thermal-couple wires with ceramic beads, to prevent the two different wires from touching causing the temperature measurement to fluctuate, and to protect the other components of the set up. When the vessel was sealed and a vacuum applied, temperatures

of 1462 K were reached, which was the upper limit on what the thermal couple could measure. This wire heater can be incorporated into the heating vessel with the addition of another copper wire feed-through in the front flange. This would enable much more heat to be applied to the sample within the vacuum vessel than was possible previously, and push the boundaries of available P-T space to explore.

Appendix A

List of Distorted-fcc Structures

This appendix contains a list of the d-fcc structures studied in this thesis.

Structure	Spacegroup	a (Å)	b (Å)	c (Å)	α	β	γ
$hP3(1)$	$P3_1$	3.1777(2)	3.1777(2)	7.9429(6)	90	90	120
$hP3(2)$	$P3_2$	3.1777(2)	3.1777(2)	7.9429(6)	90	90	120
$hP6$	$P3_121$	3.1788(3)	3.1788(3)	15.887(2)	90	90	120
$hR24$	$R\bar{3}m$	6.3561(4)	6.3561(4)	15.8861(10)	90	90	120
$oC8(1)$	$Cmmm$	8.538(12)	5.982(5)	2.965(8)	90	90	90
$oC8(2)$	$Cmma$	8.553(6)	5.963(9)	2.987(3)	90	90	90
$oI16$	$Ibam$	9.1170(12)	6.4495(7)	6.3357(9)	90	90	90
$oP16$	$Pmmm$	6.4895(4)	6.3168(3)	9.1527(7)	90	90	90
$mC4$	$C2/m$	5.6083(6)	3.1636(3)	5.579(2)	90	109.21(2)	90
$mI4$	$I2/m$	5.6177(2)	3.15976(11)	5.5619(3)	90	109.309(5)	90
$mP4$	$P2/m$	5.6094(6)	3.1633(3)	5.579(2)	90	109.234(13)	90
$mC16$	$C2/m$	11.0262(12)	6.5361(12)	6.3824(16)	90	124.876(11)	90
$oC4$	$Cmcm$	2.9567(3)	5.8008(3)	5.085(4)	90	90	90
$tI2$	$I4/mmm$	3.1832(10)	3.1832(10)	4.7621(3)	90	90	90

Table A.1 *Table of d-fcc structures studied in this thesis, with sample lattice parameters and corresponding spacegroups. More information is contained in Table A.2.*

Structure	Wyckoff Positions	Atomic Coordinates	P (GPa)	T (K)	Lanthanide
$hP3(1)$		Rietveld not performed	21	293	La
$hP3(2)$		Rietveld not performed	21	293	La
$hP6$	*6c*	(0.402(3), 0.380(4), 0.7452(6))	21	293	La
$hR24$	*6c* *18h*	(0, 0, 0.269(2)) (0.5066(10), -0.5066(10), 0.243(2))	21	293	La
$oC8(1)$	*4g* *4j*	(0.233(3), 0, 0) (0, 0.290(5), 0.5)	26.2	293	Gd
$oC8(2)$	*4g* *4a*	(0, 0.25, 0.561(3)) (0.25, 0, 0)	26.2	293	Gd
$oI16$	*8g* *8j*	(0, 0.237(2), 0.25) 0.263(2), 0.0342(14), 0)	25.9	412.3	La
$oP16$		Rietveld not performed	21	293	La
$mC4$	*4i*	(0.2699(9), 0, 0.237(2))	21	293	La
$mI4$		Rietveld not performed	21	293	La
$mP4$	*2m* *2n*	(0.732(2), 0, 0.737(2)) (0.231(4), 0.5, 0.737(2))	21	293	La
$mC16$	$4i_1$ $4i_2$ *8j*	(0.25(2), 0, 0.80(2)) (0.26(2) ,0 ,0.25(2)) (0.004(8), 0.775(8), 0.26(2))	21	293	La
$oC4$		Rietveld not performed	12.6	293	Ce
$tI2$		Rietveld not performed	7.9	602	Ce

Table A.2 *Table of d-fcc structures studied in this thesis, with corresponding Wyckoff positions, sample atomic coordinates, sample pressures, sample temperatures and the lanthanide from which the sample values are drawn from. In some cases, no Rietveld refinement was performed since it was clear from the Le Bail refinement that the structure did not fit the diffraction profile. More information is contained in Table A.1.*

Bibliography

[1] M. I. McMahon and R. J. Nelmes. High-pressure structures and phase transformations in elemental metals. *Chemical Society Reviews*, 35:943–963, 2006.

[2] M. Oganov A. R. Xie Y. Trojan I. Medvedev S. Lyakhov A. O. Valle M. Ma, Y. Eremets and V. Prakapenka. Transparent dense sodium. *Nature*, 458:182–185, 2009.

[3] H. Luo, S. Desgreniers, Y. K. Vohra, and A. L. Ruoff. High-pressure optical studies on sulfur to 121 GPa: Optical evidence for metallization. *Physical Review Letters*, 67:2998–3001, 1991.

[4] J. F. Lin, D. L. Heinz, H. Mao, R.l J. Hemley, J. M. Devine, J. Li, and G. Shen. Stability of magnesiowüstite in Earth's lower mantle. *Proceedings of the National Academy of Sciences*, 100(8):4405–4408, 2003.

[5] K. Kurpiewska and Krzysztof L. High pressure macromolecular crystallography for structural biology: a review. *Open Life Sciences*, 5:531–542, 2010.

[6] A. L. Ruoff, H. Xia, H. Luo, and Y. K. Vohra. Miniaturization techniques for obtaining static pressures comparable to the pressure at the center of the earth: X–ray diffraction at 416 GPa. *Review of Scientific Instruments*, 61(12):3830–3833, 1990.

[7] N. Dubrovinskaia, L. Dubrovinsky, N. A. Solopova, A. Abakumov, S. Turner, M. Hanfland, E. Bykova, M. Bykov, C. Prescher, V. B. Prakapenka, S. Petitgirard, I. Chuvashova, B. Gasharova, Y. L. Mathis, P. Ershov, I. Snigireva, and A. Snigirev. Terapascal static pressure generation with ultrahigh yield strength nanodiamond. *Science Advances*, 2(7), 2016.

[8] M. I. McMahon. *High Pressure Diffraction from Good Powders, Poor Powders and Poor Single Crystals*, pages 1–20. Springer Netherlands, Dordrecht, 2004.

[9] R. J. Nelmes and M. I. McMahon. High-Pressure Powder Diffraction on Synchrotron Sources. *Journal of Synchrotron Radiation*, 1(1):69–73, 1994.

[10] D. A. Young. *Phase diagrams of the elements*. Berkeley: University of California Press, 1991.

[11] T. Krüger, B. Merkau, W. A. Grosshans, and W. B. Holzapfel. Kinetics and systematics of structural phase transitions in the regular lanthanide metals under pressure. *High Pressure Research*, 2(4):193–236, 1990.

[12] R. J. Nelmes, P. D. Hatton, M. I. McMahon, R. O. Piltz, J. Crain, R. J. Cernik, and G. Bushnell-Wye. Angle-dispersive powder-diffraction techniques for crystal structure refinement at high pressure. *Review of Scientific Instruments*, 63(1):1039–1042, 1992.

[13] O. Shimomura, K. Takemura, H. Fujihisa, Y. Fujii, Y. Ohishi, T. Kikegawa, Y. Amemiya, and T. Matsushita. Application of an imaging plate to high-pressure x-ray study with a diamond anvil cell (invited). *Review of Scientific Instruments*, 63(1), 1992.

[14] N. Hamaya, Y. Sakamoto, H. Fujihisa, Y. Fujii, K. Takemura, T. Kikegawa, and O. Shimomura. Crystal structure of the distorted FCC high-pressure phase of praseodymium. *Journal of Physics: Condensed Matter*, 5(31):L369, 1993.

[15] G. K. Samudrala and Y. K. Vohra. Chapter 257 - Structural Properties of Lanthanides at Ultra High Pressure. In Jean-Claude G. Bnzli and Vitalij K. Pecharsky, editors, *Including Actinides*, volume 43 of *Handbook on the Physics and Chemistry of Rare Earths*, pages 275 – 319. Elsevier, 2013.

[16] N. C. Cunningham, W. Qiu, K. M. Hope, H. P. Liermann, and Y. K. Vohra. Symmetry lowering under high pressure: Structural evidence for f-shell delocalization in heavy rare earth metal terbium. *Physical Review B*, 76:212101, 2007.

[17] B. J. Baer, H. Cynn, V. Iota, C.S. Yoo, and G. Shen. Phase diagram and equation of state of praseodymium at high pressures and temperatures. *Physical Review B*, 67:134115, 2003.

[18] D. Errandonea, R. Boehler, B. Schwager, and M. Mezouar. Structural studies of gadolinium at high pressure and temperature. *Physical Review B*, 75:014103, 2007.

[19] C.E. Weir, E.R. Lippincott, A. Vanvalkenburg, and E.N. Bunting. Infrared studies in the 1- to 15-micron region to 30,000 atmospheres. *Journal of Research of the National Bureau of Standards Section A-Physics and Chemistry*, 63:55–62, 1959.

[20] J. C. Jamieson, A. W. Lawson, and N. D. Nachtrieb. New Device for Obtaining X-Ray Diffraction Patterns from Substances Exposed to High Pressure. *Review of Scientific Instruments*, 30(11):1016–1019, 1959.

[21] L. Merrill and W. A. Bassett. Miniature diamond anvil pressure cell for single crystal x-ray diffraction studies. *Review of Scientific Instruments*, 45(2):290–294, 1974.

[22] R. Boehler and K. De Hantsetters. New anvil designs in diamond-cells. *High Pressure Research*, 24(3):391–396, 2004.

[23] S. A. Moggach, D. R. Allan, S. Parsons, and J. E. Warren. Incorporation of a new design of backing seat and anvil in a Merrill-Bassett diamond anvil cell. *Journal of Applied Crystallography*, 41(2):249–251, 2008.

[24] Z. Jenei, H. Cynn, K. Visbeck, and W. J. Evans. High-temperature experiments using a resistively heated high-pressure membrane diamond anvil cell. *Review of Scientific Instruments*, 84(9), 2013.

[25] D. M. Adams and A. C. Shaw. A computer-aided design study of the behaviour of diamond anvils under stress. *Journal of Physics D: Applied Physics*, 15(9):1609, 1982.

[26] H. K. Mao and P. M. Bell. Generation of Static Pressures to 1.5 Mbar. *Year book - Carnegie Institution of Washington*, 76:644 – 658, 1976-1977.

[27] C. M. Sung, C. Goetze, and H. K. Mao. Pressure distribution in the diamond anvil press and the shear strengh of fayalite. *Review of Scientific Instruments*, 48(11):1386–1391, 1977.

[28] M. S. Bruno and K. J. Dunn. Stress analysis of a beveled diamond anvil. *Review of Scientific Instruments*, 55(6):940–943, 1984.

[29] H. K. Mao, P. M. Bell, J. W. Shaner, and D. J. Steinberg. Specific volume measurements of Cu, Mo, Pd, and Ag and calibration of the ruby R1 fluorescence pressure gauge from 0.06 to 1 Mbar. *Journal of Applied Physics*, 49(6):3276–3283, 1978.

[30] T. H. Maiman. Stimulated Optical Radiation in Ruby. *Nature*, 187:493–494, 1960.

[31] R. A. Forman, G. J. Piermarini, J. D. Barnett, and S. Block. Pressure Measurement Made by the Utilization of Ruby Sharp-Line Luminescence. *Science*, 176(4032):284–285, 1972.

[32] J. D. Barnett, S. Block, and G. J. Piermarini. An Optical Fluorescence System for Quantitative Pressure Measurement in the Diamond Anvil Cell. *Review of Scientific Instruments*, 44(1):1–9, 1973.

[33] G. J. Piermarini, S. Block, J. D. Barnett, and R. A. Forman. Calibration of the pressure dependence of the R1 ruby fluorescence line to 195 kbar. *Journal of Applied Physics*, 46(6):2774–2780, 1975.

[34] K. Syassen. Ruby under pressure. *High Pressure Research*, 28(2):75–126, 2008.

[35] D. L. Decker. Equation of State of NaCl and its use as a Pressure Gauge in High Pressure Research. *Journal of Applied Physics*, 36(1):157–161, 1965.

[36] M. Hanfland, K. Syassen, and J. Köhler. Pressure-volume relationship of Ta. *Journal of Applied Physics*, 91(7), 2002.

[37] P. I. Dorogokupets and A. R. Oganov. Ruby, metals, and MgO as alternative pressure scales: A semiempirical description of shock-wave, ultrasonic, x-ray, and thermochemical data at high temperatures and pressures. *Physical Review B*, 75:024115, 2007.

[38] C. R. Bishop and M. Stern. A Method for Prevention of Hydrogen Embrittlement of Tantalum in Aqueous Media. *CORROSION*, 17(8):379t–385t, 1961.

[39] Z. Li, Y. Cheng, X Chen, T. Wang, D. Shi, Z. Tong, Y. Yan, X. Tian, and Z. Zhao. High-Purity Tantalum Powder and Preparation Method Thereof, Dec 2016.

[40] M. Taxak, S. Kumar, N. Krishnamurthy, A. K. Suri, G. P. Tiwari. Change in lattice parameter of tantalum due to dissolved hydrogen. *Processing and Application of Ceramics*, 6:73–76, 2012.

[41] M. Yokoo, N. Kawai, K. G. Nakamura, K. Kondo, Y. Tange, and T. Tsuchiya. Ultrahigh-pressure scales for gold and platinum at pressures up to 550 GPa. *Physical Review B*, 80:104114, 2009.

[42] H. Cynn, B. J. Baer, S. G. MacLeod, W. J. Evans, M. J. Lipp, J. P. Klepeis, Z. Jenei, J. Y. Chen, K. Catalli, D. Popov, and C. Y. Park. Comparison of the existing internally consistent pressure scales at high pressures and high temperatures. In *APS Meeting Abstracts*, 2012.

[43] P. I. Dorogokupets and A. Dewaele. Equations of state of MgO, Au, Pt, NaCl-B1, and NaCl-B2: Internally consistent high-temperature pressure scales. *High Pressure Research*, 27(4):431–446, 2007.

[44] R. J. Angel, J. Gonzalez-Platas and M. Alvaro. EosFit7c and a Fortran module (library) for equation of state calculations. *Zeitschrift fr Kristallographie - Crystalline Materials*, 229(5):405–419, 2014.

[45] J. F. Nye. *Physical Properties of Crystals*. Oxford University Press, 1957.

[46] O. L. Anderson. *Equations of State of Solids for Geophysics and Ceramic Science*. Oxford University Press, 1995.

[47] F. Birch. Finite elastic strain of cubic crystals. *Phys. Rev.*, 71:809–824, Jun 1947.

[48] R. J. Angel. Equations of State. *Reviews in Mineralogy and Geochemistry*, 41(1):35–59, 2000.

[49] S. Gupta and S. C. Goyal. Anderson-Gruneisen parameter under high temperature in (Fe,Mn,Co,Mg) 2 SiO 4. *Journal of Physics: Conference Series*, 377(1):012075, 2012.

[50] Y. Fei. *Thermal Expansion*. American Geophysical Union, 1995.

[51] K. Takemura. Evaluation of the hydrostaticity of a helium-pressure medium with powder x-ray diffraction techniques. *Journal of Applied Physics*, 89(1), 2001.

[52] M. Chai and J. Michael-Brown. Effects of static non-hydrostatic stress on the R lines of ruby single crystals. *Geophysical Research Letters*, 23(24):3539–3542, 1996.

[53] A. Dewaele and P. Loubeyre. Pressurizing conditions in helium-pressure-transmitting medium. *High Pressure Research*, 27(4):419–429, 2007.

[54] H. K. Mao, R. J. Hemley, Y. Wu, A. P. Jephcoat, L. W. Finger, C. S. Zha, and W. A. Bassett. High-Pressure Phase Diagram and Equation of State of Solid Helium from Single-Crystal X-Ray Diffraction to 23.3 GPa. *Physical Review Letters*, 60:2649–2652, 1988.

[55] S. Klotz, J. C. Chervin, P. Munsch, and G. Le Marchand. Hydrostatic limits of 11 pressure transmitting media. *Journal of Physics D: Applied Physics*, 42(7):075413, 2009.

[56] Y. Fei and Y. Wang. High-Pressure and High-Temperature Powder Diffraction. *Reviews in Mineralogy and Geochemistry*, 41(1):521–557, 2000.

[57] N. Dubrovinskaia and L. Dubrovinsky. *Chapter 25 - Internal and external electrical heating in diamond anvil cells*. Elsevier, Amsterdam, 2005.

[58] C. S. Zha and W. A. Bassett. Internal resistive heating in diamond anvil cell for *in situ* x-ray diffraction and Raman scattering. *Review of Scientific Instruments*, 74(3):1255–1262, 2003.

[59] L. S. Dubrovinsky and P. Saxena, S. K.and Lazor. High-pressure and high-temperature in situ X-ray diffraction study of iron and corundum to 68 GPa using an internally heated diamond anvil cell. *Physics and Chemistry of Minerals*, 25(6):434–441, 1998.

[60] S. T. Weir, D. D. Jackson, S. Falabella, G. Samudrala, and Y. K. Vohra. An electrical microheater technique for high-pressure and high-temperature diamond anvil cell experiments. *Review of Scientific Instruments*, 80(1), 2009.

[61] S. Tateno, K. Hirose, Y. Ohishi, and Y. Tatsumi. The Structure of Iron in Earths Inner Core. *Science*, 330(6002):359–361, 2010.

[62] D. Errandonea. Phase behavior of metals at very high PT conditions: A review of recent experimental studies. *Journal of Physics and Chemistry of Solids*, 67(910):2017–2026, 2006. Study of matter under extreme conditions.

[63] G. Shen, M. L. Rivers, Y. Wang, and S. R. Sutton. Laser heated diamond cell system at the Advanced Photon Source for in situ x-ray measurements at high Pressure and temperature. *Review of Scientific Instruments*, 72(2):1273–1282, 2001.

[64] R. Boehler. Advances in high temperature research in diamond cells. *Recent Trends in High Pressure Research*, pages 591–600, 1992.

[65] A. Salamat and R. A. Fischer and R. Briggs and M. I. McMahon and S. Petitgirard. In situ synchrotron X-ray diffraction in the laser-heated diamond anvil cell: Melting phenomena and synthesis of new materials. *Coordination Chemistry Reviews*, 277278:15 – 30, 2014.

[66] A. F. Goncharov, P. Beck, V. V. Struzhkin, R. J. Hemley, and J. C. Crowhurst. Laser-heating diamond anvil cell studies of simple molecular systems at high pressures and temperatures. *Journal of Physics and Chemistry of Solids*, 69(9):2217 – 2222, 2008.

[67] Y. Meng, R. Hrubiak, E. Rod, R. Boehler, and G. Shen. New developments in laser-heated diamond anvil cell with in situ synchrotron x-ray diffraction at High Pressure Collaborative Access Team. *Review of Scientific Instruments*, 86(7), 2015.

[68] IS Rayfast Limited. `http://tinyurl.com/h4wq8pb`, 2004. Visited on 17/06/2016.

[69] B. Clegg, R. Cooper, R. C. B. Copley, J. A. K. Howard, L. Palatinus, S. Parsons, D. Sivia, K. Fucke, L. Hatcher, S. Moggach, M. Probert, M. Senn, H. Shepherd, H. Sparkes, A. L. Thompson, M. Warren, C. Wilson, and P. Wood. *X-ray Structure Analysis*. 15th edition, 2015.

[70] V. Pecharsky and P. Zavalij. *Fundamentals of Powder Diffraction and Structural Characterization of Materials, Second Edition*. Springer US.

[71] Unknown. X-ray Diffraction. *http://tinyurl.com/zlxlycz*, Visited on 15/09/2015.

[72] W. L. Bragg. The Specular Reflection of X-rays. *Nature*, 90:410, 1912.

[73] J. R. Hook and H. E. Hall. *Solid State Physics*. Wiley.

[74] N. W. Ashcroft and N. D. Mermin. *Solid State Physics*. Saunders College, 1st edition, 1976.

[75] IUCr Online Dictionary of Crystallography. Atomic scattering factor. Visited on 19/05/2017.

[76] E. E. McBride, K. A. Munro, G. W. Stinton, R. J. Husband, R. Briggs, H.-P. Liermann, and M. I. McMahon. One-dimensional chain melting in incommensurate potassium. *Physical Review B*, 91:144111, 2015.

[77] I. Loa, E. I. Isaev, M. I. McMahon, D. Y. Kim, B. Johansson, A. Bosak, and M. Krisch. Lattice Dynamics and Superconductivity in Cerium at High Pressure. *Physical Review Letter*, 108:045502, 2012.

[78] J. Als-Nielsen and D. McMorrow. *Elements of Modern X-ray Physics*. Wiley, New York, NY.

[79] Booster synchrotron. `http://www.diamond.ac.uk/Science/Machine/Components/booster.html`. Visited on 11/11/2015.

[80] Booster. `http://www.esrf.eu/Accelerators/Accelerators/Booster`. Visited on 11/11/2015.

[81] M. Barthelmess, U. Englisch, J. Pflger, A. Schps, J. Skupin, and M. Tischer. Status of the Petra III Insertion Devices. `https://accelconf.web.cern.ch/accelconf/e08/papers/wepc133.pdf`, 2008. Visited on 11/11/2015.

[82] G. Benedetti, Z. Marti, D. Einfeld, and M. Munoz. Beam Optics Measurements during the Commissioning of the ALBA Booster. `https://accelconf.web.cern.ch/accelconf/IPAC10/papers/wepea056.pdf`, 2010. Visited on 11/11/2015.

[83] A. Le Bail, H. Duroy, and J. L. Fourquet. Ab-initio structure determination of $LiSbWO_6$ by X-ray powder diffraction. *Materials Research Bulletin*, 23(3):447 – 452, 1988.

[84] H. M. Rietveld. A profile refinement method for nuclear and magnetic structures. *Journal of Applied Crystallography*, 2(2):65–71, 1969.

[85] R. A. Young and D. B. Wiles. Profile shape functions in Rietveld refinements. *Journal of Applied Crystallography*, 15(4):430–438, 1982.

[86] G. Caglioti, A. Paoletti, and F.P. Ricci. Choice of collimators for a crystal spectrometer for neutron diffraction. *Nuclear Instruments*, 3(4):223 – 228, 1958.

[87] J. P. Attfield, A. K. Cheetham, D. E. Cox, and A. W. Sleight. Synchrotron X-ray and neutron powder diffraction studies of the structure of α-$CrPO_4$. *Journal of Applied Crystallography*, 21(5):452–457, 1988.

[88] G. Will, W. Parrish, and T. C. Huang. Crystal-structure refinement by profile fitting and least-squares analysis of powder diffractometer data. *Journal of Applied Crystallography*, 16(6):611–622, 1983.

[89] W. A. Dollase. Correction of Intensities for preferred orientation in powder diffractometry: Application of the March model. *Journal of Applied Crystallography*, 19(4):267–272, 1986.

[90] B. H. Toby. R factors in Rietveld analysis: How good is good enough? *Powder Diffraction*, 21:67–70, 2006.

[91] R. A. Young. *The Rietveld method*. Oxford University Press, Oxford, 1993.

[92] B. Johansson and A Rosengren. Generalized phase diagram for the rare-earth elements: Calculations and correlations of bulk properties. *Physical Review B*, 11:2836–2857, 1975.

[93] B. E. Douglas. The Lanthanide contraction. *Journal of Chemical Education*, 31(11):598, 1954.

[94] K. Takemura and K. Syassen. Pressure-volume relations and polymorphism of europium and ytterbium to 30 GPa. *Journal of Physics F: Metal Physics*, 15(3):543, 1985.

[95] J. C. Duthie and D. G. Pettifor. Correlation between d-Band Occupancy and Crystal Structure in the Rare Earths. *Physical Review Letters*, 38:564–567, 1977.

[96] G. K. Samudrala and Y. K. Vohra. Crystallographic phases in heavy rare earth metals under megabar pressures. *Journal of Physics: Conference Series*, 377(1):012111, 2012.

[97] Y. K. Vohra, V. Vijayakumar, B. K. Godwal, and S. K. Sikka. Structure of the distorted fcc high-pressure phase of the trivalent rare-earth metals. *Physical Review B*, 30:6205–6207, 1984.

[98] W. Y. Dong, T. H. Lin, K. J. Dunn, and C. N. J. Wagner. Phase transitions in samarium at high pressures. *Physical Review B*, 35:966–970, 1987.

[99] S. D. Barrett and S. S. Dhesiy. *The Structure of Rare-Earth Metal Surfaces*. Imperial College Press, 2011.

[100] J. Akella, J. Xu, and G. S. Smith. Static high pressure studies on Nd and Sc. *Physica B+C*, 139:285 – 288, 1986.

[101] H. Hua, Y. K. Vohra, J. Akella, S. T. Weir, R. Ahujat, and B. Johansson. Theoretical and Experimental Studies on Gadolinium at Ultra High Pressure. *The Review of High Pressure Science and Technology*, 7:233–235, 1998.

[102] F. Porsch and W. B. Holzapfel. Novel Reentrant High Pressure Phase Transtion in Lanthanum. *Physical Review Letters*, 70:4087–4089, 1993.

[103] L. Gerward, J. Staun Olsen, and U. Benedict. On the use of distorted fcc structures for describing high-pressure phases. *Physica B+C*, 144(1):72–78, 1986.

[104] F. Porsch and W. B. Holzapfel. Symmetry change at the fcc–distorted-fcc phase transition of lanthanides under pressure. *Physical Review B*, 50:16212–16218, 1994.

[105] W. A. Grosshans, Y. K. Vohra, and W. B. Holzapfel. Evidence for a Soft Phonon Mode and a New Structure in Rare-Earth Metals under Pressure. *Physical Review Letter*, 49:1572–1575, 1982.

[106] S. R. Evans, I. Loa, L. F. Lundegaard, and M. I. McMahon. Phase transitions in praseodymium up to 23 GPa: An x-ray powder diffraction study. *Physical Review B*, 80:134105, 2009.

[107] H. K. Mao, R. M. Hazen, P. M. Bell, and J. Wittig. Evidence for $4f$–shell delocalization in praseodymium under pressure. *Journal of Applied Physics*, 52(7):4572–4574, 1981.

[108] W. A. Grosshans, Y. K. Vohra, and W. B. Holzapfel. F bonding in praseodymium under high pressure. *Journal of Physics F: Metal Physics*, 13(8):L147, 1983.

[109] V. P. Dmitriev, A. Yu. Kuznetsov, O. Bandilet, P. Bouvier, L. Dubrovinsky, D. Machon, and H.-P. Weber. Stability of the high-pressure monoclinic phases in Ce and Pr metals: Comparative diffraction study and phenomenological theory. *Physical Review B*, 70:014104, 2004.

[110] R. G. Haire, S. Heathman, and U. Benedict. A structural study of promethium metal under pressure. *High Pressure Research*, 2(5-6):273–288, 1990.

[111] N. C. Cunningham, W. Qiu, and Y. K. Vohra. Observation of complete regular trivalent rare earth sequence in heavy lanthanide metal holmium under high pressure. *High Pressure Research*, 26(1):43–50, 2006.

[112] G. K. Samudrala, S. A. Thomas, J. M. Montgomery, and Y. K. Vohra. High pressure phase transitions in the rare earth metal erbium to 151 GPa. *Journal of Physics: Condensed Matter*, 23(31):315701, 2011.

[113] M. Pravica, Z. Quine, and E. Romano. X-ray diffraction study of elemental thulium at pressures up to 86 GPa. *Physical Review B*, 74:104107, 2006.

[114] G. N. Chesnut and Y. K. Vohra. Phase transformation in lutetium metal at 88 GPa. *Physical Review B*, 57:10221–10223, 1998.

[115] Y. R. Shen, R. S. Kumar, A. L. Cornelius, and M. F. Nicol. High-pressure structural studies of dysprosium using angle-dispersive x-ray diffraction. *Physical Review B*, 75:064109, 2007.

[116] G. N. Chesnut and Y. K. Vohra. α-uranium phase in compressed neodymium metal. *Physical Review B*, 61:R3768–R3771, 2000.

[117] Y. C. Zhao, F. Porsch, and W. B. Holzapfel. Intermediate $4f$ bonding structure for samarium under pressure. *Physical Review B*, 50:6603–6608, 1994.

[118] J. S. Olsen, L. Gerward, U. Benedict, and J.-P. Itie. The crystal structure and the equation of state of cerium metal in the pressure range 0–46 GPa. *Physica B+C*, 133(2–3):129 – 137, 1985.

[119] N. Velisavljevic, Y. K. Vohra, and S. T. Weir. Simultaneous electrical and X-ray diffraction studies on neodymium metal to 152 GPa. *High Pressure Research*, 25(2):137–144, 2005.

[120] R. Patterson, C. K. Saw, and J. Akella. Static high-pressure structural studies on Dy to 119 GPa. *Journal of Applied Physics*, 95(10):5443–5446, 2004.

[121] Y. K. Vohra, B. R. Sangala, A. K. Stemshorn, and K. M. Hope. High Pressure Phase Transformations in Heavy Rare Earth Metals and Connections to Actinide Crystal Structures. *Materials Research Society Symposium Proceedings*, 1104, 2011.

[122] G. M. Tsoi J. M. Montgomery, G. K. Samudrala and Y. K. Vohra. High-pressure phase transitions in rare earth metal thulium to 195 GPa. *Journal of Physics: Condensed Matter*, 23(15):155701, 2011.

[123] H. Hong and Y. K. Vohra. Phase Transformations in Heavy Rare Earth Metal Lutetium to 270 GPa. *The Review of High Pressure Science and Technology*, 7:227–229, 1998.

[124] J. Akella, S. T. Weir, Y. K. Vohra, H. Prokop, S. A. Catledge, and G. N. Chesnut. High pressure phase transformations in neodymium studied in a diamond anvil cell using diamond-coated rhenium gaskets. *Journal of Physics: Condensed Matter*, 11(34):6515, 1999.

[125] Y. K. Vohra, B. R. Sangala, A. K. Stemshorn, and K. M. Hope. High Pressure Phase Transformations in Heavy Rare Earth Metals and Connections to Actinide Crystal Structures. In *Symposium NN – Actinides 2008 – Basic Science, Applications and Technology*, volume 1104 of *MRS Online Proceedings Library Archive*, 2008.

[126] G. S. Smith and J. Akella. Reexamination of the crystal structure of a high-pressure phase in praseodymium metal. *Journal of Applied Physics*, 53(12), 1982.

[127] N. Velisavljevic and Y. K. Vohra. Distortion of alpha-uranium structure in praseodymium metal to 311 GPA. *High Pressure Research*, 24(2):295–302, 2004.

[128] B. Johansson. The α-γ transition in cerium is a Mott transition. *Philosophical Magazine*, 30(3):469–482, 1974.

[129] K. Held, C. Huscroft, R. T. Scalettar, and A. K. McMahan. Similarities between the Hubbard and Periodic Anderson Models at Finite Temperatures. *Physical Review Letters*, 85:373–376, 2000.

[130] I.-K. Jeong, T. W. Darling, M. J. Graf, Th. Proffen, R. H. Heffner, Yongjae Lee, T. Vogt, and J. D. Jorgensen. Role of the Lattice in the $\gamma \rightarrow \alpha$ Phase Transition of Ce: A High-Pressure Neutron and X-Ray Diffraction Study. *Physical Review Letters*, 92:105702, 2004.

[131] J. Lim, G. Fabbris, D. Haskel, and J. S. Schilling. Origin of the volume collapse under pressure in elemental Dy. *Journal of Physics: Conference Series*, 500(19):192009, 2014.

[132] O. Eriksson, J. Trygg, O. Hjortstam, B. Johansson, and J. M. Wills. Theoretical aspects of the $4f$-localization at the surface of α-Ce. *Surface Science*, 382(13):93 – 99, 1997.

[133] M. B. Maple, J. Wittig, and K. S. Kim. Pressure-Induced Magnetic-Nonmagnetic Transition of Ce Impurities in La. *Physical Review Letters*, 23:1375–1377, 1969.

[134] M. R. MacPherson, G. E. Everett, D. Wohlleben, and M. B. Maple. Magnetic susceptibility of cerium metal under pressure. *Physical Review Letters*, 26:20–23, 1971.

[135] B. R. Maddox, A. Lazicki, C. S. Yoo, V. Iota, M. Chen, A. K. McMahan, M. Y. Hu, P. Chow, R. T. Scalettar, and W. E. Pickett. $4f$ Delocalization in Gd: Inelastic X-Ray Scattering at Ultrahigh Pressure. *Physical Review Letters*, 96:215701, 2006.

[136] G. Fabbris, T. Matsuoka, J. Lim, J. R. L. Mardegan, K. Shimizu, D. Haskel, and J. S. Schilling. Different routes to pressure-induced volume collapse transitions in Gd and Tb metals. *Physical Review B*, 88:245103, 2013.

[137] G. K. Samudrala, G. M. Tsoi, and Y. K. Vohra. Structural phase transitions in yttrium under ultrahigh pressures. *Journal of Physics: Condensed Matter*, 24(36):362201, 2012.

[138] Y. Akahama, H. Fujihisa, and H. Kawamura. New Helical Chain Structure for Scandium at 240 GPa. *Physical Review Letters*, 94:195503, 2005.

[139] A. Jayaraman. Solid-Liquid and Solid-Solid Transformations in the Rare-Earth Metals at High Pressures. *Physical Review*, 139:A690–A696, 1965.

[140] E. Y. Tonkov and E. G. Ponyatovsky. *Phase Transformations of Elements Under High Pressure*. CRC Press, 2004.

[141] A. Jayaraman. Fusion Curve of Cerium to 70 Kilobar and Phenomena Associated with Supercritical Behavior of fcc Cerium. *Physical Review*, 137:A179–A182, 1965.

[142] M. Seipel, F. Porsch, and W. B. Holzapfel. Characterization of the fcc-distorted fcc-structural transition in lanthanum in an extended pressure and temperature range. *High Pressure Research*, 15(5):321–330, 1997.

[143] A. Schiwek, F. Porsch, and W. B. Holzapfel. High Temperature-High Pressure Structural Studies of Cerium. *High Pressure Research*, 22(2):407–410, 2002.

[144] D. Errandonea, R. Boehler, and M. Ross. Melting of the Rare Earth Metals and f-Electron Delocalization. *Physical Review Letters*, 85:3444–3447, 2000.

[145] Y. C. Zhao, F. Porsch, and W. B. Holzapfel. Determination of triple points in the phase diagram of praseodymium. *Physical Review B*, 52:134–137, 1995.

[146] A. Platau and S.-E. Karlsson. Position of the $4f$ level in γ-cerium. *Journal de Physique Colloques*, 40(C5):C5–385–C5–387, 1979.

[147] A. W. Lawson and T.-Y. Tang. Concerning the High Pressure Allotropic Modification of Cerium. *Physical Review*, 76:301–302, 1949.

[148] D. C. Koskimaki, K. A. Gschneidner, and N. T. Panousis. Preparation of single phase β and α cerium samples for low temperature measurements. *Journal of Crystal Growth*, 22(3):225 – 229, 1974.

[149] J. Wittig. Superconductivity of Cerium Under Pressure. *Physical Review Letters*, 21:1250–1252, 1968.

[150] J. Lægsgaard and A. Svane. Theory of the α-γ phase transition in Ce. *Physical Review B*, 59:3450–3459, 1999.

[151] R. Ramirez and L. M. Falicov. Theory of the $\alpha - \gamma$ Phase Transition in Metallic Cerium. *Physical Review B*, 3:2425–2430, 1971.

[152] J.-P. Rueff, J.-P. Itié, M. Taguchi, C. F. Hague, J.-M. Mariot, R. Delaunay, J.-P. Kappler, and N. Jaouen. Probing the γ-α Transition in Bulk Ce under Pressure: A Direct Investigation by Resonant Inelastic X-Ray Scattering. *Physical Review Letters*, 96:237403, 2006.

[153] R. I. Beecroft and C. A. Swenson. On the existence of a critical point for the phase transition in cerium. *Journal of Physics and Chemistry of Solids*, 15(3):234–239, 1960.

[154] F. H. Ellinger and W. H. Zachariasen. Structure of Cerium Metal at High Pressure. *Physical Review Letters*, 32:773–774, 1974.

[155] G. Bocquillon, R. Epain, and C. Loriers. Volumetric study of the $\alpha \rightarrow \alpha$' phase transformation of cerium and its implications regarding the crystal structure of α' cerium. *Journal of Applied Physics*, 49(8):4431–4432, 1978.

[156] S. Endo, H. Sasaki, and T. Mitsui. A New Allotropic Phase of Cerium above 121 kbar. *Journal of the Physical Society of Japan*, 42(3):882–885, 1977.

[157] D. B. McWhan. Structure of Cerium above 50 kbar. *Physical Review B*, 1:2826–2826, 1970.

[158] Ph. Schaufelberger. Crystal structure of cerium above 50 kbar. *Journal of Applied Physics*, 47(6), 1976.

[159] W. H. Zachariasen. Crystal structures of the α"-cerium phases. *Proceedings of the National Academy of Sciences of the United States of America*, 75(3):1066–1067, 1978.

[160] G. Gu, Y. K. Vohra, and K. E. Brister. Crystal grain growth during phase transformation in cerium metal at high pressure. *Physical Review B*, 52:9107–9110, 1995.

[161] Y. Zhao and W. B. Holzapfel. Structural studies on the phase diagram of cerium. *Journal of Alloys and Compounds*, 246(12):216 – 219, 1997.

[162] W. H. Zachariasen. On the crystal structure of α'-cerium. *Journal of Applied Physics*, 48(4), 1977.

[163] W. H. Zachariasen and F. H. Ellinger. The crystal structures of cerium metal at high pressure. *Acta Crystallographica Section A*, 33(1):155–160, 1977.

[164] M. I. McMahon and R. J. Nelmes. Different Results for the Equilibrium Phases of Cerium above 5 GPa. *Physical Review Letters*, 78:3884–3887, 1997.

[165] Y. K. Vohra, S. L. Beaver, J. Akella, C. A. Ruddle, and S. T. Weir. Ultrapressure equation of state of cerium metal to 208 GPa. *Journal of Applied Physics*, 85(4):2451–2453, 1999.

[166] E. King, J. A. Lee, I. R. Harris, and T. F. Smith. New Phase Boundary for Cerium. *Physical Review B*, 1:1380–1381, 1970.

[167] S. Endo and N. Fujioka. The phase boundary between α'- and tetragonal Ce. *Physics Letters A*, 70(5-6):475 – 476, 1979.

[168] I. T. Belash T. Ye. Antonova and Ye. G. Ponyatovskiy. Phase Diagram of Cerium under pressures up to 85 kbar. *The Physics of Metals and Metallography*, 51(1):110–115, 1981.

[169] O. B. Tsiok and L. G. Khvostantsev. Phase Transitions in Cerium at High Pressures (up to 15 GPa) and High Temperatures. *Journal of Experimental and Theoretical Physics*, 93(6):1245–1249, 2001.

[170] M. I. McMahon, I. Loa and S. G. MacLeod. Private Communication.

[171] A. P. Hammersley, S. O. Svensson, M. Hanfland, A. N. Fitch, and D. Hausermann. Two-dimensional detector software: From real detector to idealised image or two-theta scan. *High Pressure Research*, 14(4-6):235–248, 1996.

[172] V. Petrícek, M. Dusek, and L. Palatinus. *The Crystallographic Computing System JANA2006*. Institute of Physics, Prague, 2006.

[173] A. K. Singh and T. Kenichi. Measurement and analysis of nonhydrostatic lattice strain component in niobium to 145 GPa under various fluid pressure-transmitting media. *Journal of Applied Physics*, 90(7), 2001.

[174] L. Xiong and J. Liu and L. Bai and X. Li and C. Lin and J.-F. Lin. Strength and structural phase transitions of gadolinium at high pressure from radial x-ray diffraction. *Journal of Applied Physics*, 116(24):243503, 2014.

[175] I. Loa. Private Communication.

[176] Pressure-induced transition in titanium metal: a systematic study of the effects of uniaxial stress. *Physica B: Condensed Matter*, 355(14):116 – 125, 2005.

[177] J. F. Herbst. Lattice-constant dependence of the 4 f excitation energy in lanthanum metal. *Phys. Rev. B*, 46:6665–6670, 1992.

[178] D. B. McWhan and W. L. Bond. Simple High Pressure XRay Powder Camera. *Review of Scientific Instruments*, 35(5), 1964.

[179] Y. C. Zhao, F. Porsch, and W. B. Holzapfel. Irregularities of ytterbium under high pressure. *Physical Review B*, 49:815–817, 1994.

[180] G. N. Chesnut and Y. K. Vohra. Structural and Electronic Transitions in Ytterbium Metal to 202 GPa. *Physical Review Letters*, 82:1712–1715, 1999.

[181] D. McWhan, P. W. Montgomery, H. D. Stromberg, and G. Jura. Pressure Temperature Resistance Properties of Lanthanum, Bismuth, Neptuium, Plutonium, and Americian to 450 degC and 30 kB. *The Journal of Physical Chemistry*, 67(11):2308–2311, 1963.

[182] H. Balster and J. Wittig. Pressure-Induced Lattice Instability in fcc Lanthanum at Low Temperature. *Journal of Low Temperature Physics*, 21(3):377–414, 1975.

[183] B. Merkau and W.B. Holzapfel. Kinetics of the dhcp-fcc phase transformation in La under pressure. *Physica B+C*, 139:251–252, 1986.

[184] W. A. Grosshans. *PhD Thesis*. PhD thesis, University of Paderborn, 1987.

[185] W. A. Grosshans and W. B. Holzapfel. *HASYLAB, Jahresbericht, DESY, Hamburg*, 213, 1985.

[186] A. Machida, T. Watanuki, D. Kawana, and K. Aoki. Phase separation of lanthanum hydride under high pressure. *Physical Review B*, 83:054103, 2011.

[187] J. P. McClure. *PhD Thesis*. PhD thesis, University of Nevada, 2009.

[188] C. L. Guillaume and E. Gregoryanz and O. Degtyareva and M. I. McMahon and M. Hanfland and S. Evans and M. Guthrie and S. V. Sinogeikin and H-K. Mao. Cold melting and solid structures of dense lithium. *Nature*, 7:211–214, 2011.

[189] W. A. Grosshans and W. B. Holzapfel. Atomic volumes of rare-earth metals under pressures to 40 GPa and above. *Physical Review B*, 45:5171–5178, 1992.

[190] J. Gonzalez-Platas, M. Alvaro, F. Nestola, and R. Angel. EosFit7-GUI: a new graphical user interface for equation of state calculations, analyses and teaching. *Journal of Applied Crystallography*, 49(4):1377–1382, 2016.

[191] F. H. Spedding, A. H. Daane, and K. W. Herrmann. The crystal structures and lattice parameters of high-purity scandium, yttrium and the rare earth metals. *Acta Crystallographica*, 9(7):559–563, 1956.

[192] A. Jayaraman and R. C. Sherwood. Pressure-Induced Phase Transformation in Gadolinium and Its Effect on the Magnetic Behavior. *Physical Review Letters*, 12:22–23, 1964.

[193] D. B. McWhan and A. L. Stevens. Effect of Pressure on the Magnetic Properties and Crystal Structure of Gd, Tb, Dy, and Ho. *Physical Review*, 139:A682–A689, 1965.

[194] U. Benedict, W.A. Grosshans, and W.B. Holzapfel. Systematics of f electron delocalization in lanthanide and actinide elements under pressure. *Physica B+C*, 144(1):14 – 18, 1986.

[195] N. Hamaya, K. Fuchizaki, and T. Kikegawa. Search for polytipic structures of gadolinium. *High Pressure Research*, 4(1-6):375–377, 1990.

[196] J. Akella, G. S. Smith, and A. P. Jephcoat. High-pressure phase transformation studies in gadolinium to 106 GPa. *Journal of Physics and Chemistry of Solids*, 49(5):573 – 576, 1988.

[197] S. Beaver, G. N. Chesnut and Y. K. Vohra. Image Plate X-Ray Diffraction Study of Distorted FCC Phase in Rare Earth Metals at High Pressures. In *Symposium DD High Pressure Materials Research*, volume 499 of *MRS Proceedings*, page 435 (5 pages), 1997.

[198] F. X. Zhang, M. Lang, J. W. Wang, U. Becker, and R. C. Ewing. Structural phase transitions of cubic Gd_2O_3 at high pressures. *Physical Review B*, 78:064114, 2008.

[199] S. A. Semiletov, R. M. Imamov, and N. A. Ragimli. Production and investigation of thin Gd oxide films. *Kristallografiya*, 19:625–628, 1974.

[200] R. W. G. Wyckoff. *Second edition. Interscience Publishers, New York, New York Fluorite structure*, volume 1. Interscience Publishers, 1963.

[201] A. Boultif and D. Louër. Powder pattern indexing with the dichotomy method. *Journal of Applied Crystallography*, 37(5):724–731, 2004.

[202] R. J. Husband, I. Loa, G. W. Stinton, S. R. Evans, G. J. Ackland, and M. I. McMahon. Europium-IV: An Incommensurately Modulated Crystal Structure in the Lanthanides. *Physical Review Letters*, 109:095503, 2012.

[203] G. Shen, L. Wang, R. Ferry, H.-K. Mao, and R. J. Hemley. A portable laser heating microscope for high pressure research. *Journal of Physics: Conference Series*, 215(1):012191, 2010.